A numerical investigation of internal gravity wave phenomena with adaptive mesh techniques

Benjamin Martin

Ph.D. Thesis

Applied Modelling and Computation Group

Department of Earth Science and Engineering

Imperial College London

Abstract

Internal gravity waves in the oceans are a limited scale process capable of providing sufficient energy to activate strong diapycnal mixing near sloping bathymetry. This can account for a significant portion of oceanic vertical mixing. Mixing can be locally intense, transporting colder nutrient-rich bottom water up onto continental margins with implications for coastal marine ecosystems and the carbon cycle.

Modelling internal waves is particularly challenging. The strong vertical accelerations present in the overturning and breaking of internal waves necessitates a non-hydrostatic model, and the small-scale processes that result from the interaction of internal waves with bathymetry mean that traditional structured mesh models require high-resolution to adequately capture flow complexity.

I present two-dimensional results of numerical simulations of internal waves being generated and interacting with idealised bathymetry, using the Imperial College Ocean Model (Fluidity–ICOM), a non-hydrostatic, finite-element, unstructured mesh model incorporating anisotropic mesh adaptivity. The unstructured nature of Fluidity–ICOM allows the mesh to be optimised to represent complex bathymetries, as well as capturing the vertically inhomogeneous structure of internal waves.

Convergence of the model to analytical results has been demonstrated by modelling internal wave propagation in a linearly stratified fluid. Adaptive mesh simulations have been found to adequately capture the dynamics of internal wave breaking at a slope, and the degeneration of interfacial waves into solitary internal waves, with less computational resources than traditional models. However, further work is needed to simulate the internal leewave generation mechanism of flow over topography.

Acknowledgements

I would like to thank my supervisors, Matthew Piggott, Christopher Pain and Peter Allison, for their guidance, motivation and patience. Thanks also to: my fellow members of AMCG, in particular, Lucy Bricheno, Adam Candy, Cian Wilson, Stephan Kramer, David Ham, Tim Greaves, Patrick Farrell, Hannah Hiester, Colin Cotter, Adrian Umpleby, Gerard Gorman, Michelle Ryder, Fangxin Fang, Surinder Singh, Jon Saunders and Gareth Collins; my examiners, Julie Pietrzak and Stephen Neethling; NERC, for sponsoring this work. Most of all, I would like to thank my parents for their continuing love and support.

Declaration of originality

This is my own work, except where otherwise stated.

Copyright declaration

The copyright of this thesis rests with the author and is made available under a Creative Commons Attribution Non–Commercial No Derivatives licence. Researchers are free to copy, distribute or transmit the thesis on the condition that they attribute it, that they do not use it for commercial purposes and that they do not alter, transform or build upon it. For any reuse or redistribution, researchers must make clear to others the licence terms of this work.

Contents

1 Introduction **13**

1.1 Internal waves 14

1.2 Adaptive unstructured mesh modelling 14

1.3 The research topic 15

1.4 Motivation 17

1.4.1 Observational difficulties 17

1.4.2 Validation of the numerical model 17

1.5 Thesis summary 18

2 Background **20**

2.1 History 21

2.2 The importance of internal waves 23

2.2.1 Mixing 23

2.2.2 Upwelling and transport 24

2.2.3 Potential marine hazard 26

2.3 Theory of internal waves in a linearly stratified fluid 27

2.3.1 Governing equations 27

2.3.2 Reflection at a slope 31

2.3.3 Dispersion relation 33

2.3.4 Polarisation relations and boundary conditions 34

2.4 Theory of internal waves in a two–layer fluid 37

2.4.1 Theory 37

2.4.2 The Korteweg–de Vries equation 38

2.4.3 Energy and mixing of stratified fluids 40

3 Literature Review **46**

3.1 Generation of internal waves 47

3.1.1 Surface generation 47

3.1.2 Bottom generation 48

3.1.3 Interior generation 50

3.2 Observational techniques 51

3.3 Mathematical theory 52

3.4 Linear stratification 53

3.5 Two-layer fluid 53

3.6 Energetics of internal waves 55

4 Numerical Model — The Imperial College Ocean Model **57**

4.1 Unstructured meshes and mesh adaptivity 59

4.1.1 Unstructured meshes 59

4.1.2 Mesh adaptivity 61

4.2 The finite element method 62

4.3 Discretisation of the advection-diffusion equation 64

4.3.1 Weak forms of the equations 64

4.3.2 Basis functions 65

4.4 Discretisation of the Navier-Stokes equations 66

4.4.1 Discretisation with the P_1P_1 finite element pair 66

4.4.2 A projection based solution procedure for velocity and pressure . . 68

4.5 Representing balance in large scale geophysical problems 69

4.6 Control volume discretisation of scalar equations 69

4.7 Boundary conditions 71

4.8 The time loop 72

4.9 Mesh adaptivity 74

4.9.1 Error measures 74

4.9.2 Mesh optimisation methods 75

5 Methodology **77**

5.1 Overview 78

5.2 Propagation of internal waves in a linearly stratified fluid 78
5.2.1 Setup 78
5.3 Breaking of internal waves in a linear stratification 81
5.3.1 Coastal scale simulations 81
5.3.2 Laboratory scale simulations 85
5.4 Generation of internal waves in a two–layer 87
5.4.1 Internal lee wave generation in a two–layer fluid 87
5.4.2 Tilting tank 89
5.5 Shoaling and breaking of internal waves in a two–layer fluid 91

6 Internal waves in a linearly stratified fluid 95
6.1 Propagation 98
6.1.1 Propagation of internal waves in a linearly stratified fluid 98
6.2 Breaking 102
6.2.1 Comparison with MITgcm — a coastal scale numerical simulation . 102
6.2.2 Comparison with SUNTANS — a laboratory scale numerical simulation 122
6.3 Conclusions 127

7 Internal waves in a two–layer fluid 128
7.1 Generation 129
7.1.1 Internal lee wave generation in a two–layer fluid 130
7.1.2 Tilting tank 132
7.2 Breaking 138
7.2.1 Dynamics of a shoaling and breaking event 138
7.2.2 Adaptive mesh results with different interpolation errors 142
7.2.3 The effect of diffusivity 144
7.2.4 The effect of the angle of the slope on shoaling and breaking 149
7.2.5 Reflectance of pseudoenergy 156
7.3 Conclusions 158

8 Conclusions 160

List of Figures

2.1 Two–layer fluid, with $\rho_0 < \rho_1$. 21

2.2 A figure taken from Maas showing the generation of internal waves on the pycnocline. The boat is travelling from left to right. 22

2.3 Energy Budget for global ocean circulation. Image taken from Wunsch and Ferrari (2004). The boxes on the top row are energy sources, the shaded boxes are energy reservoirs in the ocean. Internal waves are an important feature. 25

2.4 Reflection from a subcritical slope for the case $f = 0$. The group and phase velocities are smaller on reflection and the wavenumber and amplitude are greater by a factor of $\frac{\sin(\theta+\alpha)}{\sin(\theta-\alpha)}$. The subscript i denotes the incident wave and the subscript r the reflected wave. 32

2.5 An internal wave as the superposition of upward and downward propagation wave beams. 36

2.6 Two descriptions of a two-layer fluid with an interface of thickness ϵ. . . . 39

2.7 Energy fluxes in a stratified fluid. The symbols are defined in equations (2.116), (2.118) and (2.119). Adapted from Winters et al. (1995). 44

3.1 Schematic of processes affecting internal waves in the ocean taken from Thorpe (1975). His figure caption is "As a challenge, the reader is left to decipher the symbols himself." The key features regarding generation of internal waves are the wind stress and barotropic flow over topography as described in section (3.1). 47

3.2 Global distribution of the energy flux from the semidiurnal tide to internal waves, from Nycander (2005). The units are $\mathrm{W\,m^{-2}}$, with the colour bar logarithmic. Black is less than $10^{-6}\mathrm{W\,m^{-2}}$. 49
3.3 Wave beams of the St. Andrew's Cross. This is a synthetic schieleren photograph which visualises density perturbations in the fluid. The image on the left has oscillation to buoyancy frequency ratio 0.366 , and the image on the right has ratio 0.699. Image taken from Mowbray and Rarity (1967). 50

4.1 The principal steps in the nonlinear Picard iteration algorithm. 73
4.2 An element of unit size in metric space is transformed to an anisotropic element in physical space with the transformation $S = Q\sqrt{|\Lambda|}^{-1}$. 75
4.3 Element operations used to locally optimise the mesh in two dimensions. Top-left: node insertion or edge split. Top-right: node deletion or edge collapse. Bottom-left: edge swap. Bottom-right: node movement. 76

5.1 Initial conditions describing a rightwards propagating mode–1 internal wave in a periodic domain, used in the wave propagation test case. 79
5.2 Domain used in the wave breaking simulations with planar slopes. 81
5.3 Domain for the SUNTANS wave breaking comparison test. 85
5.4 Definition sketch of the problem taken from Kranenburg and Pietrzak (1989). 87
5.5 Initial condition used in the numerical simulations for the perturbation density. Note the topographic bump at $x = 0\,\mathrm{m}$. 88
5.6 Initial condition in the tiliting tank test case. 90
5.7 Displacement of the first leftward-travelling soliton against drag coefficient for the tilting tank test case. Based on this we choose a drag coefficient of $C_D = 0.036$ to best match the experimental data. 91
5.8 Domain used in the shoaling breaking wave simulations and the important parameters. 92
5.9 Initial condition for perturbation density and the perturbation density and velocities after 10 seconds of simulated time for the shoaling breaking wave simulation. 93

6.1 L^2 norm of velocity magnitude against time for increasing resolution over 5 wave periods for the simulations listed in table 5.1. The constant analytical solution is also plotted. The frequency of oscillation is 2ω as a result of the sine–squared function in the velocity magnitude (and as a result 10 oscillations are shown). 97
6.2 Relative error against element size showing quadratic convergence for the wave propagation test case. 98
6.3 Decay rate of the L^2 norm of velocity magnitude against viscosity for different mesh spacing. 100
6.4 Numerical viscosity as a function of mesh spacing. 101
6.5 u–velocity (colour), $\mathrm{m\,s^{-1}}$, and perturbation density (contours) at time $t = 3.0\,T$. The results show the portion of the domain $x \in [1600, 4400]$. The domain has been stretched by a factor of 8 in the vertical to aid visualisation. 104
6.6 u–velocity (colour), $\mathrm{m\,s^{-1}}$, and perturbation density (contours) at time $t = 3.5\,T$. The results show the portion of the domain $x \in [1600, 4400]$. The domain has been stretched by a factor of 8 in the vertical to aid visualisation. 105
6.7 Square of the L^2 norm of velocity magnitude against time for increasing resolution for the wave breaking MITgcm comparison test case. 107
6.8 Square of the L^2 norm of velocity magnitude evaluated in the slope region, $x \in [2400, 3600]$, against time for increasing resolution for the wave breaking MITgcm comparison test case. 108
6.9 u–velocity (colour), $\mathrm{m\,s^{-1}}$, and perturbation density (contours) at time $t = 3.0\,T$. The results show the portion of the domain $x \in [1600, 4400]$. 110
6.10 u–velocity (colour), $\mathrm{m\,s^{-1}}$, and perturbation density (contours) at various times. The results show the portion of the domain $x \in [1600, 4400]$. The domain has been stretched by a factor of 8 in the vertical to aid visualisation. The MITgcm results are taken from Legg and Adcroft (2003). 113
6.11 u–velocity (colour), $\mathrm{m\,s^{-1}}$, and perturbation density (contours) at time $t = 3.1\,T$. The results show the portion of the domain $x \in [1600, 4400]$. The domain has been stretched by a factor of 8 in the vertical to aid visualisation. 115

6.12 u–velocity (colour), $\mathrm{m\,s^{-1}}$, and perturbation density (contours) at time $t = 3.6\,T$. The results show the portion of the domain $x \in [1600, 4400]$. The domain has been stretched by a factor of 8 in the vertical to aid visualisation. 116
6.13 Contour plots of perturbation density against depth and time where $z = 20\,\mathrm{m}$. 117
6.14 Contour plots of u–velocity, $\mathrm{m\,s^{-1}}$, against depth and time where $z = 20\,\mathrm{m}$. 119
6.15 MITgcm results. Contour plots of perturbation density and u velocity against depth and time where the $z = 20\,\mathrm{m}$. Taken from Legg and Adcroft (2003). 120
6.16 Perturbation density, $\frac{\rho(\mathbf{x},t)}{\rho_0} - 1$, in the adaptive mesh Fluidity-ICOM simulation of the laboratory scale wave breaking problem. T is the period of the forcing. Compare with the corresponding SUNTANS result shown in figure 6.18. 123
6.17 The adaptive mesh in the Fluidity-ICOM simulation of the laboratory scale wave breaking problem. T is the period of the forcing. 124
6.18 SUNTANS result; perturbation density. Taken from Venayagamoorthy and Fringer (2007). 125
6.19 Fluidity-ICOM simulation of the laboratory scale wave breaking problem with Froude number $\mathrm{Fr} = 0.2$. 125
6.20 Fluidity-ICOM simulation of the laboratory scale wave breaking problem with Froude number $\mathrm{Fr} = 0.4$. 126
6.21 Fluidity-ICOM simulation of the laboratory scale wave breaking problem with Froude number $\mathrm{Fr} = 0.6$. 126
6.22 Fluidity-ICOM simulation of the laboratory scale wave breaking problem with Froude number $\mathrm{Fr} = 0.8$. 126
6.23 Fluidity-ICOM simulation of the laboratory scale wave breaking problem with Froude number $\mathrm{Fr} = 1.0$. 127

7.1 Density after 90 seconds in the lee wave generation problem. 130
7.2 Numerical and analytical results for the lee wave generation problem. . . . 130
7.3 Experimental result taken from Kranenburg and Pietrzak (1989). The crosses are the data from the laboratory experiment. 131
7.4 Evolution of the interface with time at $x = 0.02$ for the tilting tank test. . 132

7.5 Evolution of the interface with time at $x = 0.1$ for the tilting tank test. . . 132
7.6 Evolution of the interface with time at $x = 0.1$ for the adaptive mesh simulation for the tilting tank test case. 133
7.7 Number of nodes in mesh for the adaptive result against time. 134
7.8 Density and adapted mesh at different times for the tilting tank test case. The times at which the images have been taken are chosen to compare to those in figure 7.9. 135
7.9 Density at various times taken from Horn et al. (2001). The caption in Horn et al. (2001) is "Photographs showing the steepening of an initial basin–scale wave to form a packet of solitons. The photographs show the whole 6 m of the tank. The evolving train of solitons is propagating from left to right in panels (b)–(d), from right to left in panel (e) and from left to right in panel (f)." Note the ultrasonic gauge close to the centre of the tank, which we estimate could be up to 0.1 m from the centre of the tank. 136
7.10 Evolution of the interface with time at $x = 0.1$ for the adaptive mesh simulation with smaller interpolation errors for the tilting tank test case. 137
7.11 Density field, showing the shoaling and breaking of a solitary wave. 139
7.12 Velocity vectors and density contours at 31 s of simulated time in the shoaling breaking wave simulation. A relatively large scale anti–clockwise circulation can be seen to have developed, with a smaller scale clockwise secondary circulation close to the boundary. 140
7.13 Evolution of the energy in the shoaling breaking wave simulation. Note the start of the mixing event at approximately 30 s, where the energy lost through mixing starts to increase. The wave is reflected at the left-hand boundary of the domain at approximately 60 s, where there is a local minimum in the kinetic energy. 141
7.14 Perturbation density and meshes for different adaptivity options at various times for the shoaling breaking wave problem. 143
7.15 Perturbation density (including a zoom of the shoaling region) and adaptive mesh for different diffusivities after 28 seconds in the shoaling breaking wave problem. 145

7.16 Perturbation density (including a zoom of the shoaling region) and adaptive mesh for different diffusivities after 35 seconds in the shoaling breaking wave problem. 146
7.17 Perturbation density (including a zoom of the shoaling region) and adaptive mesh for different diffusivities after 42 seconds in the shoaling breaking wave problem. 147
7.18 Plots of energy against time for different diffusivities in the shoaling breaking wave problem. Energy lost through mixing is similar for each case except for that with a diffusivity of $\kappa = 10^{-6}\,\mathrm{m}^2\,\mathrm{s}^{-1}$. 148
7.19 Perturbation density at different times for slope 0.54, simulation 'slope0250'. Diffusivity is set to $\kappa = 10^{-7}\,\mathrm{m}^2\,\mathrm{s}^{-1}$. 150
7.20 Perturbation density at different times for slope 0.3, simulation 'slope0450'. Diffusivity is set to $\kappa = 10^{-7}\,\mathrm{m}^2\,\mathrm{s}^{-1}$. 150
7.21 Perturbation density at different times for slope 0.15, simulation 'slope0900'. Diffusivity is set to $\kappa = 10^{-7}\,\mathrm{m}^2\,\mathrm{s}^{-1}$. 151
7.22 Perturbation density at different times for slope 0.1, simulation 'slope1350'. Diffusivity is set to $\kappa = 10^{-7}\,\mathrm{m}^2\,\mathrm{s}^{-1}$. 153
7.23 Perturbation density at different times for slope 0.045, simulation 'slope3000'. Diffusivity is set to $\kappa = 10^{-7}\,\mathrm{m}^2\,\mathrm{s}^{-1}$. 154
7.24 Plots of energy against time for different slopes. Diffusivity is set to $\kappa = 10^{-7}\,\mathrm{m}^2\,\mathrm{s}^{-1}$. 155
7.25 Reflectance of pseudoenergy as a function of Iribarren number. 157

Chapter 1

Introduction

Contents

1.1 Internal waves **14**

1.2 Adaptive unstructured mesh modelling **14**

1.3 The research topic **15**

1.4 Motivation **17**

1.4.1 Observational difficulties 17

1.4.2 Validation of the numerical model 17

1.5 Thesis summary **18**

1.1 Internal waves

Internal waves are a ubiquitous feature of the world's oceans (Garrett and Munk, 1979). They can exist where there is a stable density stratification, caused either by temperature or salinity variations (or both). Tidally driven flow of stratified fluid over topography is the main mechanism by which internal waves are generated in the ocean (Garrett and Kunze, 2007). These waves can propagate large distances until they interact with continental shelves and slopes, where the waves break, activating intense vertical mixing, which plays an important part of the global energy budget of the oceans and bio–geochemical cycles (Munk and Wunsch, 1998). Being able to understand and predict their behaviour is thus important, with their complexity leading to the need for advanced computational methods for their simulation.

1.2 Adaptive unstructured mesh modelling

When solving the partial differential equations governing geophysical fluid dynamics, one must discretise the continuous world down to a discrete (finite) one that can be considered on a computer. This is achieved through a computational mesh or grid of finite sized cells which approximate the domain under consideration. The traditional approach for discretising a domain is through structured meshes, which possess a uniform topological structure and usually comprise a largely uniform resolution. Their ability to align with coastlines and bathymetry is limited, and cannot align with dynamic solution features (*e.g.* boundary layers). Unstructured meshes (*e.g.* triangular or tetrahedral meshes with arbitrary connectivity and cell size variabilty) have several advantages over structured meshes. They can conform to complex topography which avoids the need to represent topography as a 'staircase' (discontinuous horizontal and vertical jumps in the mesh which can lead to large errors in the numerical solution (Adcroft et al., 1997)), or use shaved cells at the bottom of the water column, as well as avoiding the need to use an alternative vertical coordinate such as sigma or isopycnal coordinates. Unstructured meshes also enable the use of increased resolution in an anisotropic fashion meaning that features such as boundary layers can be accurately resolved with more efficiency than an isotropic mesh would allow; the anisotropy afforded by an unstructured mesh allows long, thin elements,

and so a feature such as a boundary layer can be accurately resolved with fewer elements and thus less computational resource. While numerical models based on unstructured meshes often require significant computational overheads, the overall efficiency of such models can outperform traditional structured mesh models, though it must be stressed that this depends on the problem being solved.

While offering these advantages, one of the disadvantages of unstructured meshes is that they can lead to pressure gradient errors. However, this problem can be overcome by decomposing the dynamical pressure into a balance, or 'hydrostatic-geostrophic', pressure and a residual pressure term. Another potential difficulty with unstructured meshes is the large range of length–scales present the mesh. This can lead to problems in solving the resulting linear systems, which can be overcome by using appropriate solvers based on multigrid methods.

The flexibility afforded by unstructured meshes facilitates the use of adaptive meshes that can be used to focus resolution in regions of dynamical interest, which are often time dependent, and resolve any developing flow features in a more computationally efficient manner than using a high resolution fixed mesh everywhere in the domain.

1.3 The research topic

Previous work on numerical modelling of internal waves has usually relied upon the traditional approach using structured meshes (Legg and Adcroft, 2003; Berntsen et al., 2006; Bourgault and Kelley, 2007; Vlasenko and Stashchuk, 2007; Lamb and Nguyen, 2009; Aghsaee et al., 2010). Unstructured meshes have also been used (Labeur and Pietrzak, 2004). Some work has been done with adaptive mesh refinement (AMR) on structured meshes (Rickard et al., 2009), but the use of an adaptive unstructured mesh to model internal waves has not been investigated before. This is the main thrust of the work presented here.

The purpose of this thesis is to investigate internal wave generation, propagation and breaking using an adaptive unstructured mesh model. Internal wave breaking occurs at a much smaller scale than the processes of internal wave generation and propagation. The use of an adapting variable resolution mesh represents a practical means to faithfully represent the physical processes involved in internal wave breaking at the smaller scale, as

well as capturing the larger scale dynamics of internal wave propagation without the need to couple, or nest, different models. Traditional fixed mesh models require a large amount of computational resources to resolve these small scale physical processes, and so the ability to focus resolution in regions of interest expedites the overall simulation of the dynamics involved across a range of scales. Sub–grid scale modelling is often used to represent small scale processes, but since their effects can feed into the large–scale dynamics and vice versa, it is preferable to resolve all the physical processes without resorting to parameterisations.

A new model is presented, which is quite different from most ocean models of today. Computational efficiency is improved through the use of robust finite element discretizations on fully unstructured meshes in conjunction with parallel anisotropic mesh adaptivity algorithms.

The results presented in this thesis have been separated into two sections: internal waves in a linearly stratified fluid; and internal waves in a two-layer fluid. For each case, numerical simulations have been carried out to validate an aspect of the novel numerical model considered here. For the case of linear stratification, fixed mesh simulations are performed to examine the numerical convergence of the kinetic energy with increasing mesh resolution for a propagating internal wave, and the level of numerical viscosity (the non–physical viscosity inherent in a numerical model) is estimated as a function of mesh spacing.

For the two-layer fluid, fixed mesh numerical simulations of the generation of internal waves by flow over topography are compared with laboratory experiments and an analytical solution (Kranenburg and Pietrzak, 1989; Labeur and Pietrzak, 2004). Also, the adaptive mesh capability is investigated with numerical simulations of the degeneration of interfacial waves into solitary waves, with comparisons made between high resolution fixed mesh results, laboratory experiments (Horn et al., 2001), and simulations with adaptive meshes.

In order to validate the model further, results of the simulations are compared with results from other leading numerical models. The more complex case of breaking of internal waves in a linearly stratified fluid at a slope offers no analytical solution, and few laboratory experiments to compare with, and so the efficacy of the numerical model can be examined by comparing the results with other numerical models (Legg and Adcroft, 2003; Venayagamoorthy and Fringer, 2005). This is conducted with several slope geometries

(planar, concave and convex slopes) and various levels of non–linearity of the waves, as quantified by an appropriate Froude number (a non–dimensional quantity defined by ratio of the velocity magnitude of the incoming wave to the phase speed).

Finally, internal solitary waves in a two-layer fluid breaking at a slope are examined with adaptive mesh simulations. A detailed consideration of the energy budget allows the quantification of the effect of changing parameters in the numerical model (*e.g.* the interpolation errors used to guide the adaptivity algorithm), in addition to physical parameters (*e.g.* the wave amplitude and the length of the slope), on the energy reflected at the slope as well as the energy that is lost through mixing.

1.4 Motivation

1.4.1 Observational difficulties

Internal waves have structure in the horizontal and vertical directions as well as being time dependent, constrained by a dispersion relation. The generation of a time history of the three–dimensional (3D) structure of internal waves in the real ocean therefore requires a complex array of sensors which is rarely available. Therefore it is rather expedient to model internal waves numerically. Some of the observational techniques that have been used to study internal waves are reviewed in section (3.2).

1.4.2 Validation of the numerical model

One of the main objectives of this thesis is to explore the utility of the novel Imperial College Ocean Model (hereafter Fluidity–ICOM) in modelling internal waves. The non-hydrostatic nature of the overturning and breaking of internal waves necessitates a non-hydrostatic model, and the small-scale processes that result from the interaction of internal waves with bathymetry mean that traditional structured mesh models require high-resolution to adequately resolve the evolution of the flow. The unstructured nature of the model considered here allows the mesh to be optimised to represent complex bathymetries, as well as capturing the vertically inhomogeneous structure of internal waves. The adaptive mesh capability of Fluidity–ICOM allows us to model internal waves in a more computationally efficient manner, *i.e.* with fewer degrees of freedom and less overall computational

resources, and this is validated against high-resolution fixed mesh results and other model and laboratory results.

1.5 Thesis summary

In chapter 2 a brief history of internal waves is presented, including descriptions of some of the first observations of internal waves. The importance of internal waves in the ocean is also highlighted. The mathematical theory of internal waves in both linearly stratified and two–layer fluids is outlined here. The background literature of internal waves in the ocean is presented in chapter 3.

In chapter 4 the numerical model, Fluidity–ICOM, is described. The most important features of the model with regard to modelling internal waves, particularly internal wave breaking, are the non-hydrostatic and the adaptive mesh capabilities. Chapter 5 contains an overview of the approach taken in the thesis, and includes details of the simulations that are considered, the numerical setups and the diagnostics that are used to assess them

Chapter 6 considers internal waves in linearly stratified fluids. The propagation of internal waves in a linearly stratified fluid and the breaking of internal waves in a linearly stratified fluid are all examined in order to quantify the applicability of Fluidity–ICOM to the study of internal waves. The kinetic energy of a propagating internal wave is shown to converge to an analytical solution with increasing mesh resolution in a quadratic fashion. Also, the more complex case of internal waves breaking at a slope is shown to compare favourably with other leading numerical models.

Internal waves in a two–layer fluid are then examined in chapter 7. Having considered internal waves in a linearly stratified fluid, which admitted an exact solution to the linearised equations and thus allowed a good means to validate the numerical model, internal waves in a two–layer fluid are considered, which is more representative of the stratification found in the upper ocean. The generation of internal waves in a two–layer fluid through flow over topography, and the degeneration of large–scale interfacial waves into solitary waves are considered. The leading internal solitary wave train that results from the degeneration of a sloped interface has the same number of solitons as a laboratory experiment, and adaptive mesh simulations compare favourably with high resolution fixed mesh simulations with a large increase in computational efficiency. Finally, internal solitary wave

breaking at a slope is investigated through a detailed consideration of the energy budget, and the energy reflected at the slope is quantified. A good fit between the calculated reflectances and the functional dependence of reflectance on the wave amplitude and slope length indicates that the energetic analysis and the numerical simulations are robust.

Chapter 8 summarises the conclusions drawn from this study, along with potential further work modelling internal waves with adaptive unstructured mesh techniques.

Chapter 2

Background

Contents

2.1 History 21

2.2 The importance of internal waves 23

2.2.1 Mixing 23

2.2.2 Upwelling and transport 24

2.2.3 Potential marine hazard 26

2.3 Theory of internal waves in a linearly stratified fluid 27

2.3.1 Governing equations 27

2.3.2 Reflection at a slope 31

2.3.3 Dispersion relation 33

2.3.4 Polarisation relations and boundary conditions 34

2.4 Theory of internal waves in a two–layer fluid 37

2.4.1 Theory 37

2.4.2 The Korteweg–de Vries equation 38

2.4.3 Energy and mixing of stratified fluids 40

2.1 History

Internal gravity waves can propagate in any stably–stratified fluid through the restoring force of gravity on fluid particles displaced from their equilibrium levels. The simplest stable stratification is that of a two–layer fluid, with one layer of fluid above another of greater density, as shown in figure 2.1.

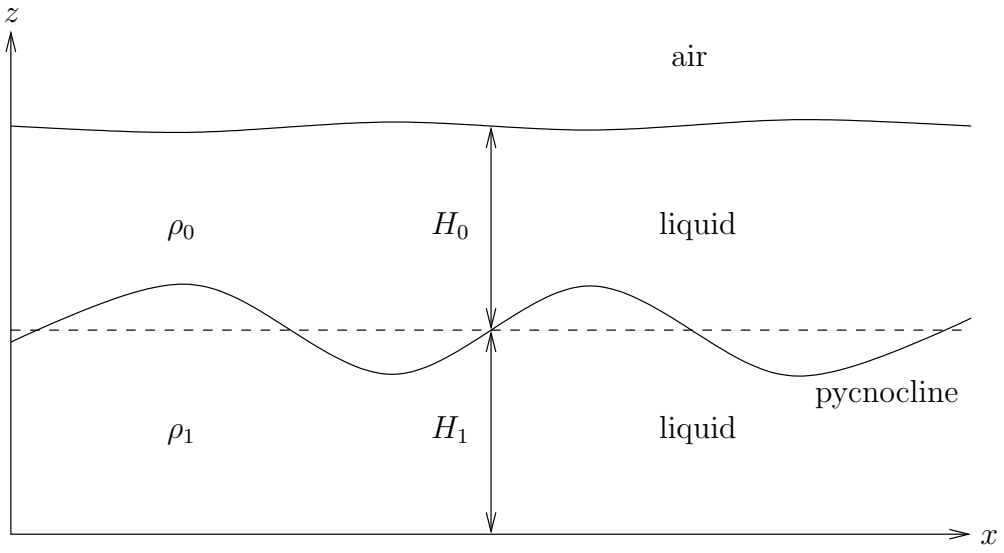


Figure 2.1: Two–layer fluid, with $\rho_0 < \rho_1$.

The interface between these layers, the pycnocline, can undergo oscillations, with little manifestation on the air–liquid surface above, if we assume the two layers in question are in the ocean, for example. Although this case reduces to that of surface waves when $\rho_0 \ll \rho_1$, these internal waves differ primarily in their amplitudes, which are typically 10^3 times greater, and their phase speeds, which are of the order of $1\,\mathrm{m\,s^{-1}}$ compared to $c = \sqrt{gH} \sim 200\,\mathrm{m\,s^{-1}}$ for surface waves in the deep ocean, *i.e.* such waves could cross the Atlantic Ocean in approximately 7 hours (Gill, 1982, p. 107). In the continuously stratified interior of the ocean, the restoring force of gravity is much weaker than for the two–layer fluid, and the periods and wavelengths of internal waves are much greater.

Internal waves had been predicted much earlier than the first observations. Stokes (1847) was the first to develop the theory of internal waves at the boundary surface in a fluid consisting of two layers of infinite thickness; the extension to continuous stratification was performed by Rayleigh (1883).

One of the first documented effects of internal waves in the ocean dates from the

late nineteenth century, when the Norwegian explorer Fridtjof Nansen experienced strong resistance to his vessel, the *Fram*, on his expedition through the Arctic Ocean.

This phenomenon, called "dead water" by mariners, which can occur when a slow–moving vessel creates internal waves at the lower boundary of a thin freshwater surface layer, was later explained by Ekman (1904). If the ship's draft (the distance between the highest waterline and the bottom of the ship) is close to the thickness of the freshwater surface layer, then the ship can generate an internal wave on the pycnocline which radiates energy away from the neighbourhood of the ship, and the ship experiences this as additional drag. This drag reaches a maximum when the ship is travelling close to the speed of propagation, c, of this (baroclinic) wave, given by

$$c^2 = g' \frac{H_0 H_1}{H_0 + H_1}, \tag{2.1}$$

where H_0 and H_1 are the equilibrium depths of the two layers and $g' = g(\rho_1 - \rho_0)/\rho_1$ is the reduced gravity.

Maas has carried out laboratory experiments to illustrate "dead water". A small boat was dragged along a channel containing a two layer fluid by means of a small weight. Figure 2.2 shows the experiment. The generation of an internal wave can be seen behind the small boat.

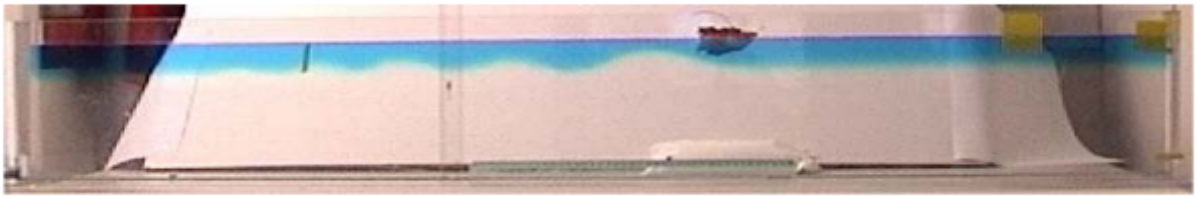


Figure 2.2: A figure taken from Maas showing the generation of internal waves on the pycnocline. The boat is travelling from left to right.

Note that if the lower layer is much deeper than the upper, $H_1 \gg H_0$ the phase speed c can be approximated by

$$c^2 \approx g' H_0, \tag{2.2}$$

so that the internal wave is similar to a surface wave on water of the depth of the shallower upper layer with the acceleration due to gravity g' instead of g.

Ekman also brought attention to an account by Pliny the Elder (Pliny, 77), which may be one of the earliest documentations of internal waves:

> *Est parvus admodum piscis adsuetus petris, echeneis appellatus. hoc carinis adhaerente naves tardius ire creduntur... fertur Actiaco Marte tenuisse praetoriam navem Antoni properantis circumire et exhortari suos, donec transiret in aliam, ideoque Caesariana classis impetu maiore protinus venit.*

> There is a very small rock–dwelling fish called the Remora which is believed to slow down ships by attaching itself to their keels... It is thought that one of these fish held up Mark Antony's flagship at the battle of Actium, just as he was hurrying to rally his men and boost their morale. By the time he had swapped ships, Caesar's fleet had gained the advantage and had a stronger attack.

Ekman suggested that internal waves, rather than the Remora, were responsible for the retardation of Antony's ship. The Battle of Actium took place in the mouth of the modern day Ambracian Gulf. The Ambracian Gulf is a fairly shallow gulf which is fed by the Louros and Arachthos rivers, which make it warmer and fresher that the Ionian Sea. A warm, fresher current flows into the Ionian Sea from the Ambracian Gulf, making the region in which the battle of Actium took place a region of freshwater influence. This means there could have been a layer of brackish (saltier than freshwater, but less salty than seawater) water on the surface in which Antony's heavier, deeper draft quinqueremes may well have experienced the effect of dead water whereas Octavian (Caesar) had lighter shallower–draft vessels. Antony's deeper draft vessels would have been more likely to be captured by dead water, and Pliny's description of Antony's vessel being held fast may have been accurate (Parker, 1999).

2.2 The importance of internal waves

2.2.1 Mixing

The oceans are, on the whole, stably–stratified, which not only means that they can support internal waves, but also that vertical mixing is inhibited. Cold, dense water that is formed

in high–latitude regions (e.g. via open–ocean deep–convection (Marshall and Schott, 1999)) sinks and spreads over the bottom of the oceanic basins. This water must be slowly mixed with the waters above if a quasi steady state is to be achieved.

Rough estimates of the vertical diffusivity of the global ocean required to maintain stratification are of the order of $10^{-4}\,\mathrm{m^2 s^{-1}}$ (Wunsch and Ferrari, 2004). However, local measurements of vertical diffusivity away from topographic features are of the order of $10^{-5}\,\mathrm{m^2 s^{-1}}$ (Munk and Wunsch, 1998). The oceanic internal wave field can provide a sufficient source of energy to activate strong vertical mixing near sloping boundaries, thus increasing the overall vertical diffusivity of the ocean. Global ocean models often use vertical diffusivities that are too large as a parameterisation of vertical mixing and convection. Understanding the vertical mixing that occurs when internal waves break at topography is thus an essential part of any global ocean model.

Sandström's theorem (Sandström, 1908) essentially states that the meridional overturning circulation is mechanically, rather than thermally, driven. Winds and tides are the only source of mechanical energy to drive the interior mixing.

Internal waves are an important feature of the global energy budget, as demonstrated by Wunsch and Ferrari (2004). They estimate that the total energy supplied to the global ocean through astronomical tidal forcing is of the order of 3.5TW, and further estimate that 1TW of this energy is available to mix the abyssal ocean. Figure (2.3) summarises the global energy budget.

Wind driven mixing happens at the surface of the ocean and most of the atmospheric kinetic energy transferred to the ocean remains in the upper mixed layer generating surface waves whose energy is dissipated at coastlines. Tidal forcing over topography happens in the deep ocean and is much better placed than wind forcing to activate abyssal mixing.

2.2.2 Upwelling and transport

When an internal wave reflects from sloping topography, the frequency of the reflected wave is the same as that of the internal wave. This means that internal wave characteristics (the group velocity, or lines of constant phase) maintain their angle to the horizontal on reflection. When the topographic slope is less than this angle the topography is subcritical. Similarly, when the topographic slope is greater than this angle the topography is

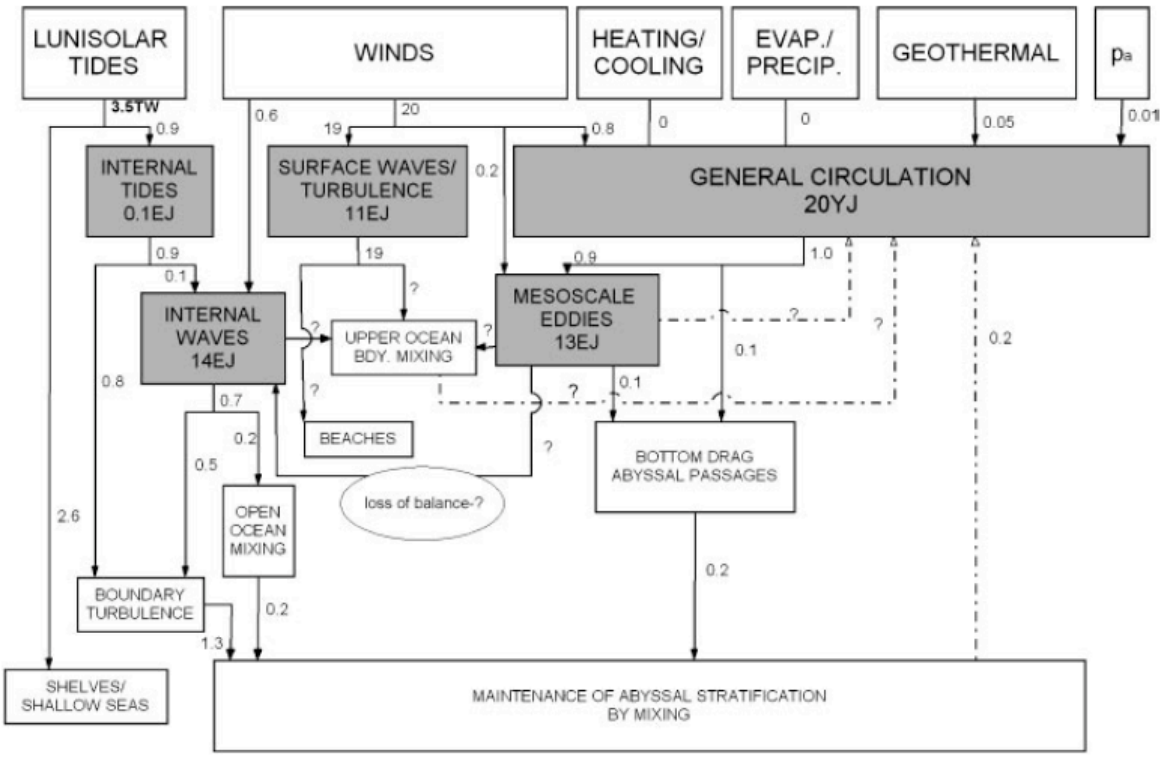


Figure 2.3: Energy Budget for global ocean circulation. Image taken from Wunsch and Ferrari (2004). The boxes on the top row are energy sources, the shaded boxes are energy reservoirs in the ocean. Internal waves are an important feature.

supercritical (see section (2.3.2) for details.)

For slopes close to the critical angle (critical topography), internal wave breaking occurs and generates an internal tidal bore. This bore, or bolus, propagates up the continental margin. This upwelling transports cold water, rich in nutrients and phytoplankton, onto the continental shelf with important biological and climatological implications.

In Monterey Canyon, internal waves could be responsible for as much as 30 % of enrichment during non–upwelling periods (Shea and Broenkow, 1982).

2.2.3 Potential marine hazard

Solitary internal waves (solitons) can inflict damage on off–shore structures associated with oil–drilling operations. The large amplitudes and the associated strong currents can impose great bending moments on those structures. It has been reported that some deep–sea drillings for oil in areas where these internal solitons occur (e.g. in the South China Sea) were damaged by the passage of a soliton (Cai et al., 2006).

It has been speculated that the cause of the loss of the nuclear submarine USS Thresher in 1963 was that it was hit by a solitary internal wave. Submarines can alter their buoyancy by filling their ballast tanks with sea water or pressurised air. They can minimise their sound transmission (and so the risk of being detected) by travelling along the pycnocline which reflects any engine noise downwards. The amplitude of a soliton is greatest in the pycnocline. If the Thresher was travelling along the pycnocline when it encountered a large amplitude soliton, the submarine would not have had time to alter its buoyancy and would have sunk down to depths beyond its designed depth and imploded (Pinet, 2008; Parker, 1999).

2.3 Theory of internal waves in a linearly stratified fluid

2.3.1 Governing equations

We start with the incompressible Navier–Stokes equations

$$\rho \frac{D\mathbf{u}}{Dt} = -\nabla p + \mu \nabla^2 \mathbf{u} + \rho \mathbf{F}, \tag{2.3}$$

$$\nabla \cdot \mathbf{u} = 0, \tag{2.4}$$

where $\mathbf{u} = (u, v, w)^T$ is the three–dimensional velocity, ρ is the density, p is the pressure, μ is the dynamic viscosity, $\mathbf{F}$ is an arbitrary body force and $\frac{D}{Dt} = \frac{\partial}{\partial t} + \mathbf{u} \cdot \nabla$ is the Lagrangian derivative (Batchelor, 1967).

The body force $\mathbf{F}$ includes gravity and the Coriolis force since we are in a rotating frame of reference

$$\mathbf{F} = \mathbf{g} - 2\boldsymbol{\Omega} \wedge \mathbf{u}, \tag{2.5}$$

where $\mathbf{g} = -g\mathbf{k}$, g is the acceleration due to gravity, $\boldsymbol{\Omega} = \frac{1}{2} f \mathbf{k}$ is the Earth's rotation vector in the local frame of reference and $\mathbf{k}$ is a unit vector in the vertically upwards direction.

Our governing equations are thus

$$\rho \frac{D\mathbf{u}}{Dt} + 2\rho\boldsymbol{\Omega} \wedge \mathbf{u} = -\nabla p - \rho g \mathbf{k} + \mu \nabla^2 \mathbf{u}, \tag{2.6}$$

$$\nabla \cdot \mathbf{u} = 0. \tag{2.7}$$

We can decompose the density field as (Cushman-Roisin (1994) p.139)

$$\rho(\mathbf{x}, t) = \rho_0 + \tilde{\rho}(z) + \rho'(\mathbf{x}, t), \tag{2.8}$$

where ρ_0 is the reference density (a constant, e.g. $1025\,\mathrm{kg\,m^{-3}}$), $\tilde{\rho}(z)$ is the ambient equilibrium stratification, and $\rho'(\mathbf{x}, t)$ is a density fluctuation induced by, for example, an internal gravity wave. The inequality $|\tilde{\rho}| \ll \rho_0$ is required to justify the Boussinesq approximation[1](Boussinesq, 1903), while the further inequality $|\rho'| \ll |\tilde{\rho}|$ is required to linearise the problem.

[1]in which case we can combine the first two terms into a "constant" term with non–zero gradient.

Similarly, we write pressure as

$$p(\mathbf{x},t) = p_0(z) + p'(\mathbf{x},t), \tag{2.9}$$

so that (2.6) in the absence of motion becomes $\frac{dp_0}{dz} = -(\rho_0 + \tilde{\rho})g$, which expresses hydrostatic balance.

The Boussinesq approximation follows by neglecting the fluctuation in density, ρ', in all the terms except for $-\rho g\mathbf{k}$ and dividing through by ρ_0 to yield

$$\frac{D\mathbf{u}}{Dt} + 2\boldsymbol{\Omega} \wedge \mathbf{u} = -\frac{1}{\rho_0}\nabla p - \frac{\rho'}{\rho_0}g\mathbf{k} + \nu\nabla^2\mathbf{u}, \tag{2.10}$$

where $\nu = \mu/\rho_0$ is now the kinematic viscosity.

In the absence of thermal and saline diffusivity, density is conserved following a fluid particle

$$\frac{D\rho}{Dt} = 0. \tag{2.11}$$

The governing linearised equations (ignoring viscous effects) are

$$x\text{–momentum} \qquad \frac{\partial u}{\partial t} - fv = -\rho_0^{-1}\frac{\partial p'}{\partial x}, \tag{2.12}$$

$$y\text{–momentum} \qquad \frac{\partial v}{\partial t} + fu = -\rho_0^{-1}\frac{\partial p'}{\partial y}, \tag{2.13}$$

$$z\text{–momentum} \qquad \frac{\partial w}{\partial t} = -\rho_0^{-1}\frac{\partial p'}{\partial z} - \frac{\rho'}{\rho_0}g, \tag{2.14}$$

$$\text{continuity} \qquad \frac{\partial u}{\partial x} + \frac{\partial v}{\partial y} + \frac{\partial w}{\partial z} = 0, \tag{2.15}$$

$$\text{density} \qquad \frac{\partial \rho'}{\partial t} + w\frac{d\tilde{\rho}}{dz} = 0. \tag{2.16}$$

The Brunt–Väisälä frequency $N(z)$ is defined by

$$N^2(z) = -\frac{g}{\rho_0 + \tilde{\rho}(z)}\frac{d\tilde{\rho}}{dz} \approx -\frac{g}{\rho_0}\frac{d\tilde{\rho}}{dz}, \tag{2.17}$$

which for a linear stratification can be assumed to be everywhere a constant and so in this case we can replace (2.16) with

$$\frac{\partial \rho'}{\partial t} - \frac{\rho_0 N^2}{g}w = 0. \tag{2.18}$$

Now we have a linear system of five equations with five unknowns which is easily soluble (see section 2.3.3). If, however, the Brunt–Väisälä frequency $N(z)$ is not constant, we do not have a linear system since our coefficient of w in (2.16) is not constant. In this case, we eliminate all variables except w as follows.

Differentiating (2.12) and (2.13) with respect to(w.r.t.) z yields

$$\frac{\partial^2 u}{\partial z \partial t} - f\frac{\partial v}{\partial z} = -\rho_0^{-1}\frac{\partial^2 p'}{\partial z \partial x}, \tag{2.19}$$

$$\frac{\partial^2 v}{\partial z \partial t} + f\frac{\partial u}{\partial z} = -\rho_0^{-1}\frac{\partial^2 p'}{\partial z \partial y}. \tag{2.20}$$

Now differentiating (2.14) w.r.t. both x and y separately and subtracting from (2.19) and (2.20) eliminates all terms in p':

$$\frac{\partial^2 u}{\partial z \partial t} - f\frac{\partial v}{\partial z} = \frac{\partial}{\partial t}\left(\frac{\partial w}{\partial x}\right) + \frac{g}{\rho_0}\left(\frac{\partial \rho'}{\partial x}\right), \tag{2.21}$$

$$\frac{\partial^2 v}{\partial z \partial t} + f\frac{\partial u}{\partial z} = \frac{\partial}{\partial t}\left(\frac{\partial w}{\partial y}\right) + \frac{g}{\rho_0}\left(\frac{\partial \rho'}{\partial y}\right). \tag{2.22}$$

Differentiating these relations w.r.t. t gives

$$\frac{\partial^3 u}{\partial z \partial t^2} - f\frac{\partial^2 v}{\partial z \partial t} = \frac{\partial^2}{\partial t^2}\left(\frac{\partial w}{\partial x}\right) + \frac{g}{\rho_0}\left(\frac{\partial}{\partial x}\left[\frac{\partial \rho'}{\partial t}\right]\right), \tag{2.23}$$

$$\frac{\partial^3 v}{\partial z \partial t^2} + f\frac{\partial^2 u}{\partial z \partial t} = \frac{\partial^2}{\partial t^2}\left(\frac{\partial w}{\partial y}\right) + \frac{g}{\rho_0}\left(\frac{\partial}{\partial y}\left[\frac{\partial \rho'}{\partial t}\right]\right). \tag{2.24}$$

Using (2.16) to eliminate all terms in ρ' gives

$$\frac{\partial^3 u}{\partial z \partial t^2} - f\frac{\partial^2 v}{\partial z \partial t} = \left(\frac{\partial^2}{\partial t^2} - \frac{g}{\rho_0}\frac{d\tilde{\rho}}{dz}\right)\frac{\partial w}{\partial x}, \tag{2.25}$$

$$\frac{\partial^3 v}{\partial z \partial t^2} + f\frac{\partial^2 u}{\partial z \partial t} = \left(\frac{\partial^2}{\partial t^2} - \frac{g}{\rho_0}\frac{d\tilde{\rho}}{dz}\right)\frac{\partial w}{\partial y}, \tag{2.26}$$

and taking the horizontal divergence: $\frac{\partial}{\partial x}(2.25) + \frac{\partial}{\partial y}(2.26)$, gives

$$\frac{\partial^3}{\partial z \partial t^2}\left(\frac{\partial u}{\partial x} + \frac{\partial v}{\partial y}\right) - f\frac{\partial^2}{\partial z \partial t}\left(\frac{\partial v}{\partial x} - \frac{\partial u}{\partial y}\right) = \left(\frac{\partial^2}{\partial t^2} - \frac{g}{\rho_0}\frac{d\tilde{\rho}}{dz}\right)\left(\frac{\partial^2 w}{\partial x^2} + \frac{\partial^2 w}{\partial y^2}\right). \tag{2.27}$$

We can also form a vorticity equation by taking the curl: $\frac{\partial}{\partial x}(2.13) - \frac{\partial}{\partial y}(2.12)$ to give

$$\frac{\partial}{\partial t}\left(\frac{\partial v}{\partial x} - \frac{\partial u}{\partial y}\right) + f\left(\frac{\partial u}{\partial x} + \frac{\partial v}{\partial y}\right) = 0. \tag{2.28}$$

Now using the vorticity equation (2.28), continuity (2.15), and the definition of N^2 (2.17), equation (2.27) becomes

$$\frac{\partial^2}{\partial t^2}\nabla^2 w + N^2\nabla_h^2 w + f^2\frac{\partial^2 w}{\partial z^2} = 0, \tag{2.29}$$

where $\nabla_h^2 = \left(\frac{\partial^2}{\partial x^2} + \frac{\partial^2}{\partial y^2}\right)$ is the horizontal Laplacian operator. A standard mathematical approach to solve equations such as (2.29) is to seek separable solutions of the form

$$w(\mathbf{x}, t) = F(x, y)W(z)\exp(i\omega t). \tag{2.30}$$

This leads to

$$\frac{1}{\omega^2 - f^2}\frac{\nabla_h^2 F}{F} = \frac{1}{N^2 - \omega^2}\frac{d^2W}{dz^2}\frac{1}{W} = -\lambda, \tag{2.31}$$

where λ is a separation constant which is the eigenvalue of the problem. Then we have

$$\nabla_h^2 F + (\omega^2 - f^2)\lambda F = 0, \tag{2.32}$$

$$\frac{d^2W}{dz^2} + (N^2(z) - \omega^2)\lambda W = 0. \tag{2.33}$$

Equation (2.32) is a second order equation with constant coefficients. Thus it seems sensible to set

$$\lambda = \frac{\kappa^2}{\omega^2 - f^2}, \tag{2.34}$$

where κ is a horizontal wavenumber $\kappa^2 = k^2 + l^2$. Equation (2.33) is a second order equation with non–constant coefficients, and with appropriate boundary conditions defines a so-called "Sturm–Liouville" type problem of the form

$$\frac{d^2W(z)}{dz^2} + \left(\frac{N^2(z) - \omega^2}{\omega^2 - f^2}\right)\kappa^2 W(z) = 0, \tag{2.35}$$

$$W(z = -d) = 0, \qquad W(z = 0) = 0. \tag{2.36}$$

These boundary conditions imply no vertical flow at the upper and lower boundaries (e.g. a rigid lid and a fixed bottom boundary). This "structure equation" for $W(z)$ can be solved for any stratification $N(z)$ with analytical approximative methods, e.g. WKB, as well as by numerical techniques, the latter being particularly appropriate for determining the eigenfrequencies of an observed density profile. Once $W(z)$ is known, we can apply the boundary condition

$$w(x = 0, z, t) = W(z) \cos \omega t, \tag{2.37}$$

to generate the internal wave modes for a given stratification $N(z)$.

2.3.2 Reflection at a slope

Linear internal wave reflection at a sloping bottom was treated analytically by Phillips Phillips (1977). The dispersion relation $\omega(\mathbf{k}) = 0$ for an internal gravity wave propagating in a linear stratification in a rotating domain is

$$\omega^2 = \frac{N^2 k^2 + f^2 m^2}{k^2 + m^2}, \tag{2.38}$$

where $\mathbf{k} = (k, 0, m)^T$ is the wavenumber which we have assumed, without loss of generality, is confined to the x–z plane. The corresponding phase velocity is

$$\mathbf{c}_p = \frac{\omega}{|\mathbf{k}|^2}\mathbf{k} = \frac{(N^2 k^2 + f^2 m^2)^{\frac{1}{2}}}{(k^2 + m^2)^{\frac{3}{2}}} (k, 0, m)^T, \tag{2.39}$$

and the group velocity is

$$\mathbf{c}_g = \frac{\partial \omega}{\partial \mathbf{k}} = \frac{km(N^2 - f^2)}{(N^2 k^2 + f^2 m^2)^{\frac{1}{2}} (k^2 + m^2)^{\frac{3}{2}}} (m, 0, -k)^T. \tag{2.40}$$

Note that $\mathbf{c}_g$ and $\mathbf{c}_p$ are orthogonal: $\mathbf{c}_g \cdot \mathbf{c}_p = 0$. We can also write the dispersion relation as

$$\frac{k}{m} = \left(\frac{\omega^2 - f^2}{N^2 - \omega^2} \right)^{\frac{1}{2}} = \tan \theta, \tag{2.41}$$

which defines the angle θ between the group velocity and the horizontal. Rewriting (2.38) in terms of this angle

$$\omega^2 = N^2 \sin^2 \theta + f^2 \cos^2 \theta, \tag{2.42}$$

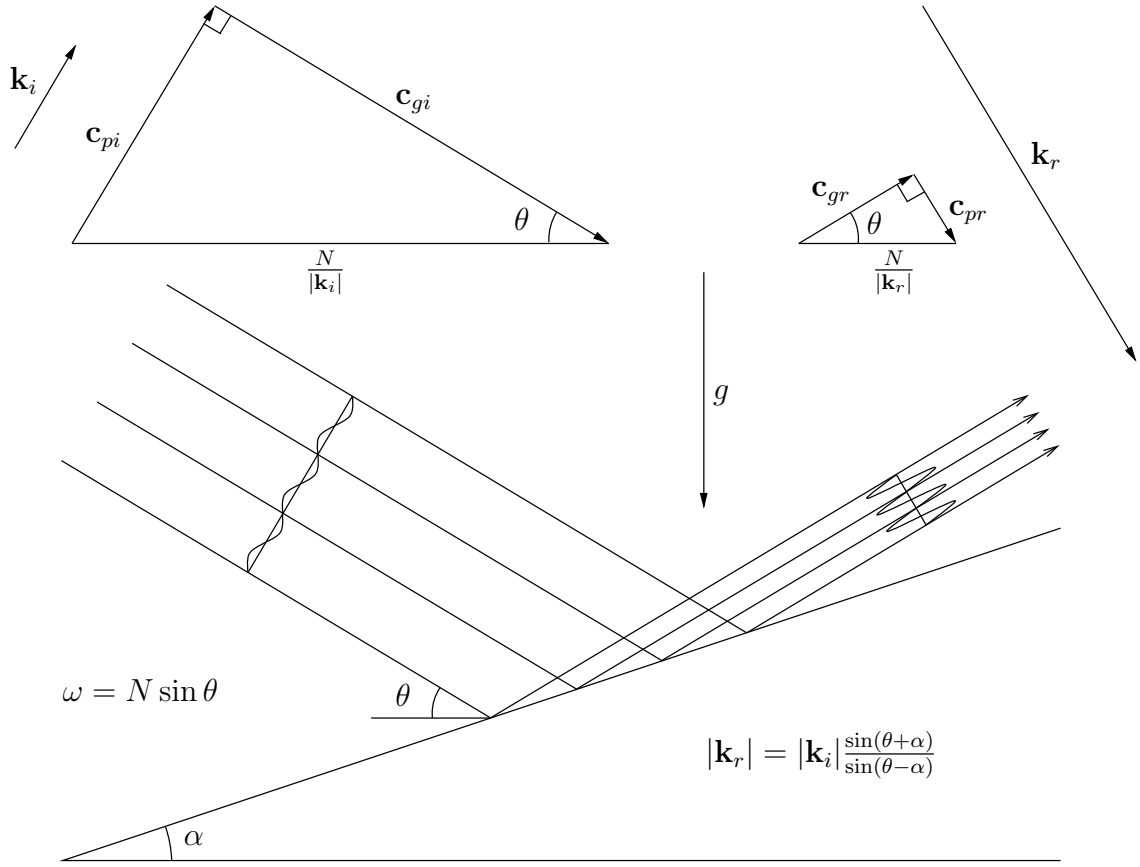


Figure 2.4: Reflection from a subcritical slope for the case $f = 0$. The group and phase velocities are smaller on reflection and the wavenumber and amplitude are greater by a factor of $\frac{\sin(\theta+\alpha)}{\sin(\theta-\alpha)}$. The subscript i denotes the incident wave and the subscript r the reflected wave.

shows that the angle at which energy propagates is independent of the wavenumber $\mathbf{k}$. An internal wave propagating in a linearly stratified fluid in a domain with horizontal boundaries can be described as a superposition of pairs of upward and downward propagating beams.

In acoustics and optics, the angles of incident and reflected wave beams are preserved with respect to the normal of the reflecting surface. The dispersion relation (2.49) shows that internal waves have rather different behaviour, with the angle between the wave beams and the horizontal preserved. Figure 2.4 illustrates the effect of reflection at a surface in a non–rotating domain ($f = 0$) on the group and phase velocities, amplitude and wavenumber, the subscript i denoting the incident wave and the subscript r the reflected wave.

For a slope less steep than the wavenumber of the incident reflection, ($\theta > \alpha$), a so-

called 'subcritical' slope, forward reflection occurs. For a 'supercritical' slope, ($\theta < \alpha$), backward reflection occurs. For a 'critical' slope, ($\theta = \alpha$), the linearised theory is no longer valid, as it predicts a reflected wave of infinite amplitude and infinitesimal group velocity. It is this case that is of most interest.

2.3.3 Dispersion relation

For a linear stratification, internal waves are plane waves, and we can consider three–dimensional solutions to the equations. We can derive the dispersion relation for a plane internal gravity wave by substituting a wave of the form $\exp\{i(kx + ly + mz - \omega t)\}$ into each of the governing equations to obtain a linear system of five homogeneous equations

$$
\begin{aligned}
-i\omega\hat{u} &- f\hat{v} &&+ \rho_0^{-1} ik\hat{p}' &&= 0, && (2.43)\\
f\hat{u} &- i\omega\hat{v} &&+ \rho_0^{-1} il\hat{p}' &&= 0, && (2.44)\\
&- i\omega\hat{w} &&+ \rho_0^{-1} im\hat{p}' &&+ \rho_0^{-1} g\hat{\rho}' = 0, && (2.45)\\
ik\hat{u} &+ il\hat{v} &&+ im\hat{w} &&= 0, && (2.46)\\
&- \frac{\rho_0 N^2}{g}\hat{w} &&- i\omega\hat{\rho}' &&= 0. && (2.47)
\end{aligned}
$$

This set of equations can be written as a matrix equation

$$
\begin{pmatrix}
1 & -\frac{if}{\omega} & 0 & -\frac{k}{\rho_0\omega} & 0 \\
\frac{if}{\omega} & 1 & 0 & -\frac{l}{\rho_0\omega} & 0 \\
0 & 0 & 1 & -\frac{m}{\rho_0\omega} & \frac{ig}{\rho_0\omega} \\
k & l & m & 0 & 0 \\
0 & 0 & -\frac{iN^2\rho_0}{g\omega} & 0 & 1
\end{pmatrix}
\begin{pmatrix}
\hat{u} \\ \hat{v} \\ \hat{w} \\ \hat{p}' \\ \hat{\rho}'
\end{pmatrix}
=
\begin{pmatrix}
0 \\ 0 \\ 0 \\ 0 \\ 0
\end{pmatrix}. \qquad (2.48)
$$

The solution is non–zero if the determinant of the 5×5 matrix vanishes. This leads to the dispersion relation

$$\omega^2 = \frac{N^2(k^2 + l^2) + f^2 m^2}{k^2 + l^2 + m^2}. \qquad (2.49)$$

This can also be written as

$$\omega^2 = N^2 \sin^2\theta + f^2 \cos^2\theta, \qquad (2.50)$$

where θ is the angle between the group velocity and the horizontal. Also, if we have $l = 0$, so that the wave is confined to the x–z plane, then we can write

$$\frac{k}{m} = \left(\frac{\omega^2 - f^2}{N^2 - \omega^2}\right)^{\frac{1}{2}} = \tan\theta, \tag{2.51}$$

and when there is no rotation, $f = 0$, this becomes

$$\omega = N \sin\theta. \tag{2.52}$$

2.3.4 Polarisation relations and boundary conditions

Eliminating u and v from (2.12) and (2.13) gives

$$\frac{\partial^2 u}{\partial t^2} + f^2 u = -\rho_0^{-1}\frac{\partial^2 p'}{\partial x \partial t} - f\rho_0^{-1}\frac{\partial p'}{\partial y}, \tag{2.53}$$

$$\frac{\partial^2 v}{\partial t^2} + f^2 v = -\rho_0^{-1}\frac{\partial^2 p'}{\partial y \partial t} + f\rho_0^{-1}\frac{\partial p'}{\partial x}. \tag{2.54}$$

Also, eliminating ρ' from (2.14) and (2.16) gives

$$\frac{\partial^2 w}{\partial t^2} + N^2 w = -\rho_0^{-1}\frac{\partial^2 p'}{\partial z \partial t}. \tag{2.55}$$

The polarisation relations can be found by substituting a plane wave form $\exp\{i(kx + ly + mz - \omega t\}$ into these equations and (2.16)

$$\frac{\hat{p}'}{\rho_0} = \hat{u}\left(\frac{\omega^2 - f^2}{k\omega + ifl}\right), \tag{2.56}$$

$$\hat{v} = \left(\frac{l\omega - ifk}{\omega^2 - f^2}\right)\frac{\hat{p}'}{\rho_0}, \tag{2.57}$$

$$\hat{w} = \left(\frac{-\omega m}{N^2 - \omega^2}\right)\frac{\hat{p}'}{\rho_0}, \tag{2.58}$$

$$\hat{\rho}' = \frac{i\rho_0 N^2}{g\omega}\hat{w}, \tag{2.59}$$

where the hats ($\hat{}$) denote the amplitude of the wave.

If we assume that $l = 0$ so that the wave vector is in the x–z plane, the first two of

these polarisation relations become

$$\frac{\hat{p}'}{\rho_0} = \hat{u}\left(\frac{\omega^2 - f^2}{k\omega}\right), \quad \hat{v} = \left(\frac{-ifk}{\omega^2 - f^2}\right)\frac{\hat{p}'}{\rho_0}, \tag{2.60}$$

and we have

$$\hat{v} = \left(\frac{-ikf}{\omega^2 - f^2}\right)\left(\frac{\omega^2 - f^2}{k\omega}\right)\hat{u} = -\hat{u}\frac{if}{\omega}, \tag{2.61}$$

$$\hat{w} = \left(\frac{-\omega m}{N^2 - \omega^2}\right)\left(\frac{\omega^2 - f^2}{k\omega}\right)\hat{u} = -\hat{u}\tan\theta, \tag{2.62}$$

$$\frac{\hat{\rho}'}{\rho_0} = -\hat{u}\frac{iN^2}{g\omega}\tan\theta. \tag{2.63}$$

Now $b' = -\frac{\rho'}{\rho_0}g$, so

$$\hat{b}' = \hat{u}\frac{iN^2}{\omega}\tan\theta. \tag{2.64}$$

Setting $\hat{u} = \frac{1}{2}iU_0$ gives the upward propagating ($k > 0$, $m > 0$) plane wave solution

$$u_{up}(x,z,t) = -\frac{1}{2}U_0[\sin(kx - \omega t)\cos mz + \cos(kx - \omega t)\sin mz], \tag{2.65}$$

$$v_{up}(x,z,t) = \frac{1}{2}U_0\frac{f}{\omega}[\cos(kx - \omega t)\cos mz - \sin(kx - \omega t)\sin mz], \tag{2.66}$$

$$w_{up}(x,z,t) = \frac{1}{2}U_0\tan\theta[\cos(kx - \omega t)\sin mz + \sin(kx - \omega t)\cos mz], \tag{2.67}$$

$$b'_{up}(x,z,t) = \frac{1}{2}\frac{N^2U_0}{\omega}\tan\theta[\sin(kx - \omega t)\sin mz - \cos(kx - \omega t)\cos mz]. \tag{2.68}$$

A plane wave solution of this form describes internal wave beams. However, such a solution is never going to satisfy the boundary conditions of no vertical velocity on the upper and lower boundaries (2.36). A rectangular domain acts as a waveguide, and the internal wave modes are a superposition of plane waves. We consider an internal wave as the sum of upward– and downward–propagating wave beams Thorpe and Haines (1987). A downward propagating wave is given by setting $m \mapsto -m$ which also implies

$\tan\theta \mapsto -\tan\theta$

$$
\begin{aligned}
u_{down}(x,z,t) &= -\frac{1}{2}U_0[\sin(kx-\omega t)\cos mz - \cos(kx-\omega t)\sin mz], && (2.69)\\
v_{down}(x,z,t) &= \frac{1}{2}U_0\frac{f}{\omega}[\cos(kx-\omega t)\cos mz + \sin(kx-\omega t)\sin mz], && (2.70)\\
w_{down}(x,z,t) &= \frac{1}{2}U_0\tan\theta[\cos(kx-\omega t)\sin mz - \sin(kx-\omega t)\cos mz], && (2.71)\\
b'_{down}(x,z,t) &= \frac{1}{2}\frac{N^2U_0}{\omega}\tan\theta[\sin(kx-\omega t)\sin mz + \cos(kx-\omega t)\cos mz]. && (2.72)
\end{aligned}
$$

Adding the upward and downward propagating waves

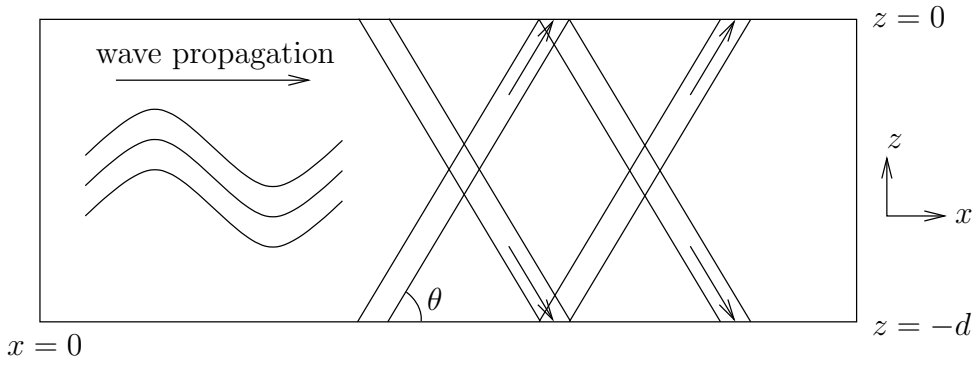


Figure 2.5: An internal wave as the superposition of upward and downward propagation wave beams.

$$
\begin{aligned}
u(x,z,t) &= -U_0\sin(kx-\omega t)\cos mz, && (2.73)\\
v(x,z,t) &= U_0\frac{f}{\omega}\cos(kx-\omega t)\cos mz, && (2.74)\\
w(x,z,t) &= U_0\tan\theta\cos(kx-\omega t)\sin mz, && (2.75)\\
b'(x,z,t) &= \frac{N^2U_0}{\omega}\tan\theta\sin(kx-\omega t)\sin mz. && (2.76)
\end{aligned}
$$

So, at $x = 0$, the boundary conditions that generate internal gravity waves in a linearly

stratified fluid are

$$u(0,z,t) = U_0 \cos mz \sin \omega t, \tag{2.77}$$

$$v(0,z,t) = U_0 \frac{f}{\omega} \cos mz \cos \omega t, \tag{2.78}$$

$$w(0,z,t) = U_0 \left(\frac{\omega^2 - f^2}{N^2 - \omega^2} \right)^{\frac{1}{2}} \sin mz \cos \omega t, \tag{2.79}$$

$$b'(0,z,t) = -\frac{N^2 U_0}{\omega} \left(\frac{\omega^2 - f^2}{N^2 - \omega^2} \right)^{\frac{1}{2}} \sin mz \sin \omega t. \tag{2.80}$$

2.4 Theory of internal waves in a two–layer fluid

2.4.1 Theory

The linear phase speed for a two layer fluid (2.1) is based upon potential theory (Segur and Hammack (1982))

$$c_0 = \sqrt{g' \frac{h_1 h_2}{h_1 + h_2}}, \tag{2.81}$$

and the first order correction is

$$c(a_0) = c_0 \left(1 + \frac{1}{2} \frac{a_0}{h} \right), \tag{2.82}$$

where $g' = g(\rho_2 - \rho_1)/\rho_0 = g\frac{\Delta\rho}{\rho_0}$ is the reduced gravity.

The corresponding wavelength is

$$L_w = k^{-1} = \left(\frac{4}{3} \frac{h_1^2 h_2^2}{a_0 (h_2 - h_1)} \right)^{\frac{1}{2}}. \tag{2.83}$$

The "thin thermocline" is described in (Phillips, 1977, p. 213) and is shown in figure 2.6. For this stratification the dispersion relation is

$$\omega^2 = g' k \left(k\epsilon + \coth kh_1 + \coth kh_2 \right)^{-1}, \tag{2.84}$$

so that the phase speed is

$$c^2 = g' \frac{1}{k} \left(k\epsilon + \coth kh_1 + \coth kh_2 \right)^{-1}. \tag{2.85}$$

It is possible to calculate the dispersion relation for a "tanh" thermocline (also shown in figure 2.6) in a domain with an infinite vertical extent (Roberts, 1975; Krauss, 1966), but for a finite domain requires numerical solution.

2.4.2 The Korteweg–de Vries equation

What follows is a brief outline for how one may derive the KdV equation from the Euler equations. The Euler equations take the form

$$\frac{\partial \mathbf{u}}{\partial t} + \mathbf{u}\cdot\nabla\mathbf{u} = -\frac{1}{\rho_0}\nabla p + \frac{\rho}{\rho_0}\mathbf{g}\,, \tag{2.86}$$

$$\frac{\partial \rho}{\partial t} + \mathbf{u}\cdot\nabla\rho = 0\,, \tag{2.87}$$

$$\nabla\cdot\mathbf{u} = 0\,, \tag{2.88}$$

which following linearisation, a density stratification for a two–layer fluid and a vertical slice geometry may be written as

$$\rho_0 u_t + p_x = 0\,, \tag{2.89}$$

$$p_z + g\rho = 0\,, \tag{2.90}$$

$$\rho_t + \Delta\rho\delta(z-h_2)w = 0\,, \tag{2.91}$$

$$u_x + w_z = 0\,, \tag{2.92}$$

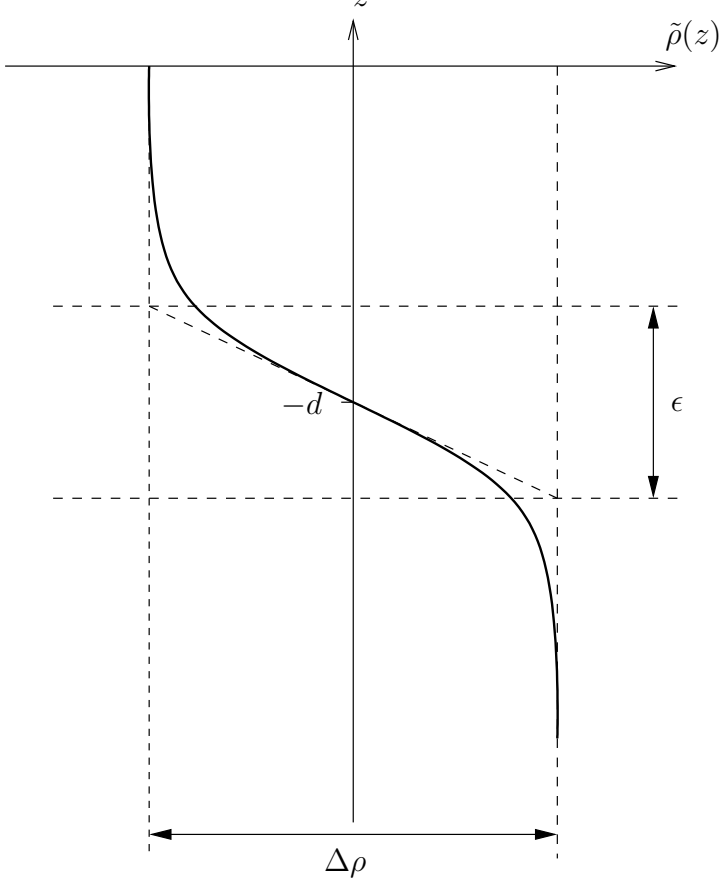
where $\delta(z)$ is a Dirac delta function and h_2 is the unperturbed depth of the interface. An asymptotic expansion in the small parameters $\frac{a}{h}$ and $\left(\frac{h}{l}\right)^2$, where a is the amplitude of the wave, h is the depth of the domain and l is the length of the wave leads to the KdV equation:

$$\eta_t + c_0\left(1+\frac{3}{2}\frac{\eta}{h}\right)\eta_x + \frac{1}{6}c_0^2h^2\eta_{xxx} = 0, \tag{2.93}$$

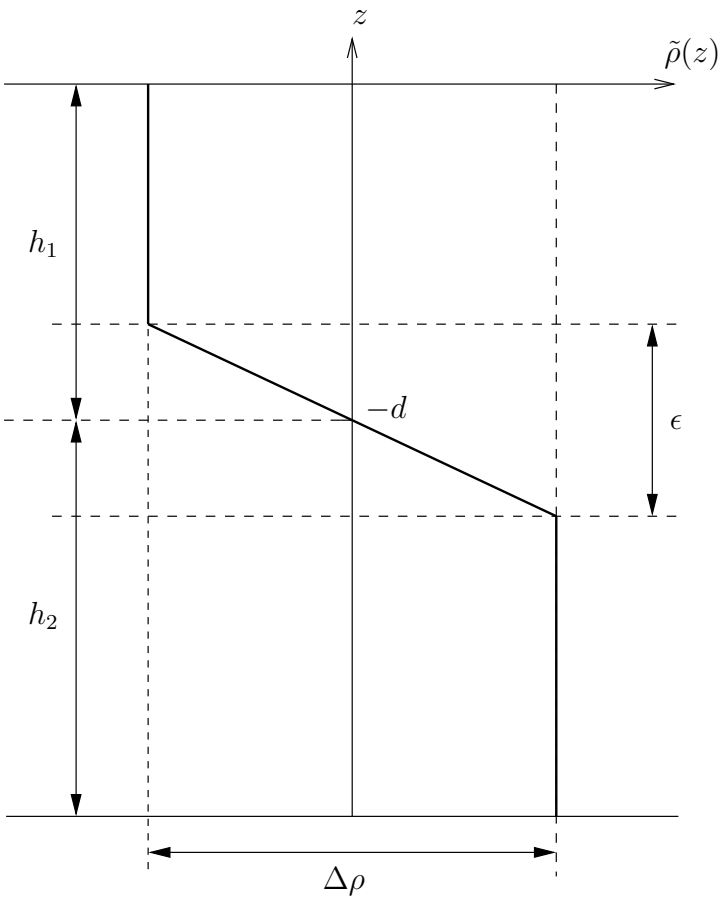
which admits the solution

$$\eta = \eta_0\,\mathrm{sech}^2\left(\left(\frac{3\eta_0}{4h^3}\right)^{\frac{1}{2}}(x-ct)\right) \tag{2.94}$$

(Whitham, 1974, Section 13.11). We thus use a sech^2 functional form as an initial condition for solitary waves in a two–layer fluid.



(a) Tanh thermocline.



(b) Thin thermocline.

Figure 2.6: Two descriptions of a two-layer fluid with an interface of thickness ϵ.

2.4.3 Energy and mixing of stratified fluids

In order to examine the effectiveness of numerical simulation methods the energy budget in the system is considered.

2.4.3.1 Boussinesq equations

We start with the Boussinesq equations

$$\frac{\partial \mathbf{u}}{\partial t} + \mathbf{u} \cdot \nabla \mathbf{u} = -\frac{1}{\rho_0} \nabla p + \frac{\rho}{\rho_0} \mathbf{g} + \nu \nabla^2 \mathbf{u} \,, \tag{2.95}$$

$$\frac{\partial \rho}{\partial t} + \mathbf{u} \cdot \nabla \rho = \kappa \nabla^2 \rho \,, \tag{2.96}$$

$$\nabla \cdot \mathbf{u} = 0 \,, \tag{2.97}$$

where t is time, $\mathbf{u}$ is the velocity vector, p is the pressure, and ρ is the density. ν is the kinematic viscosity and κ is the diffusivity. $\mathbf{g}$ is gravity, $\mathbf{g} = (0, -g)^T$ in two dimensions and $\mathbf{g} = (0, 0, -g)^T$ in three dimensions.

2.4.3.2 Energy equation

Taking the scalar product of $\rho_0 \, \mathbf{u}$ and equation (2.95) gives

$$\rho_0 \mathbf{u} \cdot \frac{\partial \mathbf{u}}{\partial t} + \rho_0 \mathbf{u} \cdot (\mathbf{u} \cdot \nabla \mathbf{u}) = -\mathbf{u} \cdot \nabla p - g \rho w + \rho_0 \nu \mathbf{u} \cdot \nabla^2 \mathbf{u} \,, \tag{2.98}$$

and using the two vector identities

$$\nabla \cdot \left(\mathbf{u} \tfrac{1}{2} u^2 \right) = \mathbf{u} \cdot (\mathbf{u} \cdot \nabla \mathbf{u}) + \tfrac{1}{2} u^2 \nabla \cdot \mathbf{u} \,, \tag{2.99}$$

$$\nabla \cdot \left(\nabla \tfrac{1}{2} u^2 \right) = \mathbf{u} \cdot \nabla^2 \mathbf{u} + \nabla \mathbf{u} : \nabla \mathbf{u} \,, \tag{2.100}$$

where : denotes the tensor inner product

$$\nabla \mathbf{u} : \nabla \mathbf{u} = \sum_{i,j} \frac{\partial u_i}{\partial x_j} \frac{\partial u_i}{\partial x_j}, \tag{2.101}$$

along with continuity (2.97) gives the **kinetic energy equation**

$$\frac{\partial}{\partial t}\left(\tfrac{1}{2}\rho_0 u^2\right) + \nabla \cdot \mathbf{f}_{KE} = -\rho g w - \nu \rho_0 \nabla \mathbf{u} : \nabla \mathbf{u}\,, \tag{2.102}$$

where,

$$\mathbf{f}_{KE} = \left(p + \tfrac{1}{2}\rho_0 u^2\right)\mathbf{u} - \nu \nabla\left(\tfrac{1}{2}\rho_0 u^2\right)\,, \tag{2.103}$$

is the kinetic energy flux vector. Taking the product of gz and equation (2.96)

$$gz\frac{\partial \rho}{\partial t} + gz\mathbf{u}\cdot\nabla\rho \quad = \quad gz\kappa\nabla^2\rho\,, \tag{2.104}$$

and using the relations

$$\nabla\cdot(\mathbf{u}\rho g z) \quad = \quad \rho g w \quad + \quad gz\mathbf{u}\cdot\nabla\rho\,, \tag{2.105}$$

$$\nabla\cdot\nabla(\rho g z) \quad = \quad gz\nabla^2\rho \quad + \quad 2g\frac{\partial\rho}{\partial z}\,, \tag{2.106}$$

gives the **potential energy equation**

$$\frac{\partial}{\partial t}(\rho g z) + \nabla\cdot\mathbf{f}_{PE} = \rho g w - 2\kappa g\frac{\partial\rho}{\partial z}\,, \tag{2.107}$$

where,

$$\mathbf{f}_{PE} = \rho g z\mathbf{u} - \kappa\nabla(\rho g z)\,, \tag{2.108}$$

is the potential energy flux vector. Integrating equations (2.102) and (2.107) over a fixed volume V gives

$$\begin{aligned}\frac{d}{dt}\int_V \tfrac{1}{2}\rho_0 u^2\,dV \quad &= \quad -\oint_S \mathbf{n}\cdot\mathbf{u}\left(p+\tfrac{1}{2}\rho_0 u^2\right)\,dS + \oint_S \nu\mathbf{n}\cdot\nabla\left(\tfrac{1}{2}\rho_0 u^2\right)\,dS \\ &\quad -\int_V \rho g w\,dV - \int_V \rho_0\nu\nabla\mathbf{u}:\nabla\mathbf{u}\,dV, \end{aligned}\tag{2.109}$$

$$\begin{aligned}\frac{d}{dt}\int_V \rho g z\,dV \quad &= \quad -\oint_S \mathbf{n}\cdot\mathbf{u}\rho g z\,dS + \oint_S \kappa\mathbf{n}\cdot\nabla(\rho g z)\,dS \\ &\quad +\int_V \rho g w\,dV - 2\kappa g\int_V\frac{\partial\rho}{\partial z}\,dV. \end{aligned}\tag{2.110}$$

where S is the bounding surface of the volume V. Imposing no normal flow boundary conditions

$$\mathbf{n} \cdot \mathbf{u} \quad = \quad 0 \qquad \text{on} \quad S, \tag{2.111}$$

gives the final energy equations

$$\frac{d}{dt}\int_V \tfrac{1}{2}\rho_0 u^2 \, dV \quad = \quad \oint_S \nu \mathbf{n} \cdot \nabla \left(\tfrac{1}{2}\rho_0 u^2\right) \, dS \quad - \int_V \rho g w \, dV - \int_V \rho_0 \nu \nabla \mathbf{u} : \nabla \mathbf{u} \, dV, \tag{2.112}$$

$$\frac{d}{dt}\int_V \rho g z \, dV \quad = \quad \oint_S \kappa \mathbf{n} \cdot \nabla(\rho g z) \, dS \qquad + \int_V \rho g w \, dV - 2\kappa g \int_V \frac{\partial \rho}{\partial z} \, dV, \tag{2.113}$$

or

$$\frac{dK}{dt} \quad = \quad -\nu_S + H - \epsilon, \tag{2.114}$$

$$\frac{dP}{dt} \quad = \quad -\kappa_S - H + D_p, \tag{2.115}$$

where

$$\begin{aligned} K &= \int_V \frac{1}{2}\rho_0 u^2 \, dV, & P &= \int_V \rho g z \, dV, \\ \nu_s &= -\oint_S \nu \mathbf{n} \cdot \nabla \left(\tfrac{1}{2}\rho_0 u^2\right) \, dS, & H &= -\int_V \rho g w \, dV, \\ \epsilon &= \int_V \rho_0 \nu \nabla \mathbf{u} : \nabla \mathbf{u} \, dV, & \kappa_s &= -\oint_S \kappa \mathbf{n} \cdot \nabla(\rho g z) \, dS, \\ D_p &= -2\kappa g \int_V \frac{\partial \rho}{\partial z} \, dV, \end{aligned} \tag{2.116}$$

are the kinetic energy (K), the potential energy (P), the rate at which kinetic energy is lost through viscous diffusion across the boundaries of the domain (ν_s), the buoyancy flux (H), the rate of viscous dissipation of kinetic energy to internal energy (ϵ), the rate at which potential energy is lost through diffusion out of the boundaries of the domain (κ_s), and the rate at which internal energy is converted to potential energy through diffusion of the stratification (D_p). The potential energy P is then split into available and backround potential energies

$$P \quad = \quad P_A + P_B, \tag{2.117}$$

such that

$$\frac{dP_A}{dt} = -H - M, \tag{2.118}$$

$$\frac{dP_B}{dt} = D_p - \kappa_S + M, \tag{2.119}$$

where M is the rate of mixing, which always acts to increase the background potential energy P_B. These energy fluxes are summarised in figure 2.7. Internal and external energies are included in this diagram. Although an internal energy equation is not used in Fluidity–ICOM, for example, to explicitly include the generation of heat by viscous damping and the subsequent effect on density through the equation of state, there is an implicit assumption of specific internal energy in the system in that diffusive processes on the microscopic scale are included through the $\kappa\nabla^2\rho$ term in equation (2.96). This explains the conversion of internal energy to potential energy through the diffusion of the stratification (D_p). Indeed, the system can be closed energetically by writing the internal (E_{int}) and external (E_{ext}) energies as

$$\frac{dE_{\text{int}}}{dt} = \epsilon - D_p, \tag{2.120}$$

$$\frac{dE_{\text{ext}}}{dt} = \nu_S + \kappa_S, \tag{2.121}$$

so that the total energy $E_{\text{total}} = K + P_A + P_B + E_{\text{int}} + E_{\text{ext}}$ satisfies

$$\frac{dE_{\text{total}}}{dt} = 0. \tag{2.122}$$

If the boundary conditions imposed are not no normal flow boundary conditions, the first terms of the right hand side of equations (2.109) and (2.110) can also be included in equation (2.121) as

$$\frac{dE_{\text{ext}}}{dt} = \nu_S + \kappa_S + \oint_S \mathbf{n}\cdot\mathbf{u}\left(p + \tfrac{1}{2}\rho_0 u^2 + \rho g z\right)\, dS\,. \tag{2.123}$$

The background potential energy P_B is obtained by adiabatically restratifying the fluid into its least potentially energetic state. This does not change the probability density function of the densities of the fluid parcels. We can then calculate the rate of mixing M

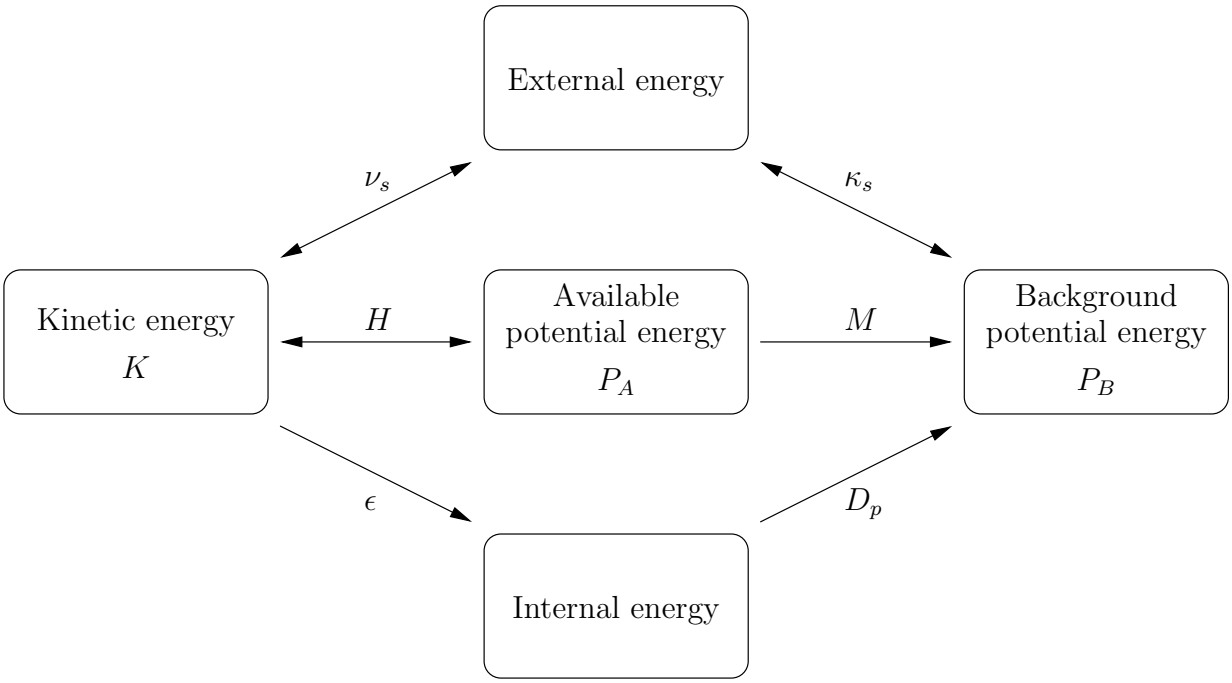


Figure 2.7: Energy fluxes in a stratified fluid. The symbols are defined in equations (2.116), (2.118) and (2.119). Adapted from Winters et al. (1995).

from equation (2.119), since D_p and κ_S are easily calculated, as

$$M = \frac{dP_B}{dt} + \kappa_S - D_p. \tag{2.124}$$

2.4.3.3 Calculating the background potential energy

The background potential energy is given by

$$P_B = g \int_V \rho z^*(\mathbf{x}, t)\, dV\,, \tag{2.125}$$

where $z^*(\mathbf{x}, t)$ is the vertical position in the reference state of the fluid parcel at position $(\mathbf{x}, t)$. $z^*(\mathbf{x}, t)$ is then given by

$$z^*(\mathbf{x}, t) = \frac{1}{A} \int H(\rho(\mathbf{x}', t) - \rho(\mathbf{x}, t)) dV', \tag{2.126}$$

where H is the Heaviside step function

$$H(\xi) = \begin{cases} 0 & \text{for} \quad \xi < 0, \\ \frac{1}{2} & \text{for} \quad \xi = 0, \\ 1 & \text{for} \quad \xi > 0. \end{cases} \tag{2.127}$$

z^* has dimensions of length and can be considered as an isopycnal coordinate, that is, the function $z^*(\mathbf{x}, t)$ has the same value at all points on a given isopycnal surface (and so is a unique function of the density).

2.4.3.4 Pseudoenergy

Lamb and Nguyen (2009) derive the mechanical energy equation as described above, but go further in defining an expression for local available potential energy density (rather than a global one). They go on to show that the sum of the kinetic and available potential energies – the pseudoenergy – is conserved when the effects of viscosity and diffusivity are ignored and when the reference density state used to calculate the available potential energy density is independent of time. The corresponding energy flux is $\mathbf{u}(K + P_A + p_d)$, where p_d is the pressure perturbation relative to the reference density. This is what is used to calculate the incident and reflected energy at the slope, rather than using an assumption of equipartition of energy to estimate the (available) potential energy, which is typically done for laboratory simulations (Helfrich (1992)), and in some numerical simulations (Bourgault and Kelley (2007)).

Chapter 3

Literature Review

Contents

3.1 Generation of internal waves 47

3.1.1 Surface generation 47

3.1.2 Bottom generation 48

3.1.3 Interior generation 50

3.2 Observational techniques 51

3.3 Mathematical theory 52

3.4 Linear stratification 53

3.5 Two-layer fluid 53

3.6 Energetics of internal waves 55

3.1 Generation of internal waves

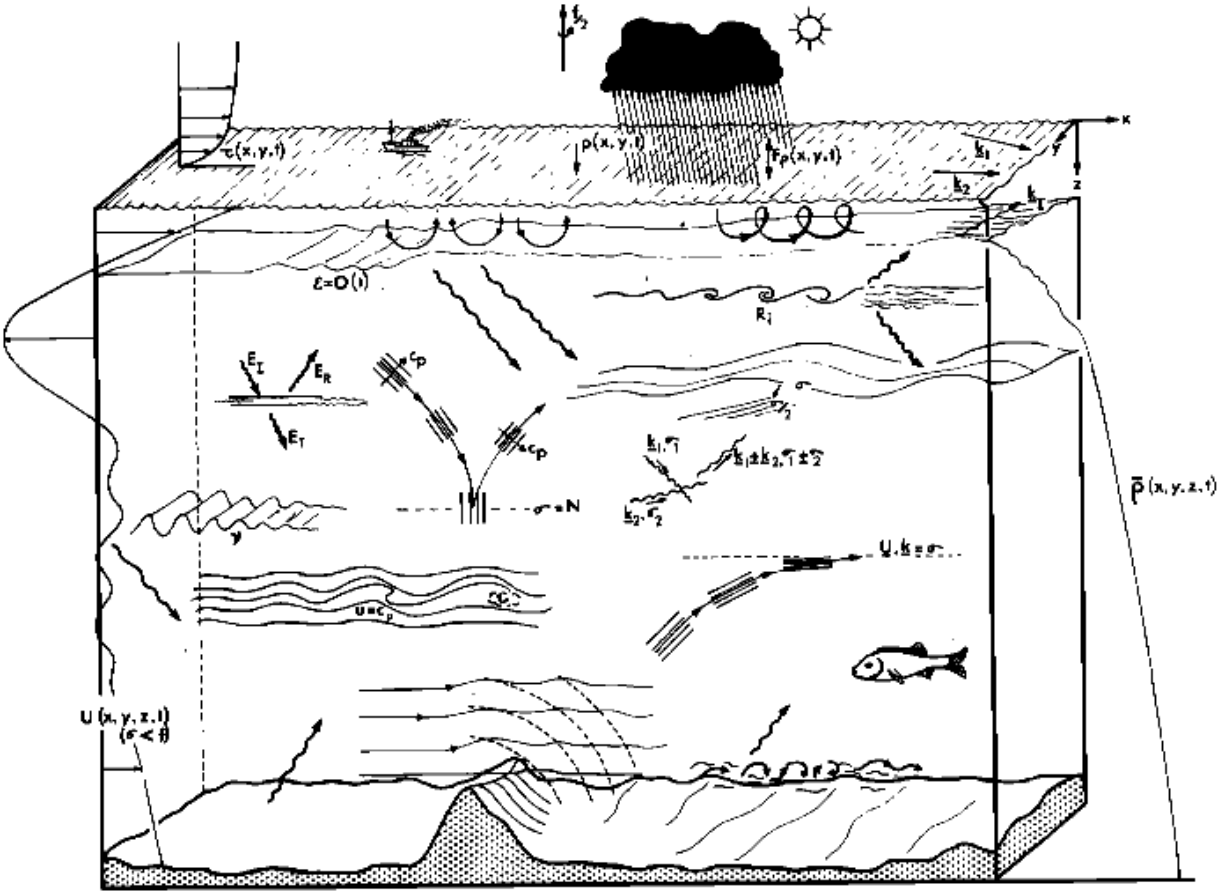


Figure 3.1: Schematic of processes affecting internal waves in the ocean taken from Thorpe (1975). His figure caption is "As a challenge, the reader is left to decipher the symbols himself." The key features regarding generation of internal waves are the wind stress and barotropic flow over topography as described in section (3.1).

Thorpe (1975) discussed several potential mechanisms proposed for the generation of internal waves, and summarised them into a schematic diagram of physical processes affecting internal waves, as shown in figure (3.1). Here we concentrate on the generation of internal waves at the surface and bottom of the ocean, as well as the interior.

3.1.1 Surface generation

Thorpe (1975) suggests several mechanisms for internal wave generation at the ocean surface: travelling pressure fields, variable wind stress, variable buoyancy flux, and the interaction of a pair of surface waves, with the first two being the most important.

The observations by Ekman (1904) of dead water prompted the study of travelling pressure fields as a generation mechanism, and more recently, Dotsenko (1991) estimated the parameters of internal waves in the wake of a steadily moving pressure anomaly for average stratifications typical in the Caribbean Sea, and concluded that this is a feasible generation mechanism of internal waves but that their amplitudes are comparatively low.

Alford (2001) estimated the energy flux from the wind to near-inertial internal wave motions in the mixed layer between 50°S and 50°N as $(0.98 \pm 0.08) \times 10^{-3}$ W m^{-2}, for a total power of 0.29 TW, making wind-driven generation of internal waves an important contributor to in the global energy budget, see figure (2.3).

3.1.2 Bottom generation

Tidally driven barotropic flow of stratified fluid over continental slopes and shelves, seamounts and mid-ocean ridges is the main mechanism by which baroclinic internal waves are generated in the ocean. Maxworthy (1979) carried out laboratory experiments of tidal flow of stratified fluid over a three-dimensional obstacle to explain field observations of internal waves in Massachusetts Bay. The Froude number, Fr, defined as the ratio of the maximum upstream tidal velocity to the phase speed of long, small-amplitude waves in the given stratification, characterises the flow. For values above a critical value of the Froude number, a downstream depression is formed, which moves upstream when the tide turns and evolves into a sequence of solitary waves. This is sometimes referred to as the lee wave generation mechanism, which is examined in section 7.1.1.

Matsuura and Hibiya (1990) made detailed comparisons between laboratory and numerical experiments of tidal flow of a stratified fluid over a large amplitude obstacle, and classified the response with two non-dimensional parameters, the Froude number and the period of the flow normalised to the time taken for an internal wave to travel over the obstacle. They found that for Froude numbers greater than one, internal waves were generated which propagate upstream, and depending on the normalised time-scale interacted with the waves formed on the other side of the obstacle.

Kranenburg and Pietrzak (1989) investigated internal lee-wave formation in an estuary with a small topographic feature. Their laboratory observations on the wavelength of the lee-wave compared favourably with a derived analytical solution. Numerical work by

Labeur and Pietrzak (2004) examined this problem numerically with FINEL3D.

Pietrzak and Labeur (2004) used FINEL3D to numerically simulate trapped internal wave generation prompted by observations of internal wave activity in the Rotterdam waterway, to investigate the time-dependent and non-linear behaviour not covered by the linear theory.

Shaw et al. (2009) used a non-hydrostatic numerical model to study the generation of internal solitary waves by barotropic tidal flow over a ridge in an idealised oceanic setting to identify the conditions that affect the generation of internal solitary waves in the northern South China Sea.

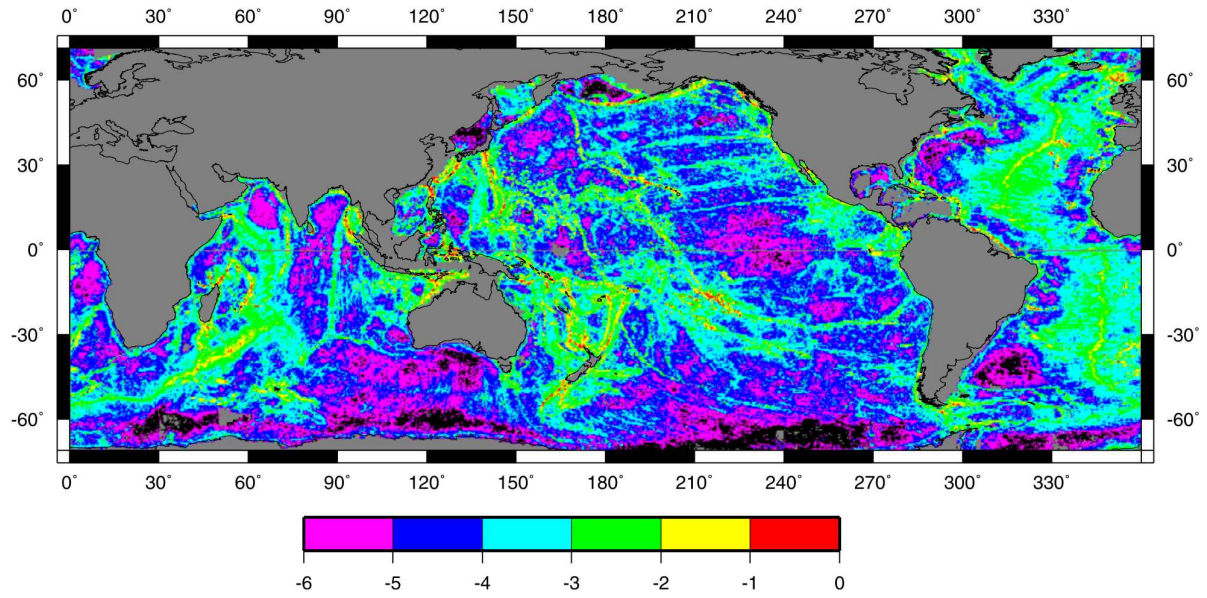


Figure 3.2: Global distribution of the energy flux from the semidiurnal tide to internal waves, from Nycander (2005). The units are $\mathrm{W\,m^{-2}}$, with the colour bar logarithmic. Black is less than $10^{-6}\mathrm{W\,m^{-2}}$.

Nycander (2005) performed a direct computation of the tidal generation of internal waves over the global ocean based on linear wave theory and high-resolution bathymetry. The geographical distribution of the energy flux due to the semi-diurnal tide is shown in figure 3.2. The largest values occur in regions of steep topography, for example at the Mid-Atlantic ridge, and the smallest values are found in flat regions, for example around Antarctica. The total flux over the area with depth greater than 500 m is 1.2 TW.

Lim et al. (2008) investigated the generation of internal waves by the interaction of barotropic flow of a two layer fluid with a continental shelf/slope topography and classified

the response into four regimes which depended on the Froude number and depth ratio of the two layer fluid in the shallow shelf region: wave of depression; internal surge; internal bolus; and no waves.

Gostiaux and Dauxois (2007) carried out a simple laboratory experiment to study internal tide generation due to interaction of barotropic flow of linearly stratified fluid with a steep continental shelf, and drew comparison with the generation of wave beams by an oscillating cylinder in a stratified fluid (see section 3.1.3).

Lamb (2004) studied numerically tidal flow over supercritical (see section 2.3.2) topography. Higher harmonic internal wave beams were generated, and the nonlinear interaction between different harmonics was investigated with harmonic analysis.

3.1.3 Interior generation

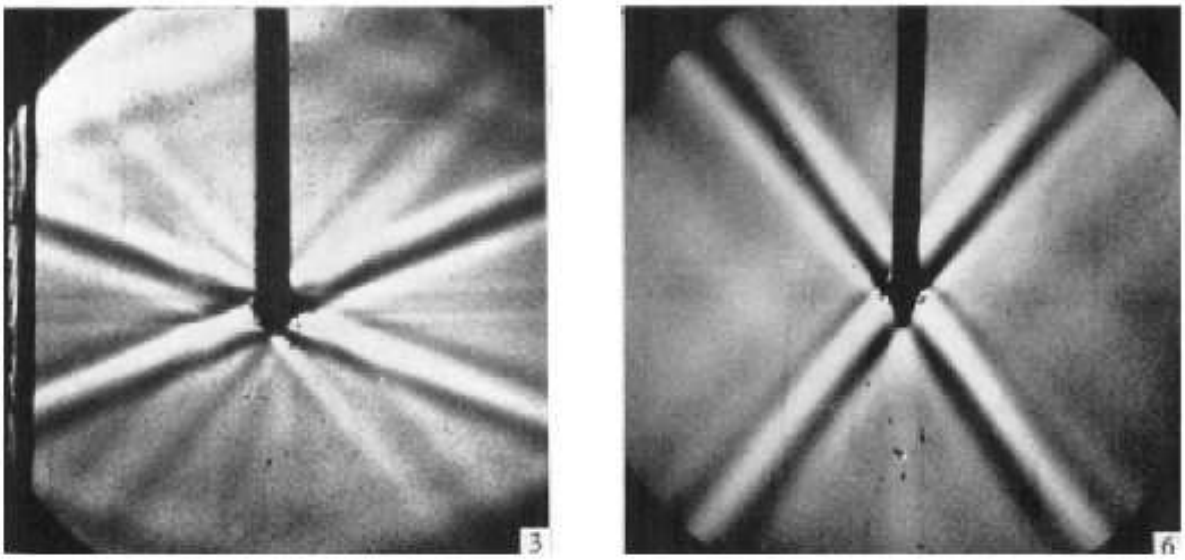


Figure 3.3: Wave beams of the St. Andrew's Cross. This is a synthetic schieleren photograph which visualises density perturbations in the fluid. The image on the left has oscillation to buoyancy frequency ratio 0.366 , and the image on the right has ratio 0.699. Image taken from Mowbray and Rarity (1967).

Another generation mechanism, which is used in the laboratory, is a cylinder oscillating in a stratified fluid with a frequency less than the buoyancy frequency. Mowbray and Rarity (1967) conducted experiments to test the linear theory of internal gravity waves produced by an oscillating cylinder in a stably stratified fluid, where they observed the famous St. Andrew's Cross pattern, see figure 3.3. While this is more of an interesting laboratory

scale phenomenom, with no oceanographic analogue, this simple problem is an excellent test-case of the ability of a numerical model to accurately represent internal waves.

Javam et al. (1999) generated internal waves using a localised standing wavelike momentum source with frequency ω by including a $f(x,z)\sin\omega t$ term in the z–momentum equation, where $f(x,z)$ is a localisation function. In the subsequent interaction with a slope, they found higher mode waves were produced by non–resonant nonlinear interactions, which could not propagate as they had frequencies greater than the local buoyancy frequency.

3.2 Observational techniques

Internal waves have structure in the horizontal and vertical directions as well as being time dependent, constrained by the dispersion relation, equation (2.49). The generation of a time history of the three–dimensional (3D) structure of internal waves therefore requires a complex array of sensors which is rarely available.

Moored sensors can provide a vertical profile of velocity and temperature at a fixed location. Current meters, consisting of a rotor for speed and a vane for direction, are attached to an essentially vertical mooring line between the sea floor and a buoyant float at or below the sea surface. Temperature fluctuations can be measured at similar locations, providing an estimate of the instantaneous vertical velocity component using $w = -(\partial T/\partial t)/(\partial T/\partial z)$, provided that the horizontally advective and diffusive terms are unimportant in the temperature equation (Garrett and Munk, 1979). By using a number of sensors at different vertical spacings on the same mooring, or on several moorings separated by various distances horizontally, a more complete picture of the structure of internal waves can be discerned (e.g. IWEX array).

Towed sensors, such as a thermistor chain (which consists of a cable with temperature sensors every few metres), can be suspended below a ship and towed slowly through the upper layers of the ocean. They provide a two–dimensional section of the temperature structure of the top 200 m of ocean. Dropped sensors are the traditional way to measure vertical structure in the oceans. The expendable bathythermograph (XBT) is dropped from a moving ship to measure the temperature profile down to 750 m. Conductivity–temperature–depth (CTD) casts record electrical conductivity and temperature (and thus

salinity and density) as functions of depth.

Cairns' yo–yo capsule is an instrument that freely drifts with the mean current whilst yo–yoing up and down approximately 15 m about an isotherm, sensing temperature and pressure. The autonomous underwater glider "Spray" has been used in Monterey Bay 2006 project. A Spray glider with Precision Measurement Engineering (PME) CTD maintained a "synthetic mooring" station in the Monterey Underwater Canyon in order to describe internal waves as they propagate up the Canyon.

The Acoustic Doppler Current Profiler (ADCP) estimates horizontal and vertical velocity as a function of depth by using the Doppler effect to measure the radial relative velocity between the instrument and suspended particulate matter in the ocean. The intensity of the backscatter signal can be used to calculate a density profile of the internal waves. Since internal waves are not directly visible, they can only be observed by their surface signature and by direct measurements of the pycnocline or thermocline. In areas where the density interface is shallow enough to permit the internal wave crests to interact with the sea surface, the waves can be detected by the resulting increased roughness of the surface ocean. Surface roughness can be photographed distinctly with the use of Synthetic Aperture Radar (SAR) imagery.

3.3 Mathematical theory

Stokes (1847) and Rayleigh (1883) were the first to consider internal waves mathematically. Linear internal wave reflection at a sloping bottom was treated analytically by Phillips (1977) (see section 2.3.2).

Gilbert and Garrett (1989), using two–dimensional theory for the scattering of internal waves off smoothly varying topography developed by Baines (1971a,b), calculated time–averaged kinetic energy densities for locally convex and concave topographies. Their results suggested that locally convex sites are more likely to show energy enhancement near the critical frequency (at which the angle of the group velocity to the horizontal matches that of the topography) than at locally concave slopes.

Dauxois and Young (1999) used matched asymptotic expansions to examine the near–critical reflection of a weakly nonlinear internal gravity wave from a sloping boundary in a uniformly stratified fluid. This weakly nonlinear theory gave rise to a final description

that is a linear equation.

3.4 Linear stratification

Cacchione and Wunsch (1974) were the first to study small amplitude mode one internal waves propagating in a fluid with constant buoyancy frequency into a shoaling region in a laboratory simulation. Their simulations were carried out with subcritical, critical and supercritical slopes (see section 2.3.2). For subcritical slopes, the amplitude and wavenumber changed according to the linear theory derived by Phillips (1977). They found that for reflection at the critical angle, the strong shearing motion becomes unstable and forms a series of periodic vortices with horizontal axes in the boundary layer, which locally mixed the fluid. For supercritical slopes, the waves did not break but nonlinear processes were important.

Legg and Adcroft (2003) investigated numerically the mixing that results when a baroclinic internal tide reflects from sloping topography with the non–hydrostatic Massachusetts Institute of Technology General Circulation Model (MITgcm). Although their calculations were two–dimensional, they included the Coriolis effect in their treatment. They found no evidence of enhanced energy dissipation at convex topography as suggested by Gilbert and Garrett (1989).

Venayagamoorthy and Fringer (2005, 2006, 2007), simulated numerically "highly nonlinear" waves on a laboratory scale with the Stanford unstructured non–hydrostatic terrain–following adaptive Navier–Stokes simulator (SUNTANS). Although they did not include rotation (which would have been fairly irrelevant on the laboratory scale), they do have some detailed 3D results of the evolution of bore–like features, "boluses", which exhibit similar behaviour to the turbulent break–up of a gravity current, via the "lobe and clef" instability.

3.5 Two-layer fluid

Kao et al. (1985) investigated in the laboratory the evolution and breaking of a solitary wave as it shoals on a sloping bottom up onto a shallower shelf region. They looked at the critical Richardson number criterion $Ri < \frac{1}{4}$ for the onset of the shoaling instability.

Vlasenko and Hutter (2002) performed numerical simulations of the breaking of internal solitary waves over a shelf-slope topography. They determined a breaking criterion for wave propagating onto the shelf based on the depths of the two fluids on the shelf and the amplitude of the wave. They also found a breaking criterion of internal solitary waves over the slope.

Helfrich (1992) carried out laboratory experiments of shoaling internal solitary waves of depression in a two-layer fluid, and found the waves break and and form a series of boluses or surges that propagate up the slope. He calculated the mixing efficiency, or fraction of the energy that goes into vertical mixing, to be $15(\pm 5)\%$.

Michallet and Ivey (1999) carried out similar experiments in the laboratory and varied several parameters, including the angle of the slope, fluid thickness ratios and density ratios. They found that the amount of energy reflected from the slope depended on the ratio of the length of the solitary wave and the length of the slope, and that mixing efficiency peaked at a maximum of 25% when this ratio was equal to 0.5, and a decrease in efficiency for ratios greater than and less than 0.5.

Boegman et al. (2005) also performed similar experiments and used an appropriate form of the Iribarren number, or surf similarity parameter, which is defined as the ratio of the boundary slope to the wave slope, as the independent variable for energy loss at the slope and mixing efficiency so that they could generalise their results to an oceanographic context.

Bourgault and Kelley (2007) also used the Iribarren number as an independent variable for the energy reflected at the slope in their numerical simulations, and proposed a tentative parameterisation for the reflectance coefficient (the ratio of reflected energy to incident energy). They suggested that Michallet and Ivey (1999) had underestimated the reflectance coefficient, but also that because their two-dimensional model did not explicitly resolve sidewall friction, they did not draw a firm conclusion.

Bourgault et al. (2007) then compared the results of Bourgault and Kelley (2007) to field observations. They estimated the energy of several leading solitary-like waves in the St. Lawrence Estuary, and using the tentatative parameterisation in Bourgault and Kelley (2007) estimated the energy reflected.

Vlasenko and Stashchuk (2007) performed three-dimensional (3D) numerical simula-

tions of internal wave shoaling with problem parameters (stratification and bottom topography) chosen to mimic those found in the northern Andaman Sea. They found that the evolution of 3D internal waves was quite different from the two-dimensional (2D) shoaling because of wave refraction at local depressions and elevations in the bathymetry, e.g, as would occur at canyons in the continental slope. Also, the wave refraction led to faster wave breaking than in the 2D case. They concluded that it should be expected that one finds regions of greater turbulent kinetic energy in regions of bottom elevations, and lesser turbulent kinetic energy in regions of depression.

Berntsen et al. (2006) compared the numerical models the Bergen Ocean Model (BOM) and the MITgcm with regards their relative merits in modelling internal solitary wave breaking. They followed one of the experiments carried out in Michallet and Ivey (1999). They found good comparison between models and laboratory results, which they attributed to the simple configuration and the small-scale nature of the problem.

Thiem and Berntsen (2009) carried out numerical simulations of the breaking and shoaling of large-amplitude solitary waves with the BOM, using similar initial conditions to Berntsen et al. (2006), but on a larger scale. They found enhanced horizontal velocities on the slope of up to 1 $\mathrm{m\,s^{-1}}$, but also that these maximum velocities were very much dependent on the grid resolution of the model and the sub-grid scale closure used.

Rickard et al. (2009) performed numerical simulations using an adaptive mesh model Gerris, with a similar configuration to Helfrich (1992) and Michallet and Ivey (1999). They checked the consistency of the adaptive model using convergence tests, finding good convergence. They compared their results with Helfrich (1992), in particular comparing the number of boluses formed as a function of the wavelength. They also calculated the reflection coefficient as a function of the Iribarren number, and compared their result with the parameterisation of Bourgault and Kelley (2007).

3.6 Energetics of internal waves

Many of the papers discussed in section 3.5 discuss the energetics of internal wave breaking. Here we concentrate on energy of stratified fluids and the consequences of mixing through internal wave breaking, as the consideration of an energy budget in a stratified fluid allows the energy that is lost through vertical diffusion of the ambient stratification to be separated

from that lost due to the wave breaking process.

Winters et al. (1995), Peltier and Caulfield (2003) and Tseng and Ferziger (2001) discuss mixing of stratified fluids in terms of available and background potential energy, the concept of which was first introduced by Lorenz (1955). The background potential energy is the minimum potential energy that can be achieved by adiabatically restratifying the fluid, and changes only through irreversible diapycnal mixing, providing a direct measure of the energy lost through mixing. Lamb and Nguyen (2009) calculated the energy flux at a slope of internal solitary waves, having derived an expression for available potential energy density, and did not assume the equipartition of kinetic and (available) potential energies.

Helfrich (1992), Michallet and Ivey (1999), Bourgault and Kelley (2007), Boegman et al. (2005) all consider the amount of energy reflected at a slope, but none explicitly calculate the energy lost through diapycnal mixing. We calculate this energy loss chapter 7 using the concepts discussed in Winters et al. (1995) and Peltier and Caulfield (2003). However, Fringer and Street (2003) did use these techniques to consider the energy lost due to shear instability of interfacial waves.

Venayagamoorthy and Fringer (2005) calculated the energy flux contributions from the non-hydrostatic pressure and nonlinear terms and found that they were a significant part of the total energy flux.

Chapter 4

Numerical Model — The Imperial College Ocean Model

Contents

4.1 Unstructured meshes and mesh adaptivity 59

4.1.1 Unstructured meshes 59

4.1.2 Mesh adaptivity 61

4.2 The finite element method 62

4.3 Discretisation of the advection-diffusion equation 64

4.3.1 Weak forms of the equations 64

4.3.2 Basis functions 65

4.4 Discretisation of the Navier-Stokes equations 66

4.4.1 Discretisation with the P_1P_1 finite element pair 66

4.4.2 A projection based solution procedure for velocity and pressure . 68

4.5 Representing balance in large scale geophysical problems . . 69

4.6 Control volume discretisation of scalar equations 69

4.7 Boundary conditions 71

4.8 The time loop 72

4.9 Mesh adaptivity 74

4.9.1 Error measures 74
4.9.2 Mesh optimisation methods 75

4.1 Unstructured meshes and mesh adaptivity

4.1.1 Unstructured meshes

Unstructured meshes can represent a computational domain in an arbitrary fashion with variable sized triangular (in 2D) or tetrahedral (in 3D) elements. For this reason, they are often used to model problems in complex domains such as flow past the exterior of vehicles and aircraft (Peraire and Morgan, 1997; Weatherill et al., 2002), or flow through pipes (Benhamadouche and Laurence, 2003; Moulinec et al., 2005). Finite volume or finite element discretisation methods are usually used in conjunction with unstructured meshes.

Structured meshes have a uniform topological structure, *i.e.* it is implicitly known that the node with indices (i, j) is connected to those with indices $(i-1, j), (i+1, j-1)$ *etc.* They are usually composed of a uniform or slowly varying resolution, and cannot conform to complex geometries, in contrast to unstructured meshes. Finite difference discretisation methods are typically used with structured meshes.

The domains which geophysical fluid dynamics modelling generally require (*i.e.* those with complex coastlines and bathymetry) would suggest that using unstructured meshes is the more sensible approach. There are several advantages in using unstructured meshes in geophysical fluid dynamics modelling. They can represent the domain more accurately and efficiently, as well as focusing resolution in an anisotropic fashion, *e.g.* increased resolution in the direction normal to a coastline or bottom boundary without increasing the resolution in the tangential direction. This allows boundary layers to be resolved without having to increase the resolution globally. The use of increased resolution in regions of interest can also be used to more accurately represent shallow regions while the bathymetry of the deep ocean is sub-sampled. This allows seas or a coastal region of particular interest to be more accurately modelled within an entire global ocean model, thereby removing problems associated with open boundaries. Using unstructured meshes on the sphere also removes problems associated with singularities at the poles.

Representing topography with structured meshes presents several difficulties. The discontinous 'staircase' representation generally leads to spurious accelerations when modelling flow over topography. One approach to overcome this problem with z-coordinate models is to use shaved or partial elements to represent sloping bathymetry, for instance as

used by Adcroft et al. (1997). Haidvogel et al. (1991) have used sigma coordinates, but this choice of vertical coordinate can lead to errors in horizontal pressure gradient calculations, particularly with steep topographies (Mellor et al., 1998). Similar pressure gradient errors can occur with unstructured meshes, but these can be overcome by splitting the pressure either into hydrostatic and non-hydrostatic parts (see section 4.5). One drawback of the sigma coordinate approach is that the number of vertical levels is constant over the entire domain, with the result that resolution could be too coarse in deep regions, or too fine in shallow coastal areas, leading to computational inefficiency or certain features of the flow being under resolved. The hybrid vertical coordinate (Griffies et al., 2000; Chassignet et al., 2003) follows sigma coordinates in the shallow regions, z-coordinates in unstratified regions, and isopycnal coordinates in stratified regions, allowing different dynamics to be accurately modelled simultaneously with the most appropriate vertical coordinate.

Work by Kramer and Stelling (2008) extended the cut cell methodology to improve the representation of coastal boundaries in structured mesh models, by producing unstructured grids at the boundaries while maintaining structured grids in the interior. The orthogonality of the grid at the boundaries enables accurate pressure gradient calculations. Casulli and Stelling (2011) employed subgrid scale representation of bathymetry in both structured and unstructured meshes to efficiently calculate mass and momentum balance in shallow water flow in complex domains, negating the need for grid refinements.

Nested meshes have in common with unstructured meshes the benefit of enhanced resolution in regions of importance, but at the same time require *a priori* knowledge of where these important regions are, in addition to causing potential problems with reflections at the interface between the different resolutions (Laugier et al., 1996; Ly and Luong, 1999).

Time dependent features such as eddies, fronts, convection events and internal wave breaking, require the use of adaptive meshes to place enhanced resolution in regions where the most efficient use of finite computational resources may be made, but not at the expense of under-resolving the rest of the domain. The use of adaptive meshes in a structured mesh framework is possible, but it is easier to build adaptive mesh algorithms based on unstructured meshes. This also enables resolution to vary smoothly, and in an anisotropic fashion, overcoming the problems associated with using nested techniques and hierarchical refinement in structured meshes.

4.1.2 Mesh adaptivity

The dynamics in the ocean occur across a large range of scales, both spatially and temporally. These processes can be coupled, and so all dynamical features of a simulation, if not appropriately parameterised, need to be adequately resolved. The use of adaptive meshes allows this range of scales to be captured in a more computationally efficient manner, that is, with fewer degrees of freedom. Fixed mesh models, on the other hand, which are usually strucured, would require a large amount of computional resources to capture this large range of scales. Unstructured meshes do require an extra computational overhead, and adaptive mesh models demand extra resources to calculate error measures to guide where extra resolution is required, as well as interpolating solutions onto a new mesh. The adaptive mesh approach can be more cost effective, especially for problems that include transient solution structures where computational resources can be focused in the most efficient manner. In particular, and considered here in this work, the adaptive mesh approach lends itself to modelling the range of scales involved in internal wave breaking.

Adaptivity has been used in conjunction with structured mesh models in the form of AMR (Berger and Oliger, 1984), which are a form of time dependent nested meshes, and so share some of the problems of nested models such as being refined in an isotropic fashion and the difficulty of representing boundaries and topography.

4.2 The finite element method

Finite element methods have been used in the study of oceanography for several decades. Early work included that by Fix (1975), Haidvogel et al. (1980), Davies (1980) and Dumas et al. (1982). Tidal and coastal problems have been examined with shallow water models employing finite element methods by Lynch and Gray (1979), Le Provost and Vincent (1986), Le Provost et al. (1994), Lynch et al. (1996) and Lyard et al. (2006). Some finite element and finite volume ocean models which are based on unstructured meshes are now briefly summarised.

QUODDY is a 3D hydrostatic finite element model (*e.g.* Lynch et al. (1996)) used for coastal and shelf applications. In the horizontal, an unstructured mesh of linear triangles is used along with sigma coordinates in the vertical.

The FEOM finite element model (Danilov et al., 2004; Wang et al., 2008; Danilov et al., 2008) is a 3D hydrostatic model using linear, and more recently non-conforming, tetrahedral elements unstructured in the horizontal with a combination of z and sigma coordinates in the vertical. Galerkin least-squares discretisation methods are employed for stability. More recent work has shifted the focus to a finite volume approach (Danilov, 2012).

FINEL3D (Labeur and Pietrzak, 2004) is a 3D non-hydrostatic finite element method model unstructured in the horizontal and vertical which employs the mini element.

The SLIM finite element model (*e.g.* White et al. (2008)) is a 3D hydrostatic model, unstructured with a ${P_1}^{\mathrm{NC}}P_1$ finite element representation in the horizontal, and a z-level prismatic mesh in the vertical. Shaved cells are used to represent bathymetry.

SUNTANS (Fringer et al., 2006) is a 3D finite volume model which is unstructured in the horizontal with prismatic z-levels in the vertical and an immersed boundary method to represent bathymetry. It includes non-hydrostatic dynamics and has been used in the simulation of internal waves.

H2Ocean (Cui et al., 2010) is a 3D non-hydrostatic unstructured mesh finite volume model. It uses a finite volume analogue of the ${P_1}^{\mathrm{NC}}P_1$ finite element.

FVCOM (Chen et al., 2003) is a 3D hydrostatic finite volume model designed for use in coastal applications. It is unstructured in the horizontal and uses sigma coordinates in

the vertical. Horizontal components of velocity are stored at element centroids with other components stored at element vertices.

Gerris (Popinet and Rickard, 2007) is a 3D non-hydrostatic finite volume model which uses an A-grid formulation and includes a method to allow for implicit damping of instabilities generally associated with the A-grid, while accurately preserving dispersive properties and geostrophic balance. It has an adaptive mesh refinement capability based on a hierarchical quadtree method.

Fluidity–ICOM is a 3D non-hydrostatic finite element ocean model designed for both large and small scale applications. It uses unstructured meshes in all three dimensions and is the only model to make use of anisotropic adaptive meshes in 3D.

4.3 Discretisation of the advection-diffusion equation

4.3.1 Weak forms of the equations

The advection-diffusion equation models the transport of scalar quantities such as temperature

$$\frac{\partial c}{\partial t} + \boldsymbol{u} \cdot \nabla c = \nabla \cdot (\kappa \nabla c) + f \quad \text{in } \Omega, \tag{4.1}$$

where c is the scalar quantity being modelled, $\boldsymbol{u}$ is the velocity, κ is a tensor of diffusivities and f is a source term. The natural boundary condition is

$$\boldsymbol{n} \cdot (\kappa \nabla c) = 0 \quad \text{on } \partial\Omega. \tag{4.2}$$

Equation 4.1 is multiplied by a test function ϕ and then integrated over the domain to give the weak formulation of the advection-diffusion equation

$$\int_\Omega \frac{\partial c}{\partial t} \phi \, d\Omega + \int_\Omega (\boldsymbol{u} \cdot \nabla c) \phi \, d\Omega = \int_\Omega (-\kappa \nabla c \cdot \nabla \phi + f\phi) \, d\Omega, \tag{4.3}$$

with integration by parts being used on the second order terms. The boundary condition (4.2) has been used to remove the surface integral and to include it in the formulation.

This is called the weak formulation since the requirement on the smoothness of the solution has been weakened. This must be considered when constructing basis functions to represent the solution (Gresho and Sani, 1998; Zienkiewicz et al., 2005).

The finite element method is now invoked by assuming a discrete finite-dimensional form for the solution $c = \sum_{j=1}^{\mathrm{N}} c_j \psi_j$. Here, ψ_j is 'trial' function from an N-dimensional subspace of the infinite dimensional space where the exact solution of the equation is located. This form is then substituted into (4.3). In the Galerkin finite element method, a finite-dimensional subset of the test functions is taken such that $\psi = \phi$, which gives the

resulting matrix system for the unknowns c_j, $j = 1, \ldots, \mathrm{N}$

$$\sum_{j=1}^{\mathrm{N}} \underbrace{\int_\Omega \phi_i \phi_j \, d\Omega}_{M_{ij}} \frac{dc_j}{dt} + \sum_{j=1}^{\mathrm{N}} \underbrace{\int_\Omega \phi_i \boldsymbol{u} \cdot \nabla \phi_j \, d\Omega}_{T_{ij}} \; c_j + \sum_{j=1}^{\mathrm{N}} \underbrace{\int_\Omega \kappa \nabla \phi_i \cdot \nabla \phi_j \, d\Omega}_{D_{ij}} \; c_j = \underbrace{\int_\Omega f \phi_i \, d\Omega}_{F_i},$$

for $i = 1, \ldots, \mathrm{N}$. This can be written in matrix form as

$$\boldsymbol{M} \frac{d\boldsymbol{c}}{dt} + \boldsymbol{T}\boldsymbol{c} + \boldsymbol{D}\boldsymbol{c} = \boldsymbol{F},$$

where $\boldsymbol{c} = (c_1, \ldots, c_{\mathrm{N}})^T$.

The theta method (Gresho and Sani, 1998) for temporal discretisation gives the fully discrete system

$$(\boldsymbol{M} + \Delta t \theta (\boldsymbol{T} + \boldsymbol{D}))\, \boldsymbol{c}^{n+1} = (\boldsymbol{M} - \Delta t (1-\theta)(\boldsymbol{T} + \boldsymbol{D}))\, \boldsymbol{c}^n + \boldsymbol{F}^{n+\theta},$$

with the superscripts denoting the time level and $\theta \in [0, 1]$. Choosing $\theta = 0.5$ gives the Crank-Nicolson discretisation, which is second-order accurate in time, and is the value used for the simulations presented later in this work.

4.3.2 Basis functions

For a patch of elements that contain node j, the piecewise-linear continuous basis function ϕ_j is defined so that it takes the value 1 at the central node (node j) of the patch and is zero at all other nodes of the mesh, *i.e.* ϕ has compact support. The discrete solution is now defined as a continuous piecewise-linear function with value c_j at node j. Other options for basis functions are available, such as higher order and discontinuous functions.

4.4 Discretisation of the Navier-Stokes equations

The 3D non-hydrostatic Boussinesq equations in a domain $V \subset \mathbb{R}^3$,

$$\begin{aligned} \frac{\partial \boldsymbol{u}}{\partial t} + \boldsymbol{u}\cdot\nabla\boldsymbol{u} + 2\boldsymbol{\Omega}\times\boldsymbol{u} &= -\nabla p - \rho g\boldsymbol{k} + \nabla\cdot\boldsymbol{\tau} + \boldsymbol{F}, && \text{(4.4a)} \\ \nabla\cdot\boldsymbol{u} &= 0, && \text{(4.4b)} \\ \frac{\partial T}{\partial t} + \boldsymbol{u}\cdot\nabla T &= \nabla\cdot(\boldsymbol{\kappa}\nabla T), && \text{(4.4c)} \\ \rho &\equiv \rho(T). && \text{(4.4d)} \end{aligned}$$

describe the dynamics of the ocean. $\boldsymbol{u}$ is the 3D velocity vector, t is time, p is the perturbation pressure, g is the acceleration due to gravity, T is the temperature and ρ is the perturbation density, with the assumption that buoyancy acts in the vertical. $\boldsymbol{\tau}$ is the deviatoric stress tensor which is used to model viscous effects. $\boldsymbol{\kappa}$ is the thermal diffusivity tensor which is assumed to be diagonal. The rotation vector is $\boldsymbol{\Omega} = (0, 0, \Omega_z)^T$, where $\Omega_z = 7.292 \times 10^{-5}\,\mathrm{rad\,s^{-1}}$ for calculations on the globe. For simulations in smaller, flat domains the f-plane approximation can be used where $2\boldsymbol{\Omega} = (0, 0, \Omega_z \sin(\psi_0))^T$ and ψ_0 is the latitude for the domain. Finally, $\boldsymbol{F}$ contains additional source terms such as a quadratic drag term to simulate sidewall friction in a 2D simulation.

4.4.1 Discretisation with the P_1P_1 finite element pair

The domain V is partitioned into an unstructured mesh of tetrahedra with N the time dependent number of nodes in the mesh. The finite element basis functions used in this work are continuous piecewise linear elements. The numerical approximations to the velocity, pressure and temperature are represented as

$$\begin{aligned} \boldsymbol{u} \equiv (u, v, w)^{\mathrm{T}} &\approx \sum_{j=1}^{\mathrm{N}} (\mathbf{u}_j(t), \mathbf{u}_{\mathrm{N+j}}(t), \mathbf{u}_{\mathrm{2N+j}}(t))^{\mathrm{T}} \phi_j(\boldsymbol{x}), \\ p &\approx \sum_{j=1}^{\mathrm{N}} \mathbf{p}_j(t)\phi_j(\boldsymbol{x}), \quad T \approx \sum_{j=1}^{\mathrm{N}} \mathbf{T}_j(t)\phi_j(\boldsymbol{x}). \end{aligned}$$

These forms for $\boldsymbol{u}$, p and T are substituted into (4.4). Galerkin projection in space and theta differencing in time results in the discrete momentum equation

$$(M_L + \theta\Delta t A)\left(\frac{\mathbf{u}^{n+1} - \mathbf{u}^n}{\Delta t}\right) = -A\mathbf{u}^n + C\mathbf{p}^{n+1/2} - G\boldsymbol{\rho}'^{n+1/2} + \mathbf{f}^{n+1/2}, \tag{4.5}$$

the discrete continuity equation

$$C^{\mathrm{T}}\mathbf{u}^{n+1} = \mathbf{0}, \tag{4.6}$$

and the discrete temperature equation

$$(M'_L + \theta\Delta t H)\,\mathbf{T}^{n+1} = (M'_L - (1-\theta)\Delta t H)\,\mathbf{T}^n.$$

Homogeneous Neumann boundary conditions, *i.e.* free stress and zero heat flux, have been assumed for simplicity. Δt is the time step size, superscripts denote the time level and $A \equiv A(\tilde{\mathbf{u}}) = N(\tilde{\mathbf{u}}) + L - D$. M'_L and M_L are the diagonal lumped mass matrices obtained by summing the rows of M' and M which are given by

$$M \equiv \mathrm{diag}(M', M', M'), \quad \text{where} \quad M'_{ij} = \int_V \phi_i(\boldsymbol{x})\phi_j(\boldsymbol{x})\,dV, \quad \text{for } 1 \le i, j \le \mathrm{N}.$$

The Coriolis and buoyancy terms are defined with

$$L \equiv 2\Omega_z \begin{pmatrix} 0 & -M' & 0 \\ M' & 0 & 0 \\ 0 & 0 & 0 \end{pmatrix}, \quad G \equiv g \begin{pmatrix} 0 & 0 & 0 \\ 0 & 0 & 0 \\ 0 & 0 & M' \end{pmatrix}, \quad \boldsymbol{\rho}' \equiv \begin{pmatrix} 0 \\ 0 \\ \boldsymbol{\rho} \end{pmatrix}.$$

The matrix $N(\tilde{\mathbf{u}})$ is the result of discretising the nonlinear advection terms

$$N(\tilde{\mathbf{u}}) \equiv \mathrm{diag}(N', N', N'), \quad \text{where} \quad N'_{ij}(\tilde{\mathbf{u}}) = \int_V \phi_i(\boldsymbol{x})\tilde{\mathbf{u}} \cdot \nabla\phi_j(\boldsymbol{x})\,dV, \quad \text{for } 1 \le i, j \le \mathrm{N},$$

The viscous terms are represented via the matrix D. The vector $\mathbf{f}$ represents external forcing, for instance a quadratic sidewall friction. The matrix $-C$ represents the discrete form of the gradient operator with

$$C \equiv (C^1, C^2, C^3)^T, \quad C^q_{ij} = \int_V \phi_j(\boldsymbol{x})\frac{\partial\phi_i(\boldsymbol{x})}{\partial x_q}\,dV, \quad 1 \le i, j \le \mathrm{N}; q = 1, 2, 3,$$

and so C^T represents the discrete divergence operator. Finally the matrix H represents diffusion and is given by

$$H_{ij} = \int_V \left(\phi_i \tilde{\mathbf{u}}^n \cdot \nabla \phi_j + \boldsymbol{\kappa}_{lm} \frac{\partial \phi_j}{\partial x_m} \frac{\partial \phi_i}{\partial x_l} \right) dV, \quad \text{for } 1 \leq i, j \leq \mathrm{N}.$$

A Galerkin method is used for momentum here, which is non-dissipative and non-stabilised. To guarantee boundedness and stability, a flux-limited control volume finite element extension to the above is employed for the tracer fields (section 4.6).

4.4.2 A projection based solution procedure for velocity and pressure

A projection method to decouple the velocity and pressure solutions is employed for better computational efficiency. Firstly, equation (4.5) is solved for a velocity prediction $\mathbf{u}_*^{n+1}$ using the old pressure $\mathbf{p}^{n-1/2}$ instead of $\mathbf{p}^{n+1/2}$. $\mathbf{u}_*^{n+1}$ will not usually satisfy the discrete continuity equation (4.6) and so velocity and pressure are modified with a discrete irrotational correction of the form

$$M_L \mathbf{u}^{n+1} = M_L \mathbf{u}_*^{n+1} + \Delta t C \Delta \mathbf{p} \tag{4.7}$$

so that continuity $C^T \mathbf{u}^{n+1} = \mathbf{0}$ is satisfied at the end of each timestep. The discretised elliptic problem for $\Delta \mathbf{p}$

$$C^{\mathrm{T}} M_L^{-1} C \Delta \mathbf{p} = -\frac{C^{\mathrm{T}} \mathbf{u}_*^{n+1}}{\Delta t}.$$

is obtained by multiplying equation (4.7) through by $C^{\mathrm{T}} M_L^{-1}$, and applying continuity. This discretisation method can result in singularities and so a pressure filter K representing a discretisation of a fourth order operator is applied. K is given by the matrix $K = Q^T M_L^{-1} Q$, where Q is the matrix defined by

$$Q_{ij} = \frac{1}{2} \int_V (\nabla \phi_i)^T \, \overline{\overline{h}} \, \nabla \phi_j \, dV,$$

and $\overline{\overline{h}}$ is a tensor representing local element size. The pressure update is now

$$(C^{\mathrm{T}} M_L^{-1} C + K) \Delta \mathbf{p} = -\frac{C^{\mathrm{T}} \mathbf{u}_*^{n+1}}{\Delta t} - K \mathbf{p}_*^{n+1/2} \tag{4.8}$$

with $\mathbf{p}_*^{n+1/2}$ the pressure at the new time level from the previous nonlinear iteration. Now that $\Delta\mathbf{p}$ has been obtained from equation (4.8), equation (4.7) gives $\mathbf{u}^{n+1}$, and pressure is $\mathbf{p}_*^{n+1/2} = \mathbf{p}^{n-1/2}$.

4.5 Representing balance in large scale geophysical problems

In large scale geophysical problems with stratification and rotation, the buoyancy and Coriolis terms are the dominant terms in the equation and are largely balanced by a pressure gradient

$$2\boldsymbol{\Omega} \times \boldsymbol{u} + \rho \boldsymbol{g} \approx -\nabla p_{hg}, \tag{4.9}$$

where p_{hg} is some part of the full dynamic pressure. Here, a P_1P_1 velocity-pressure finite element pair, where both velocity and density, as well as pressure, are represented with piecewise linear elements, has been used. It can be seen that the left hand side of equation (4.9) has a continuous piecewise linear representation, whereas the right hand side has a discontinuous piecewise constant representation. This can lead to numerical errors and spurious accelerations.

One approach to overcome this problem is to split the pressure into hydrostatic (p_h) and non-hydrostatic (p_{nh}) parts, with p_h balancing the buoyancy force: $\partial p_h/\partial z = -\rho g$. p_h is now represented more accurately with a higher order element than those used to represent velocity and pressure, with quadratic elements being used in this case. p_{nh} is calculated using a standard finite element and ensures that the velocity field is divergence free.

4.6 Control volume discretisation of scalar equations

A control volume method is employed in this work to prevent spurious overshoots and undershoots in the calculation of the advection of scalar fields. The advection-diffusion equation is rewritten with the advection term represented as the difference between a conservative term and a velocity divergence term:

$$\frac{\partial c}{\partial t} + \nabla \cdot \boldsymbol{u} c - c \nabla \cdot \boldsymbol{u} = \nabla \cdot (\kappa \nabla c) + f \quad \text{in } \Omega \tag{4.10}$$

with c the scalar field, $\boldsymbol{u}$ a the velocity, κ is the diffusivity and f a source term. A dual mesh of control volumes is formed around the nodes of the parent mesh. A test function ϕ, which is piecewise constant in these control volumes, is multiplied by equation (4.10) and then integrated by parts to leave surface integrals around each control volume

$$\int_{\Omega_{CV}} \frac{\partial c}{\partial t}\phi \, d\Omega + \int_{\partial\Omega_{CV}} (\boldsymbol{u}\cdot\boldsymbol{n})c\phi \, d\partial\Omega - \int_{\Omega_{CV}} (\nabla\cdot\boldsymbol{u})c\phi \, d\Omega \tag{4.11}$$
$$= \int_{\partial\Omega_{CV}} (\boldsymbol{n}\cdot\kappa\boldsymbol{q})\phi \, d\partial\Omega + \int_{\Omega_{CV}} f\phi \, d\Omega,$$

$$\int_{\Omega_{CV}} \boldsymbol{q}\phi \, d\Omega = \int_{\partial\Omega_{CV}} u\boldsymbol{n}\phi \, d\partial\Omega. \tag{4.12}$$

The auxiliary variable, $\boldsymbol{q}$, has been introduced as a result of the second derivative in the diffusion term, and is governed by an equation (4.12) that is local to the control volume, Ω_{CV}.

c and $\boldsymbol{q}$ are not defined on the faces of the dual mesh, but appropriate values can be calculated with the following methods. The method of Bassi and Rebay (1997) is used for the diffusion term. The unknown u and the auxiliary variable $\boldsymbol{q}$ are calculated by taking their average in the control volumes on either side of the face.

The original mesh is used to calculate the interpolated values at the faces of the control volumes for the advection terms, but this does not in general result in a bounded flux. The value at the face is calculated with the method of Sweby (1984). More detailed explanation of this method is given in Wilson (2009).

4.7 Boundary conditions

Boundary conditions can now be imposed to close the system. Such a boundary condition might be imposing no normal flow on all the boundaries of the domain as used in section 5.4.2, or more complex time and space dependent boundary conditions on certain boundaries to generate internal waves such as $\boldsymbol{u} \cdot \boldsymbol{n} = U_0 \cos mz \sin \omega t$.

4.7.0.1 Dirichlet condition for a scalar field

A Dirichlet condition on the boundary $\partial\Omega$ for a scalar field like temperature T is

$$T = \tilde{T}, \quad \text{on} \quad \partial\Omega.$$

which is applied via the 'big-spring' method (see Smith and Griffiths (1998) section 3.8 for example) in Fluidity–ICOM.

4.7.0.2 Dirichlet condition for momentum

The boundary condition for momentum is set by prescribing all components of velocity. At the boundary where internal waves are generated, the normal component of velocity is specified as

$$u(0, z, t) = U_0 \cos mz \sin \omega t, \tag{4.13}$$

and the velocity in the tangential direction as

$$w(0, z, t) = U_0 \omega (N^2 - \omega^2)^{-\frac{1}{2}} \sin mz \cos \omega t, \tag{4.14}$$

When all components are specified to be zero, this is referred to as a no-slip boundary condition.

4.8 The time loop

Internal waves are a time-dependent process, and so an algorithm is needed to advance the numerical solution in time. This is acheived in Fluidity–ICOM with the non-linear Picard iteration scheme, where each of the coupled equations are solved using the best available solution for the other variables at that point in the timestep.

As before, the numerical solution of the tracer field c is given by the vector $\mathbf{c}$ with $\mathbf{c} = (c_1, ..., c_N)^T$. At the start of the nth timestep, the value of $\mathbf{c}$ is assumed to be known (along with the value of all other solution variables) and is denoted by $\mathbf{c}^n$. At the $(n+1)$th timestep the value is denoted by $\mathbf{c}^{n+1}$. Picard iteration uses the best available data to produce a tentative value of $\mathbf{c}$ at the $(n+1)$th timestep and this is denoted by $\tilde{\mathbf{c}}^{n+1}$ and so at the start of the timestep the best available data is $\tilde{\mathbf{c}}^{n+1} = \mathbf{c}^n$. At the end of the last iteration this tentative value becomes final at which point $\mathbf{c}^{n+1} = \tilde{\mathbf{c}}^{n+1}$.

During the Picard iteration, there is a choice of values to use for the solution of a variable that depends on other solution variables. The velocity $\mathbf{u}$ is needed to solve the advection-diffusion equation for $\mathbf{c}$, and so the available values to use for $\mathbf{u}$ are $\mathbf{u}^n$ and $\tilde{\mathbf{u}}^{n+1}$. The nonlinear relaxation parameter $\theta_{nl} \in [0, 1]$ allows the use of a linear combination of these two values given by:

$$\boldsymbol{u}^{n+\theta_{\mathrm{nl}}} = \theta_{\mathrm{nl}} \tilde{\boldsymbol{u}}^{n+1} + (1 - \theta_{\mathrm{nl}}) \boldsymbol{u}^n. \tag{4.15}$$

During the the first nonlinear iteration $\tilde{\boldsymbol{u}}^{n+1} = \boldsymbol{u}^n$.

The sequence of steps in the Picard iteration loop are outlined in figure 4.1.

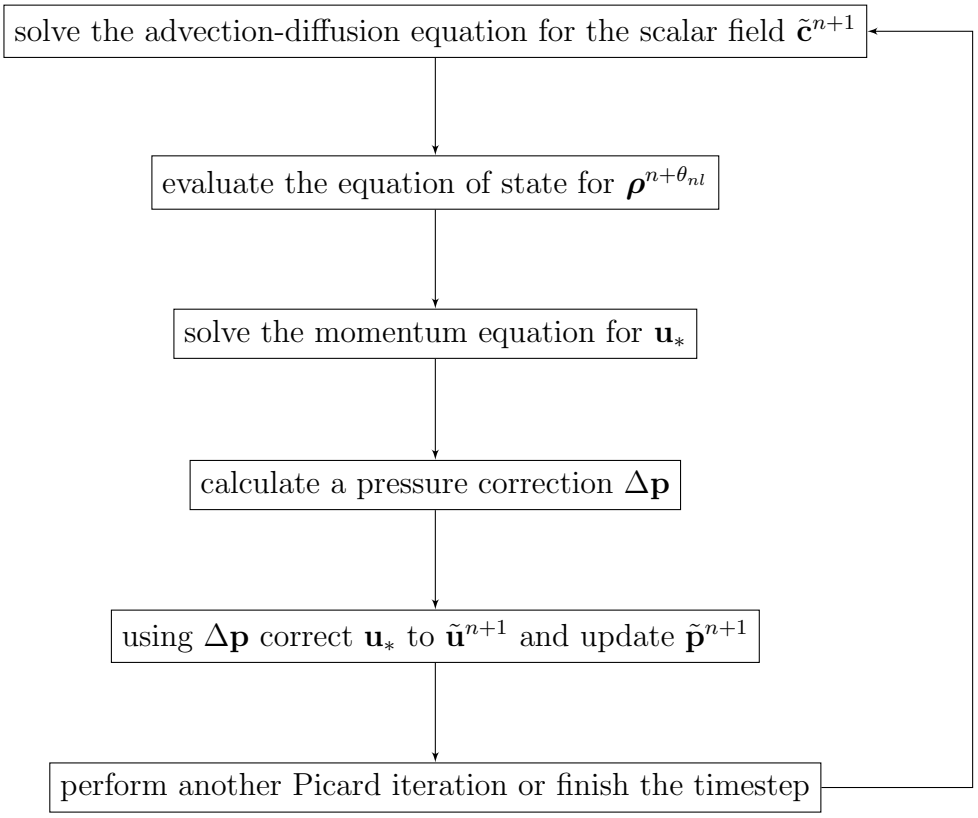


Figure 4.1: The principal steps in the nonlinear Picard iteration algorithm.

4.9 Mesh adaptivity

Adaptive mesh techniques require a measure by which to guide whereabouts in the computational domain the mesh needs to be refined or coarsened, depending on the complexity of the solution or to capture particular features of interest. These measures are often based on the gradient of the solution of a particular field, or some other physics based quantity such as vorticity. Optimisation algorithms are then used to perform local operations on the mesh to control the error measure.

4.9.1 Error measures

One of the error measures used to guide adaptive meshes is an estimate of the interpolation error. The interpolation error for element e in the mesh is such that

$$\epsilon_e \equiv ||u - \Pi_h u||_{\infty,e} \leq \tilde{\gamma} \max_{\boldsymbol{x}\in e} \max_{\boldsymbol{v}|\boldsymbol{x}+\boldsymbol{v}\in e} \{\boldsymbol{v}^T |H(\boldsymbol{x})| \boldsymbol{v}\} \tag{4.16}$$

where $\Pi_h u$ if the piecewise linear Lagrange interpolant of u, $||\cdot||_{\infty,e}$ is the max-norm on element e, $\tilde{\gamma}$ is an order 1 constant independent of the mesh, and $H \equiv \nabla^T \nabla u$ is the Hessian. $\boldsymbol{v}^T H(\boldsymbol{x}) \boldsymbol{v}$ is the curvature of the field in the direction of $\boldsymbol{v}$, and this directional information can be used to make anisotropic meshes.

By diagonalising the Hessian as $H = Q\Lambda Q^T$, with Q a matrix of orthonormal eigenvectors and Λ a diagonal matrix of eigenvalues, it can be interpreted as a combination of a rotation and a rescaling. An adapted mesh can then be constructed which distributes the error throughout the domain. This is equivalent to constructing a uniform mesh of equilateral tetrahedra (or triangles) in a metric space with the metric $M = |H|/\epsilon$ where ϵ is a user defined desired error which can be spatially dependent (George, 1998). The transformation $\boldsymbol{v} = Q\sqrt{|\Lambda|}^{-1}\tilde{\boldsymbol{v}}$ can be used to transform a uniform isotropic element to the adapted anisotropic element in the physical domain achieving the desired interpolation error throughout the domain, figure 4.2. Maximum and minimum edge lengths can be imposed by limiting the minimum and maximum eigenvalues with

$$\tilde{\lambda}_j = \min\left\{\frac{1}{h_{\min}^2}, \max\left\{\frac{|\lambda_j|}{\epsilon}, \frac{1}{h_{\max}^2}\right\}\right\}, \quad j = 1, 2, 3,$$

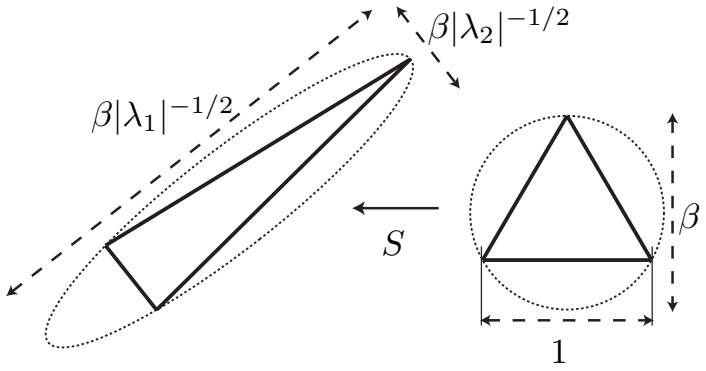


Figure 4.2: An element of unit size in metric space is transformed to an anisotropic element in physical space with the transformation $S = Q\sqrt{|\Lambda|}^{-1}$.

since the eigenvalues λ_i of the Hessian are proportional to the inverse of the square of the desired edge lengths. Several fields can be adapted to, in which case a metric is constructed for each field with its own interpolation errors and these are superimposed.

4.9.2 Mesh optimisation methods

Now that a field of desired edge lengths has been constructed, the overall quality of the mesh can be improved with local mesh optimisation algorithms, where each element is visited in turn and its size and shape is optimised. In a metric space with edge lengths measured with a weighted norm $||\boldsymbol{v}||_M = (\boldsymbol{v}^T M \boldsymbol{v})^{1/2}$, the goal is a mesh of unit sized equilateral tetrahedra (or triangles). Edge lengths and in-sphere radius can be used to measure mesh quality and these are incorporated into the functional given by:

$$F_e = \frac{1}{2}\sum_{l\in\mathcal{L}_e}(r_l - 1)^2 + \left(\frac{\alpha}{\rho_e} - 1\right)^2, \tag{4.17}$$

where $\mathcal{L}_e$ is the set of edges of element e, r_l is the length of edge l, ρ_e is the radius of the element's inscribed sphere, and $\alpha = \sqrt{6}/12$ (or $1/2\sqrt{3}$ in 2D) is the radius of the inscribed sphere for a unit equilateral tetrahedron. The objective of the mesh optimisation algorithm is to minimise the functional F_e. A sequence of local topological and geometrical operations (Freitag and Ollivier-Gooch, 1997; Pain et al., 2001) are performed on the mesh by visiting each element in turn in a Gauss-Seidel iterative manner and the local mesh structure is changed with the operations shown in figure 4.3.

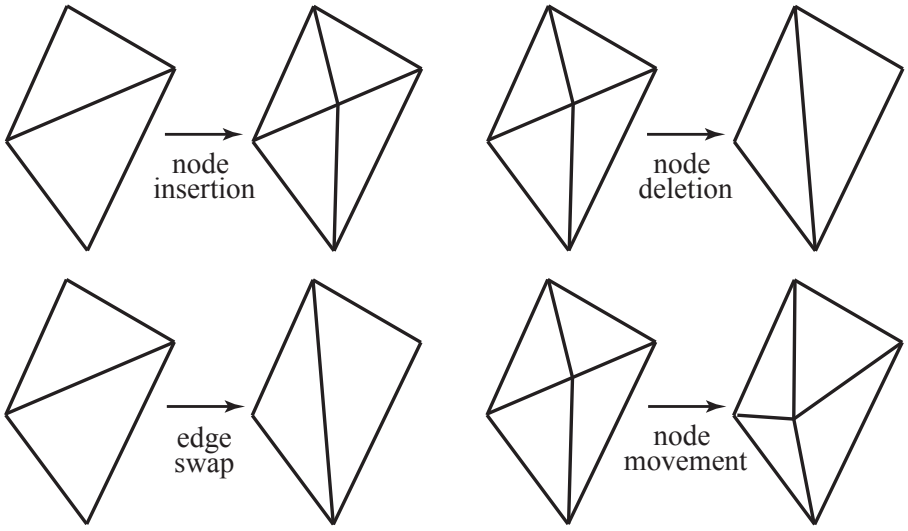


Figure 4.3: Element operations used to locally optimise the mesh in two dimensions. Top-left: node insertion or edge split. Top-right: node deletion or edge collapse. Bottom-left: edge swap. Bottom-right: node movement.

Chapter 5

Methodology

Contents

5.1 Overview 78

5.2 Propagation of internal waves in a linearly stratified fluid . . 78

5.2.1 Setup 78

5.3 Breaking of internal waves in a linear stratification 81

5.3.1 Coastal scale simulations 81

5.3.2 Laboratory scale simulations 85

5.4 Generation of internal waves in a two–layer 87

5.4.1 Internal lee wave generation in a two–layer fluid 87

5.4.2 Tilting tank 89

5.5 Shoaling and breaking of internal waves in a two–layer fluid 91

5.1 Overview

This chapter describes the numerical simulations that have been carried out. The details of the physical setup, including the domain, initial and boundary conditions are described for each set of simulations. Also, physical parameters such as diffusivity or forcing amplitude, and numerical parameters such as the time-step, mesh size, and whether the mesh is being adapted with time are also described.

The diagnostics used to assess the simulations, such as the evolution of kinetic energy with time, and convergence to known analytical solutions are also outlined in this chapter.

5.2 Propagation of internal waves in a linearly stratified fluid

The simple case of internal wave propagation has an analytical solution which lends itself to being used as a test case for model convergence. Also, numerical viscous effects can be estimated, and examined as a function of mesh spacing.

5.2.1 Setup

The linearised equations describing the dynamics of an inviscid linearly–stratified fluid in a rectangular domain admit the two–dimensional rightward–propagating trapped–wave solution:

$$u(x,z,t) = -U_0 \sin(kx - \omega t)\cos mz, \tag{5.1}$$

$$w(x,z,t) = U_0 \frac{k}{m}\cos(kx - \omega t)\sin mz, \tag{5.2}$$

$$\rho'(x,z,t) = U_0 \frac{\rho_0 N^2}{g\omega}\frac{k}{m}\sin(kx - \omega t)\sin mz, \tag{5.3}$$

where u and w are the horizontal and vertical components of velocity respectively, ρ' is the density perturbation, U_0 is the maximum value of u, k and m are the horizontal and vertical wavenumbers respectively, N is the buoyancy frequency, ω is the frequency of the wave given by the dispersion relation:

$$\omega^2 = \frac{N^2 k^2}{k^2 + m^2}, \tag{5.4}$$

and g is the gravity magnitude.

5.2.1.1 Domain and initial and boundary conditions

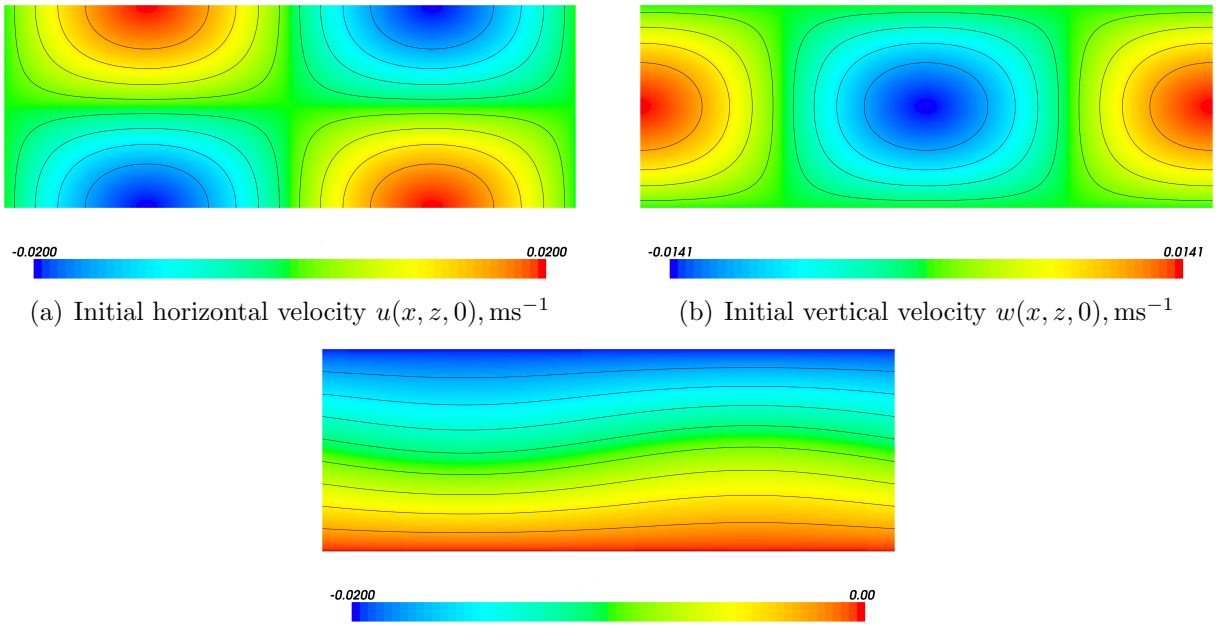
We now consider a horizontally periodic domain which is one horizontal wavelength ($2\pi/k$) long and half a vertical wavelength (π/m) deep, and use the initial conditions:

$$u(x,z,0) = -U_0 \sin kx \cos mz, \tag{5.5}$$

$$w(x,z,0) = U_0 \frac{k}{m} \cos kx \sin mz, \tag{5.6}$$

$$\rho'(x,z,0) = U_0 \frac{\rho_0 N^2}{g\omega} \frac{k}{m} \sin kx \sin mz, \tag{5.7}$$

to set up a rightwards–propagating mode–1 internal wave.



(a) Initial horizontal velocity $u(x,z,0), \mathrm{ms}^{-1}$

(b) Initial vertical velocity $w(x,z,0), \mathrm{ms}^{-1}$

(c) Initial density $\frac{\rho}{\rho_0} - 1$

Figure 5.1: Initial conditions describing a rightwards propagating mode–1 internal wave in a periodic domain, used in the wave propagation test case.

The internal wave maintains its form and propagates rightwards out of the domain, which due to its periodic nature re-enters the domain at the left hand side.

5.2.1.2 Diagnostics

Under the Boussinesq approximation, kinetic energy is proportional to the square of the L^2 norm of velocity magnitude. To test our numerical results we thus examine the L^2 norm of velocity magnitude with time and compare this with the constant analytical value evaluated over the domain:

$$\sqrt{\int_0^{\frac{\pi}{m}} \int_0^{\frac{2\pi}{k}} (u^2 + w^2)\, dxdz} = \frac{U_0 \pi}{\sqrt{2mk}} \left(1 + \frac{k^2}{m^2}\right)^{\frac{1}{2}}. \tag{5.8}$$

Simulation	Δx,Δz, m	Vertices	Elements	Δt, s
WavePropagateA	0.02	2666	5334	0.1884
WavePropagateB	0.01	10431	20864	0.0942
WavePropagateC	0.005	41261	82524	0.0471
WavePropagateD	0.0025	164121	328244	0.0236

Table 5.1: Table of mesh and time step parameters used in the wave propagation simulations.

The L^2 norm of velocity magnitude, as calculated in equation 5.8, is constant when evaluated over an integer number of horizontal wavelengths. Since the domain is one wavelength long the L^2 norm of velocity should remain constant.

A series of simulations with increasing mesh resolutions are run, with time steps chosen so that the wave Courant number remains fixed. We compare the L^2 norm of velocity magnitude after 5 wave periods with the analytical result to measure the convergence of the model.

These first simulations were run with an explicit viscosity of zero. The simulations are rerun with explicit viscosity magnitudes of $10^{-8}, 10^{-7}$ and $10^{-6}\,\mathrm{m^2 s^{-1}}$, and the rate at which the L^2 norm of velocity magnitude decays with time, α, is calculated by fitting a function $-\alpha t + \beta \cos \omega t + \gamma$ to the numerical value of the L^2 norm of velocity magnitude for each viscosity and mesh resolution.

5.3 Breaking of internal waves in a linear stratification

5.3.1 Coastal scale simulations

Numerical simulations of internal wave breaking at idealised continental margins at coastal scales are conducted with Fluidity–ICOM in order to compare directly with the results produced by Legg and Adcroft (2003) who used the state-of-the-art Massachusetts Institute of Technology General Circulation Model (MITgcm). MITgcm is a non-hydrostatic model which uses a finite volume formulation on a fixed but not necessarily uniform grid, with a z-level mesh that can employ shaved or partial cells to accurately conform to complex bathymetry.

Firstly, simulations are conducted to test the effects of mesh resolution and adaptivity on the results. Then the effects of changing horizontal and vertical viscosities are considered. The influence of rotation on the wave propagation and breaking are discussed and the results are directly compared with those of Legg and Adcroft (2003). Finally, simulations with differently shaped continental margins — planar (critical, subcritical and supercritical slopes), concave, convex and generic — are performed, and the breaking processes are discussed.

5.3.1.1 Domain

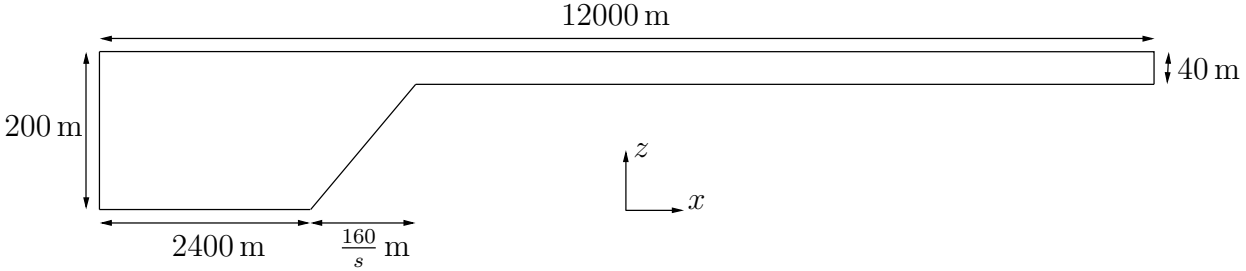


Figure 5.2: Domain used in the wave breaking simulations with planar slopes.

The domain is 12 000 m in length, $x \in [0, 12000]$ and $z \in [0, 200]$, with bathymetry defined by

$$z_{\text{planar}} = \begin{cases} 0 & \text{for} \quad 0 < x \leq 2400, \\ s(x - 2400) & \text{for} \quad 2400 < x \leq \frac{160}{s} + 2400, \\ 160 & \text{for} \quad \frac{160}{s} + 2400 < x \leq 12000, \end{cases} \tag{5.9}$$

for the simulations with planar slopes (figure 5.2). The simulations with concave, convex and generic, or more specifically, hyperbolic tangent (referred to hereafter as "tanh") bathymetries have domains defined by

$$z_{\text{concave}} = \begin{cases} 0 & \text{for} \quad 0 < x \leq 2400, \\ 160\left(1 - \sqrt{\frac{3600-x}{1200}}\right) & \text{for} \quad 2400 < x \leq 3600, \\ 160 & \text{for} \quad 3600 < x \leq 12000, \end{cases} \tag{5.10}$$

$$z_{\text{convex}} = \begin{cases} 0 & \text{for} \quad 0 < x \leq 2400, \\ 160\sqrt{\frac{x-2400}{1200}} & \text{for} \quad 2400 < x \leq 3600, \\ 160 & \text{for} \quad 3600 < x \leq 12000, \end{cases} \tag{5.11}$$

$$z_{\text{tanh}} = 80\left(1 + \tanh\left[\frac{x - 3000}{600}\right]\right) \quad \text{for} \quad 0 < x \leq 12000. \tag{5.12}$$

The majority of the simulations are carried out in a two-dimensional vertical slice domain, (x, z), (the exception being the simulation incorporating the effects of Coriolis) with the velocity field denoted by $\mathbf{u} = (u, w)$.

5.3.1.2 Initial and boundary conditions

Initial conditions consist of no flow and a stable horizontal uniform stratification

$$u(\mathbf{x}, 0) = 0, \qquad w = (\mathbf{x}, 0) = 0, \qquad \tilde{\rho}(\mathbf{x}, 0) = \frac{\rho_0 N^2 z}{g}. \tag{5.13}$$

The boundary conditions imposed are a no-normal flow boundary condition on the upper boundary, $w(z = 200) = 0$, also known as a rigid lid boundary condition, and a no–slip velocity boundary condition on the bottom boundary, $u = w = 0$.

The problem is forced by generating an off-shore internal wave at the $x = 0$ boundary of the domain. A baroclinic wave is generated there, which propagates into the domain the x-direction, before it interacts with the continental margin.

The boundary conditions that generate the offshore internal wave are

$$u(0,z,t) = U_0 \cos mz \sin \omega t \tag{5.14}$$

$$w(0,z,t) = U_0 \omega (N^2 - \omega^2)^{-\frac{1}{2}} \sin mz \cos \omega t \tag{5.15}$$

$$\rho'(0,z,t) = \frac{U_0 \rho_0 N^2}{g} (N^2 - \omega^2)^{-\frac{1}{2}} \sin mz \sin \omega t \tag{5.16}$$

where $g = 10\,\mathrm{m\,s^{-2}}$, $m = \dfrac{\pi}{d}$, $d = 200\,\mathrm{m}$, $\omega = 1.41 \times 10^{-4}\,\mathrm{rad\,s^{-1}}$, $N = 1.07 \times 10^{-3}\,\mathrm{rad\,s^{-1}}$ and $U_0 = 0.024\,\mathrm{m\,s^{-1}}$. The period of the waves is $T = \dfrac{2\pi}{\omega} = 44561.6\,\mathrm{s}$.

These boundary conditions are derived in 2.3.4 and differ slightly to those in Legg and Adcroft (2003) in the coefficients used, primarily due the fact that we do not include Coriolis effects, but also because the boundary conditions in Legg and Adcroft (2003) seem to be inconsistent in that while the boundary condition for perturbation density is dimensionally correct, it is proportional only to N, when in fact it should be proportional to N^2. The boundary condition at $x = 12000$ is $w = 0$ and $\tilde{\rho}(12000, z, t) = \tilde{\rho}(12000, z, 0) = \dfrac{\rho_0 N^2 z}{g}$, so that fluid can flow in and out of the domain, but the no vertical flow and fixed density conditions ensure that no waves are generated there.

5.3.1.3 Parameters

Fluidity–ICOM solves the advection–diffusion equation for temperature rather than for (perturbation) density, so a linear equation of state is used, with a thermal expansion coefficient of $2.0 \times 10^{-4}\,\mathrm{K^{-1}}$. Temperature diffusivity is set to $\kappa = 0$, but the implicit numerical diffusivity inherent in the stable advection method used for temperature is non–zero (similarly to the previous section). A Galerkin discretisation is used for momentum, and a high–resolution control volume method for temperature (Wilson, 2009) and the temporal discretisation is Crank–Nicolson. The resulting linear systems are solved iteratively to a relative tolerance of 10^{-7}.

MITgcm 'use sufficiently high resolution to explicitly resolve the mixing processes due to Kelvin–Helmholtz instability and do not employ a sophisticated subgrid-scale mixing scheme: constant eddy viscosities are used instead, with values of $\nu_h = 10^{-2}\,\mathrm{m^2\,s^{-1}}$ and $\nu_z = 10^{-3}\,\mathrm{m^2\,s^{-1}}$' (Legg and Adcroft (2003)).

5.3.1.4 Adaptivity parameters

The adaptive mesh algorithm can be tuned to adapt to the curvature of density and the horizontal and vertical velocity fields. For both the density and velocity fields, the relative interpolation errors are set to 50% at the ends of the domain $x = 0$ and $x = 12000$ and to 10% in the location of the slope, $x \in [2400, 3600]$, with a linear gradation between the slope and the ends of the domain. The minimum horizontal and vertical element edge lengths that the adaptive mesh algorithm is allowed to set are $(\Delta x, \Delta z) = (5.0, 0.5)$ m in the region $x \in [2400, 3600]$, and scaled linearly up to (100.0,10.0) m at the ends of the domain. The maximum element edge lengths allowed are set to (200.0, 10.0) m everywhere, which is the coarsest resolution that can still accurately represent the propagation of the internal wave.

5.3.1.5 Diagnostics

One diagnostic that can be used to examine the effectiveness of mesh adaptivity is to look at the total kinetic energy of the fluid in each of the fixed mesh simulations and compare the adaptive mesh result to these. The total kinetic energy (in the Boussinesq sense) in the system is

$$KE = \int_{\Omega} \frac{1}{2} \rho_0 |\mathbf{u}|^2 d\Omega, \tag{5.17}$$

where Ω is the domain. We use the square of the L^2 norm of velocity magnitude as a metric to compare the adaptive mesh result to the fixed mesh results:

$$\int_{\Omega} |\mathbf{u}|^2 d\Omega, \tag{5.18}$$

A more relevant metric to evaluate the adaptive mesh result is to calculate the kinetic energy of the system in the region of interest *i.e.* at the slope:

$$\int_{z=0}^{z=200} \int_{x=2400}^{x=3600} |\mathbf{u}|^2 dx dz, \tag{5.19}$$

fot the planar simulation with a critical slope.

5.3.2 Laboratory scale simulations

A numerical simulation on a laboratory scale is carried out with Fluidity–ICOM to compare directly with the results produced by Venayagamoorthy and Fringer (2007) with the Stanford unstructured non–hydrostatic terrain–following adaptive Navier–Stokes simulator (SUNTANS).

5.3.2.1 Domain

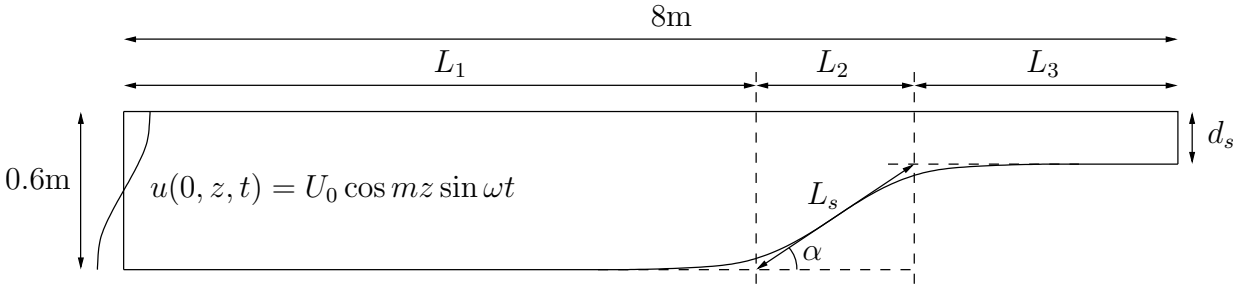


Figure 5.3: Domain for the SUNTANS wave breaking comparison test.

The domain is 8 m in length, $x \in [0, 8]$, with bathymetry defined by

$$z = \tfrac{1}{2} L_s \sin\alpha \left(\tanh \tfrac{2}{L_s \cos\alpha} \left[x - (L_1 + \tfrac{1}{2} L_2) \right] + 1 \right), \tag{5.20}$$

which has a maximum gradient $\gamma = \tan\alpha$ at $x = (L_1 + \frac{1}{2} L_2)$, i.e., halfway up the slope.

5.3.2.2 Initial and boundary conditions

The initial density stratification is given by

$$\frac{\tilde{\rho}(z)}{\rho_0} = -\frac{\Delta\tilde{\rho}}{\rho_0} \left(\frac{z}{d} \right), \tag{5.21}$$

with $\frac{\Delta\tilde{\rho}}{\rho_0} = 0.02$ and the depth d is 0.6 m. Gravity is set to $10\,\mathrm{m\,s^{-2}}$. This results in the constant buoyancy frequency $N = \frac{1}{\sqrt{3}}\,\mathrm{rad\,s^{-1}}$. A first mode internal wave is generated at the boundary $x = 0$ with the boundary conditions

$$u(0,z,t) = U_0 \cos mz \sin \omega t \tag{5.22}$$

$$w(0,z,t) = U_0 \omega (N^2 - \omega^2)^{-\frac{1}{2}} \sin mz \cos \omega t \tag{5.23}$$

$$\rho'(0,z,t) = \frac{U_0 \rho_0 N^2}{g} (N^2 - \omega^2)^{-\frac{1}{2}} \sin mz \sin \omega t \tag{5.24}$$

where $U_0 = 0.07\,\mathrm{m\,s^{-1}}$ is the amplitude of the forcing, m is the vertical wavenumber corresponding to the first baroclinic mode, $m = \frac{\pi}{d}$, and $\omega = \frac{1}{3}\,\mathrm{rad\,s^{-1}}$ is the forcing frequency. The period of the oscillations is $T = \frac{2\pi}{\omega}$ =18.85 s. By the dispersion relation, the slope of the group velocity is

$$s = \tan\theta = \frac{k}{m} = \left(\frac{\omega^2}{N^2 - \omega^2} \right)^{\frac{1}{2}} = \frac{1}{\sqrt{2}}. \tag{5.25}$$

For a critical slope, we choose L_2 and L_s such that $\tan\alpha = \frac{1}{\sqrt{2}}$. There is no normal flow on the upper boundary, $w(z = 0) = 0$, and a no–slip velocity boundary condition on the bottom boundary.

5.3.2.3 Parameters

A linear equation of state is used, with thermal expansion coefficient $2.0 \times 10^{-4}\,\mathrm{K^{-1}}$. Kinematic viscosity is set to $\nu = 10^{-6}\,\mathrm{m^2\,s^{-1}}$ and temperature diffusivity is set to $\kappa = 10^{-6}\,\mathrm{m^2\,s^{-1}}$. A Galerkin scheme is used for momentum and the high–resolution control volume method for temperature. Temporal discretisation is Crank–Nicolson, with a time step of 0.1885 s. The resulting linear systems were solved iteratively to a tolerance of 10^{-10}.

5.3.2.4 Diagnostics

The results are compared qualitatively with those from Venayagamoorthy and Fringer (2007). Also, the effect of increasing the wave amplitude on the wave breaking is briefly examined.

5.4 Generation of internal waves in a two–layer

The generation of internal waves in a two–layer fluid is examined in this section. Two generation mechanisms are considered: the internal lee wave generation as a result of stratified flow over topography; and the degeneration of large–scale interfacial waves into a train of solitary waves.

5.4.1 Internal lee wave generation in a two–layer fluid

Stratified flow over bottom topography is one of the main generation mechanisms for internal waves. In this section, we simulate the flow of a two-layer fluid over a topographic bump and compare the internal lee wave that is generated with an analytical solution and a laboratory simulation (Kranenburg and Pietrzak, 1989), and the results of numerical simulations with FINEL3D Labeur and Pietrzak (2004).

5.4.1.1 Setup

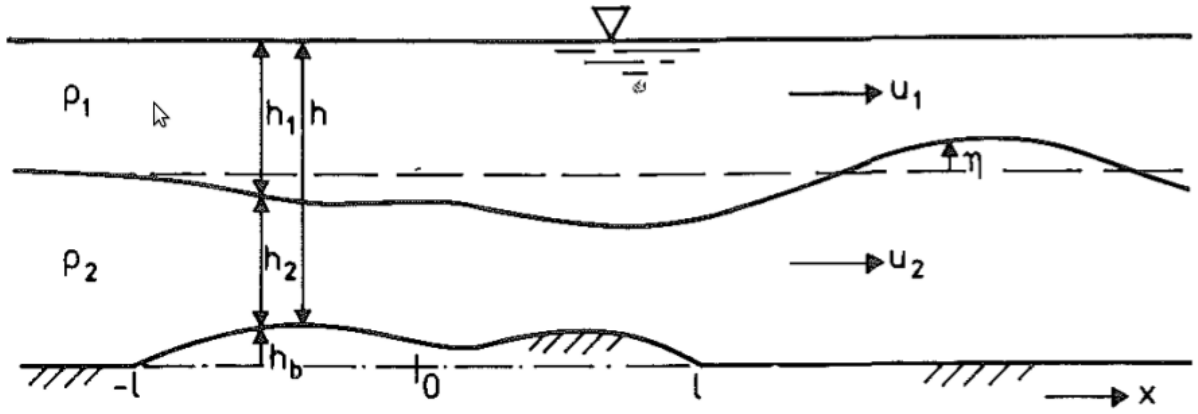


Figure 5.4: Definition sketch of the problem taken from Kranenburg and Pietrzak (1989).

The domain is 6 m wide ($x \in [-1, 5]$) and 0.4 m deep with a bump on the bottom of the domain at the origin. There is a constant discharge q in each layer of the system so that $u_1 h_1 = u_2 h_2 = q$. The boundary conditions are free slip on the top and bottom boundaries, and no normal flow. The initial condition for the density perturbation is

$$\rho'(x, z, t = 0) = -\frac{1}{2}\frac{\Delta\rho}{\rho_0} \tanh\left[\frac{z - h_2}{\epsilon}\right], \tag{5.26}$$

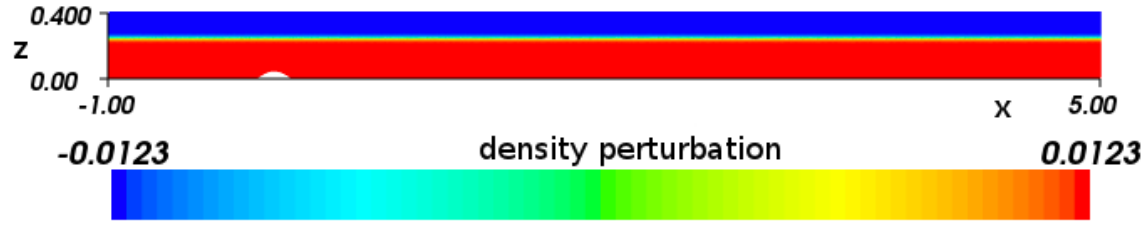


Figure 5.5: Initial condition used in the numerical simulations for the perturbation density. Note the topographic bump at $x = 0\,\mathrm{m}$.

where ϵ is the thickness of the interface. The fluid is initially stationary with the velocity set to zero throughout the domain. The boundary condition for horizontal velocity is imposed at the left hand side of the domain and is given by

$$u(x = -1, z, t) = \left(u_2 + \frac{1}{2}(u_1 - u_2)\left(\tanh\left[\frac{z - h_2}{\epsilon}\right] + 1\right)\right) r(t), \tag{5.27}$$

where q is the discharge in each layer, $u_1 = q/h_1$ is the velocity in the upper layer and $u_2 = q/h_2$ is the velocity in the lower layer, and $r(t)$ is a function of time that begins at zero and ramps up to a value of 1.0 over a period of t_0:

$$r(t) = \begin{cases} 3\left(\frac{t}{t_0}\right)^2 - 2\left(\frac{t}{t_0}\right)^3 & \text{for} \quad t < t_0, \\ 1.0 & \text{for} \quad t \geq t_0. \end{cases} \tag{5.28}$$

The boundary condition for perturbation density is imposed at the left hand side of the domain ($x = -1.0\,\mathrm{m}$) is the same as the initial condition for perturbation density. To prevent waves being reflected at the right hand boundary, a 1 m long sponge region for perturbation density is used in the numerical simulation. This appears in the advection–diffusion equation as a source term and an absorption term, so that the solution is relaxed to the ambient stratification to damp the lee wave.

5.4.1.2 Diagnostics

The analytical solution for inviscid subcritical two-layer flow over a topographic bump is derived in (Kranenburg and Pietrzak, 1989). This shows that the downstream interface of the two-layer fluid η is:

$$\eta(x) = \frac{\pi}{b}\frac{F_2^2}{k^2}\frac{\frac{kl}{h}\cos\frac{kl}{h}}{\left(k\frac{l}{h}\right)^2 - \frac{\pi^2}{4}}\hat{h}_b \sin\frac{kx}{h}, \tag{5.29}$$

where

$$k = \left(\frac{1-F^2}{b}\right)^{\frac{1}{2}}, \tag{5.30}$$

is a dimensionless wavenumber, and

$$b = \frac{u_1^2 h_1 + u_2^2 h_2}{3g'h^2}, \tag{5.31}$$

$$F_2^2 = \frac{u_2^2}{g'h_2}, \quad F^2 = \frac{u_1^2}{g'h_1} + F_2^2, \tag{5.32}$$

are internal Froude numbers, g' is the reduced gravity, l is the half-width of the topography, h is the total domain height and $\hat{h}_b$ is the height of the topography, which is defined by:

$$h_b = \hat{h}_b \cos\frac{\pi x}{2l} \quad \text{for} - l \leq x \leq l. \tag{5.33}$$

5.4.2 Tilting tank

Horn et al. (2001) performed laboratory simulations of the evolution of an initially sloped thermocline in a two–layer fluid to investigate the degeneration of large–scale interfacial waves in a lake. We compare the experiments which resulted in the generation of solitons with numerical simulations carried out with Fluidity–ICOM, to test its efficacy in modelling internal solitary wave generation.

5.4.2.1 Setup

In the laboratory experiments the tank was tilted at the desired angle of the thermocline and filled with freshwater and saltwater, and once the appropriate stratification had been achieved, the tank was tilted (back to a flat position) to start the experiment. In the numerical simulations we initialise the two–layer fluid with a thermocline at an angle to the horizontal equivalent to the angle through which the tank was tilted, as shown in figure 5.6, rather than changing the direction of the gravity vector over a finite time at the start of the simulation. The initial density perturbation is described by

$$\rho'(x,z) = -\frac{1}{2}\frac{\Delta\rho}{\rho_0}\tanh\left[\frac{z-\zeta(x)}{\epsilon}\right], \tag{5.34}$$

where $\zeta(x) = x\tan\theta + h$ defines the sloping interface with θ the initial angle of tilt and h the height of thermocline above the bottom of the tank in the (horizontal) centre of the tank ($x = 0$). ϵ gives a measure of the interface thickness $\delta_\rho = 2\epsilon\tanh^{-1}(0.99)$, so that across the interface 99% of the density change occurs over a thickness δ_ρ (Fringer and Street (2003)).

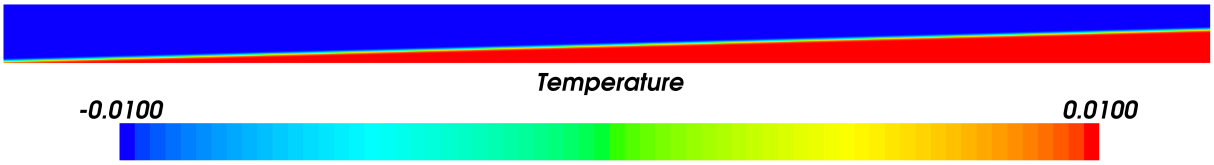


Figure 5.6: Initial condition in the tiliting tank test case.

The dimensions of the tank are 6 m by 0.29 m. No slip boundary conditions are imposed on all four boundaries. ϵ takes the value 0.00189 m which corresponds to a thermocline thickness of $\delta_\rho = 0.01$ m. Viscosity is set to $\nu = 1.0 \times 10^{-6}\,\mathrm{m^2\,s^{-1}}$ which is a typical value for freshwater (and saltwater) and the diffusivity of the stratifying agent (in this case salt) is set to $\kappa = 1.5 \times 10^{-9}\,\mathrm{m^2\,s^{-1}}$ which is a typical value for the diffusivity of salt in water (Batchelor, 1967, p. 595).

A quadratic drag term is included in the simulations to simulate the friction on the sidewalls of the tank (Bourgault and Kelley, 2007; Kundu, 1990). This appears in the right hand side of the momentum equation as a sink term:

$$\mathbf{F}_s = -C_D\frac{|\mathbf{u}|\mathbf{u}}{B} \tag{5.35}$$

where C_D is the drag coefficient and B is the width of the tank.

The drag coefficient is chosen so that the displacement of the first leftward–travelling soliton matches that in the laboratory experiment. Several fixed mesh simulations were performed with different drag coefficents to inform the choice of drag coefficient to be used in subsequent simulations. We found that the displacement of the first leftward–travelling soliton depended on the drag coefficient in an exponential fashion as shown in figure 5.7, which led to the choice of $C_D = 0.036$ for the drag coefficient.

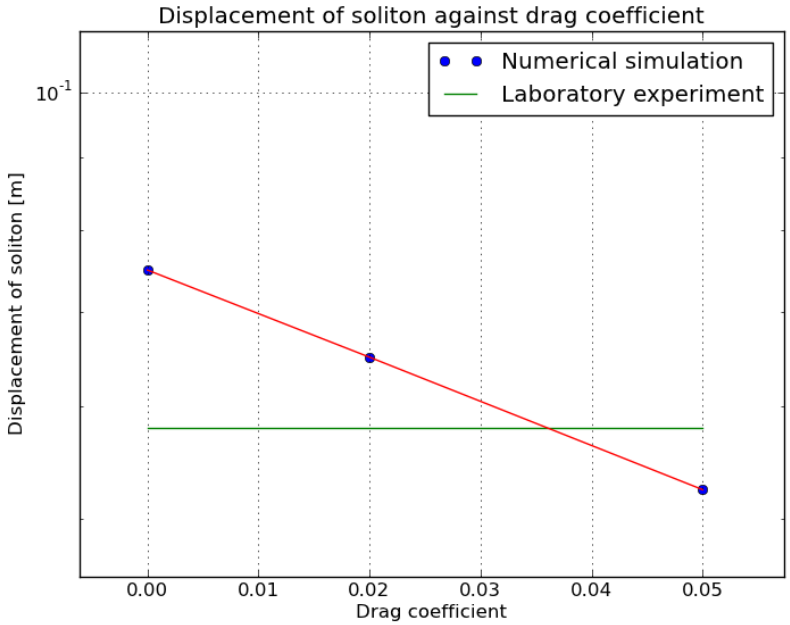


Figure 5.7: Displacement of the first leftward-travelling soliton against drag coefficient for the tilting tank test case. Based on this we choose a drag coefficient of $C_D = 0.036$ to best match the experimental data.

5.5 Shoaling and breaking of internal waves in a two–layer fluid

5.5.0.2 Setup

The initial condition for the perturbation density is a sech profile displacement with the same width but twice the amplitude to the wave that we wish to generate,

$$\rho'(x,z) = -\frac{1}{2}\frac{\Delta\rho}{\rho_0}\tanh\left[\frac{z-h_2+\zeta(x)}{\epsilon}\right], \tag{5.36}$$

where

$$\zeta(x) = 2a\,\mathrm{sech}^2\left[\frac{x-x_0}{2L_w}\right], \tag{5.37}$$

with x_0 the horizontal coordinate defining the location of the left-hand boundary of the domain. This is shown in the upper panel of figure 5.8. This evolves into a rightward propagating solitary wave, shown in the lower panel of figure 5.8. The fluid is initially stationary with the velocity equal to zero everywhere throughout the domain. The boundary conditions are no-normal flow for velocity everywhere on the boundary, along with no-slip on the bottom boundary and the slope.

Initial condition.

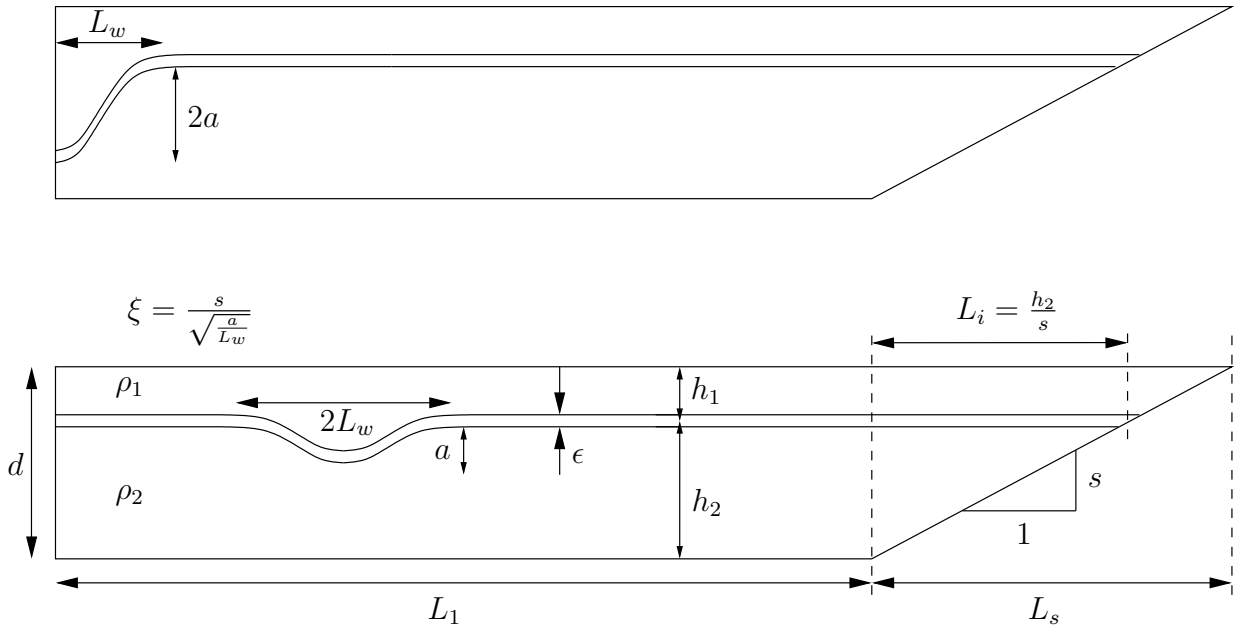
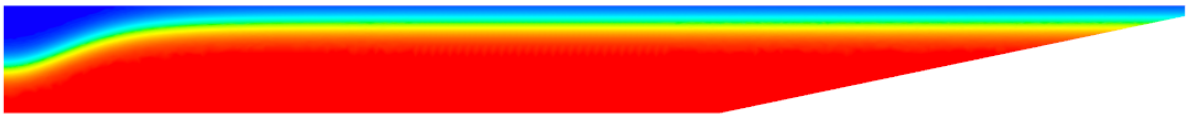
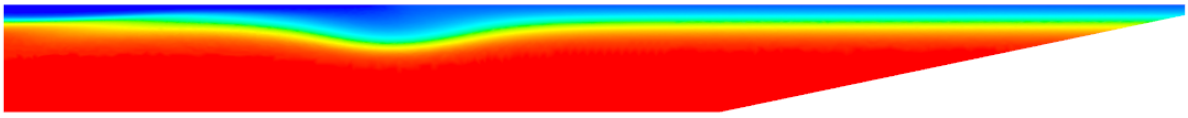


Figure 5.8: Domain used in the shoaling breaking wave simulations and the important parameters.

5.9 shows the initial condition for perturbation density, and the perturbation density and horizontal and vertical velocity fields after 10 s, showing how the initial condition has evolved into a rightward propagating solitary wave



(a) Initial condition for perturbation density



(b) Perturbation density after 10 s



(c) Horizontal velocity after 10 s



(d) Vertical velocity after 10 s

Figure 5.9: Initial condition for perturbation density and the perturbation density and velocities after 10 seconds of simulated time for the shoaling breaking wave simulation.

5.5.0.3 Reflectance of pseudoenergy

The Iribarren number is defined as

$$\xi = \frac{s}{|a/L_w|^{1/2}}, \tag{5.38}$$

where s is the slope, and a and L_w are the amplitude and the wavelength of the shoaling wave respectively. This dimensionless number, also known as a 'surf similarity parameter', was originally developed to classify surface waves breaking at the shore, but Boegman et al. (2005) found it also applied to internal solitary wave breaking at a slope.

The sum of the kinetic and available potential energies is the pseudoenergy. The energy reflectance is the ratio of reflected to incident pseudoenergy flux, and this is calculated for a series of simulations with wave amplitudes of 21, 26, 31, 36 and 41 mm, and slope lengths of 250, 450, 650, 900 and 1350 mm.

Chapter 6

Internal waves in a linearly stratified fluid

Contents

6.1 Propagation 98

6.1.1 Propagation of internal waves in a linearly stratified fluid 98

6.2 Breaking 102

6.2.1 Comparison with MITgcm — a coastal scale numerical simulation 102

6.2.2 Comparison with SUNTANS — a laboratory scale numerical simulation 122

6.3 Conclusions 127

This chapter considers internal waves in a linearly stratified fluid and their numerical solution. Propagation and breaking of internal waves are considered and through comparisons with analytical and other numerical models the methods considered in this thesis are validated and benchmarked.

The propagation of internal waves in a horizontally periodic domain is considered to demonstrate that the numerical model converges to an analytical result. It is important to show that the numerical model used in this study can accurately simulate internal waves and by using an appropriate error measure the model converges appropriately. At a series of mesh resolutions the L^2 norm of kinetic energy is considered and is demonstrated to converge to the theoretical value at second (quadratic) order. As expected some dissipation is observed and in order to quantify the magnitude of the implicit viscous effect in the model causing this an analysis of the simulation at a series of explicit viscosity values is considered. From this, estimates for the implicit numerical viscosity at different mesh resolutions are established and shown to be better than second order.

Also, the more complicated process of internal waves breaking at a slope, which does not have an analytical solution, is considered to compare Fluidity–ICOM with other established numerical models. The interaction of internal waves with topography and subsequent breaking is one of the primary mechanisms for intense diapycnal mixing in the ocean, and thus it is vitally important to ensure that one is able to represent this multi-scale process accurately in models. To investigate this, comparisons are made to the popular and well-trusted MITgcm (at coastal scale) (Legg and Adcroft, 2003) and SUNTANS (at laboratory scale) (Venayagamoorthy and Fringer, 2005, 2006, 2007) models. The effects of model resolution (including mesh adaptivity), viscosity and geometry are considered.

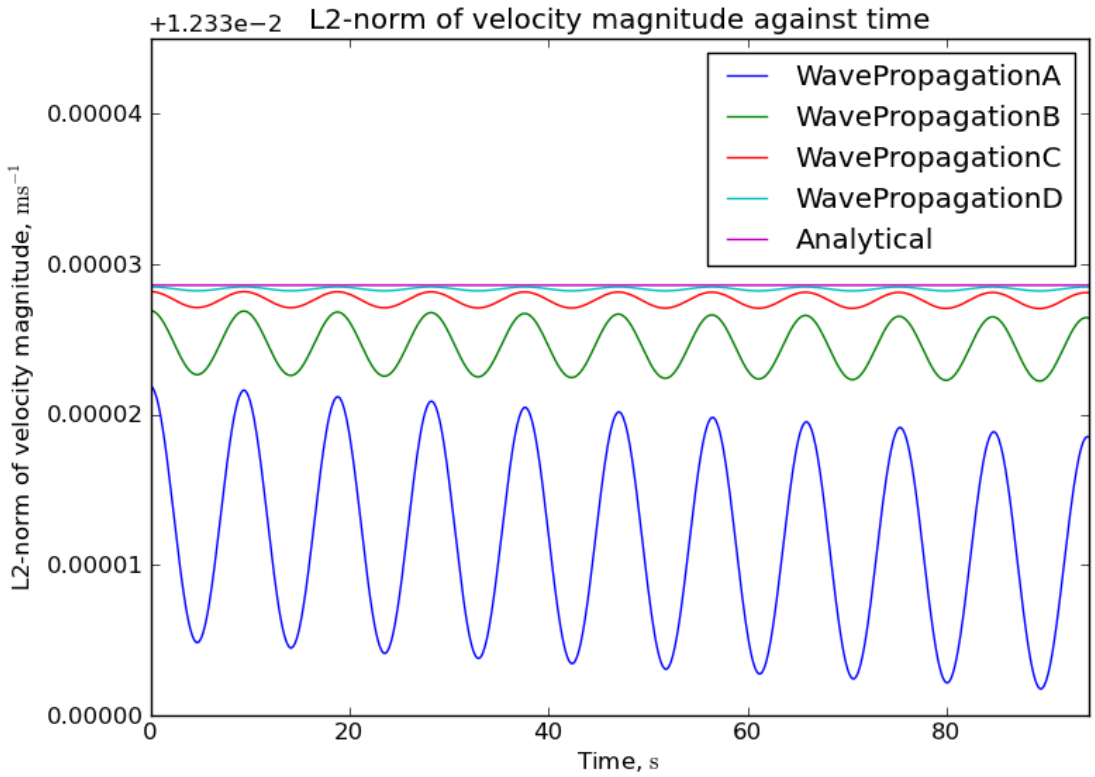


Figure 6.1: L^2 norm of velocity magnitude against time for increasing resolution over 5 wave periods for the simulations listed in table 5.1. The constant analytical solution is also plotted. The frequency of oscillation is 2ω as a result of the sine–squared function in the velocity magnitude (and as a result 10 oscillations are shown).

6.1 Propagation

6.1.1 Propagation of internal waves in a linearly stratified fluid

Figure 6.1 shows the L^2 norm of velocity magnitude against time for four simulations with increasing mesh resolution, the parameters for which are shown in table 5.1. Also plotted in figure 6.1 is the analytical value of the L^2 norm of velocity magnitude which remains constant with time.

The time–averaged value of the L^2 norm of velocity magnitude approaches the analytical solution with increasing mesh resolution as expected, and the variability of the L^2 norm of velocity magnitude (or amplitude of oscillation) decreases with increasing mesh resolution.

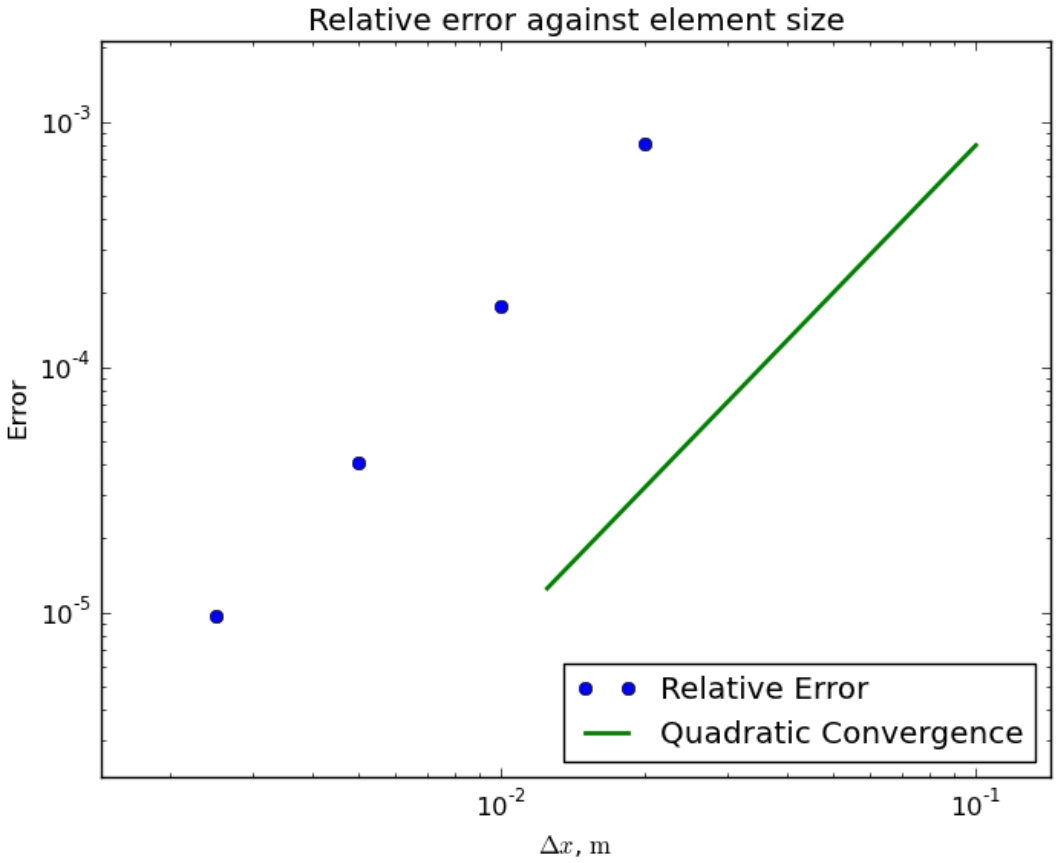


Figure 6.2: Relative error against element size showing quadratic convergence for the wave propagation test case.

The relative error of the solution of the L^2 norm of velocity magnitude after 5 periods is plotted against mesh size Δx in figure 6.2 for the four simulations, along with a straight

line representing quadratic convergence. Figure 6.2 clearly shows that the convergence rate is quadratic, as expected from a continuous Galerkin discretisation for the momentum equation.

In figure 6.1, the L^2 norm of velocity magnitude decays with time due to implicit numerical dissipation effects. The magnitude of this numerical viscosity in each simulation can be estimated by comparing this decay against the rate at which the L^2 norm of velocity magnitude decays with time when different values of explicit viscosity are applied within the simulations. The simulations listed in Table 5.1 were run with an explicit viscosity of zero and hence all dissipation effects must be numerical. Numerical viscosity has been inferred from the simulations with non–zero explicit viscosity. The decay rates are given in table 6.1.

Δx, Δz	$\nu = 0.0$	$\nu = 10^{-8}$	$\nu = 10^{-7}$	$\nu = 10^{-6}$
0.02	3.59×10^{-8}	3.85×10^{-8}	6.14×10^{-8}	2.91×10^{-7}
0.01	4.97×10^{-9}	7.53×10^{-9}	3.05×10^{-8}	2.60×10^{-7}
0.005	7.27×10^{-10}	—	—	2.56×10^{-7}
0.0025	1.18×10^{-10}	—	—	2.55×10^{-7}

Table 6.1: Decay rate α (ms^{-2}) for different explicit viscosities ($\mathrm{m}^2\mathrm{s}^{-1}$) and mesh spacing Δx, Δz (m).

Figure 6.3 shows that there is a linear dependence between the explicit viscosity value applied and the decay rate of the L^2 norm of velocity magnitude. This can give us an indication of the numerical viscosity ν_0 using the linear dependence $\alpha \propto (\nu + \nu_0)$. Table 6.2 lists the estimates of numerical viscosity, and these values are plotted in figure 6.4.

Δx, Δz	ν_0
0.02	1.41×10^{-7}
0.01	1.95×10^{-8}
0.005	2.85×10^{-9}
0.0025	4.63×10^{-10}

Table 6.2: Estimates of numerical viscosity ν_0 ($\mathrm{m}^2\mathrm{s}^{-1}$) for different mesh spacing Δx, Δz (m).

Figure 6.4 shows that numerical viscosity is proportional to $(\Delta x)^{2.75}$.

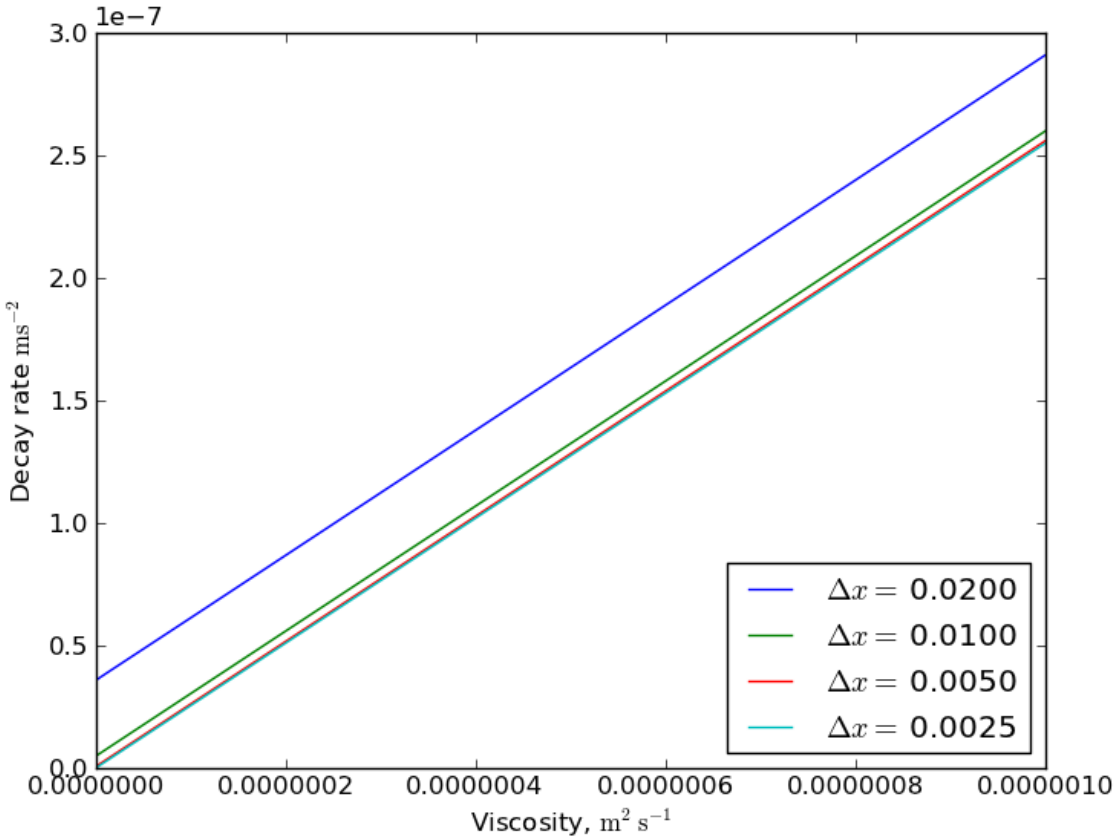


Figure 6.3: Decay rate of the L^2 norm of velocity magnitude against viscosity for different mesh spacing.

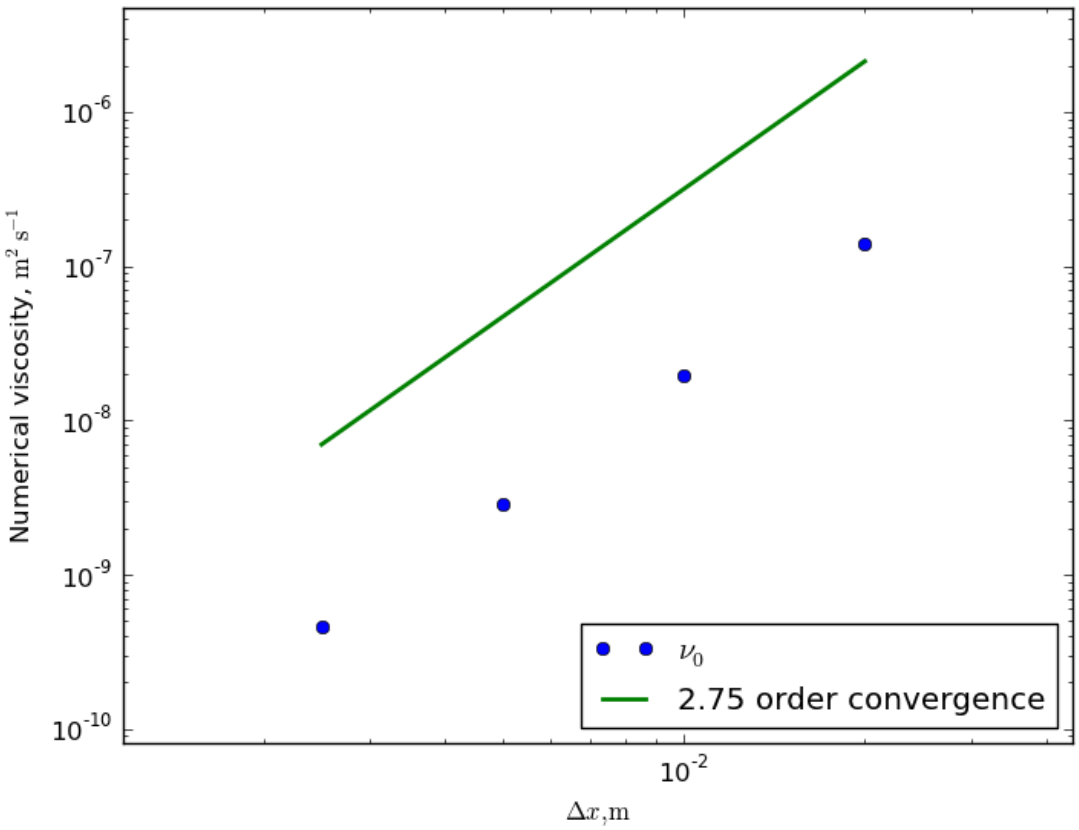


Figure 6.4: Numerical viscosity as a function of mesh spacing.

6.2 Breaking

This section examines the breaking of first baroclinic mode internal waves in a linearly stratified fluid. The interaction of internal waves with topography and subsequent breaking is one of the primary mechanisms for intense diapycnal mixing in the ocean. Thus it is critical that the ability of the model to accurately represent this phenomena is thoroughly assessed.

6.2.1 Comparison with MITgcm — a coastal scale numerical simulation

Numerical simulations of internal wave breaking at idealised continental margins at coastal scales are conducted with Fluidity–ICOM in order to compare directly with the results produced by Legg and Adcroft (2003) who used the state-of-the-art Massachusetts Institute of Technology General Circulation Model (MITgcm).

6.2.1.1 The effect of resolution and adaptivity

Several fixed mesh simulations with increasing resolution are performed to validate the adaptive mesh results. Horizontal velocities and perturbation density are compared for different simulations to examine qualitative convergence, and as a more quantitative diagnostic the evolution of the kinetic energy for the different simulations are investigated.

For these simulations viscosity is set to $\nu_x = 10^{-2}\,\mathrm{m}^2\,\mathrm{s}^{-1}$ in the horizontal direction, and to $\nu_z = 10^{-3}\,\mathrm{m}^2\,\mathrm{s}^{-1}$ in the vertical direction, as is used in Legg and Adcroft (2003), and the planar domain with critical slope $s = \frac{2}{15}$ is considered. A time step Δt is chosen such that the maximum Courant number is always less than 5, that is $\Delta t \left(\frac{|u|}{\Delta x} + \frac{|w|}{\Delta z} \right) < 5.0$ by examining typical velocities in any given simulation and choosing the appropriate time step. It is possible to use adaptive timestepping, but in these particular simulations it has not been used.

Figure 6.5 shows u-velocity and perturbation density at $t = 3.0\,T$, where T is the period of the waves, for various fixed mesh resolutions and adaptive mesh simulations. It is clear that the coarsest mesh simulations, ResolutionA and ResolutionB, are very under-resolved, with the magnitude of the maximum and minimum horizontal velocities greater than those for the finest fixed mesh simulation, ResolutionD. Qualitatively, the results are

Simulation	Δx, m	Δz, m	Vertices	Elements	Δt, s
ResolutionA/LeggP	100.0	10.0	1148	2294	557.020
ResolutionB/LeggQ	50.0	5.0	4420	8838	278.510
ResolutionC/LeggR	20.0	2.0	29103	58204	111.404
ResolutionD/LeggS	10.0	1.0	120749	241496	55.702
Adaptive	—	—	—	—	55.702

Table 6.3: Table of parameters used in the wave breaking simulations comparing to MIT-gcm.

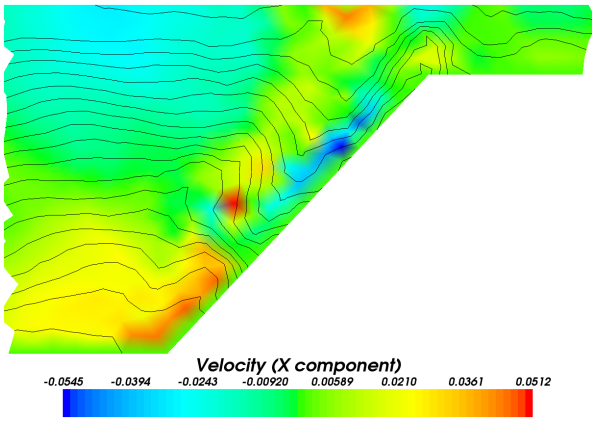
similar in the existence of a density front, with corresponding upslope flow behind and downslope flow ahead of it, approximately one third of the way up the slope, with this density front better resolved with increasing resolution. ResolutionC and ResolutionD are fairly comparable, the main difference being the appearance of a series of density fronts in the finer resolution. Also, ResolutionC exhibits a larger magnitude of the downslope flow than in ResolutionD, which is due to the viscous boundary layer being more well-resolved in ResolutionD as a result of the finer resolution. The "correct" solution to this problem is now assumed to be the result from the finest mesh simulation, and the adaptive mesh results can now be compared to this.

The adaptive mesh result is most similar to the finest resolution fixed mesh result, both in terms of magnitude and flow structure, and is resolving the complex overturning very well.

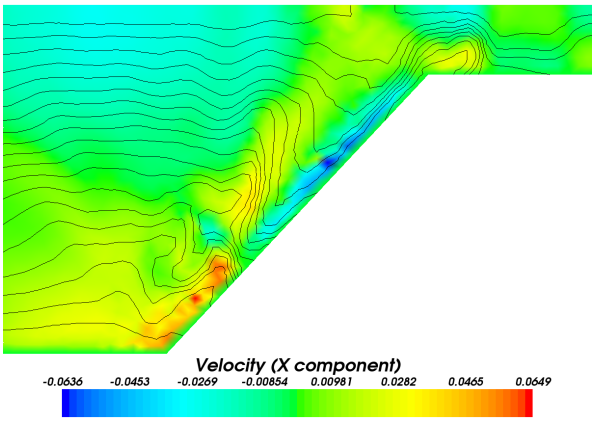
The bolus of more dense fluid that has propagated up the slope and onto the shelf has travelled furthest in the adaptive mesh result. A series of density fronts is also observed in the adaptive case. The adaptive mesh result has lost a perturbation density contour at the top of the domain, which is probably due to the mesh being too coarse there, which is something also visible in the coarsest mesh result. This may be a potential disadvantage of adaptivity when it comes to calculating potential energy in the system, and it may be necessary to restrict the maximum element sizes to those in the simulation ResolutionB.

Half a period later, in figure 6.6, the front is still observable, even in the coarsest simulation. However, the bolus that was at the top of the slope is missing from the coarsest mesh result as the resolution is too coarse to represent it. The bolus has propagated furthest along the shelf for the adaptive mesh result, which suggests that the adaptive mesh result is representing the dynamics accurately.

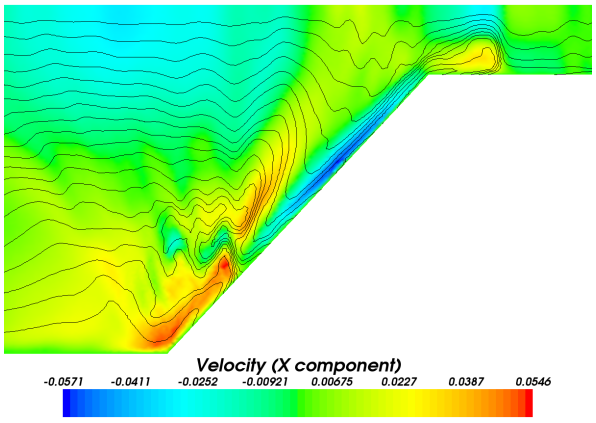
The effect of adapting the mesh to density and u-velocity can be seen in figures 6.5 and



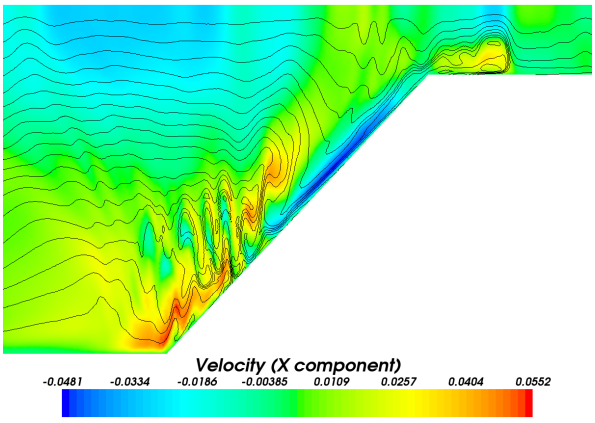
(a) ResolutionA



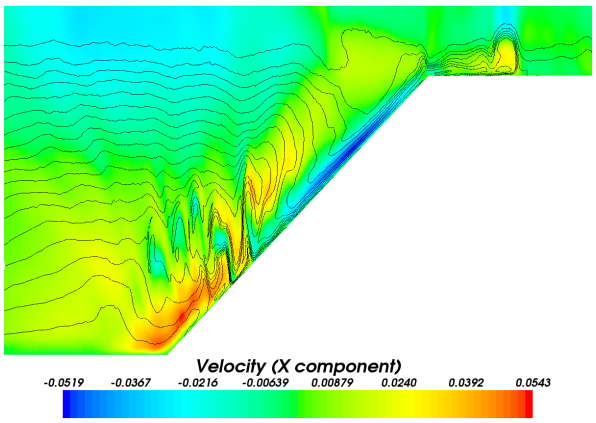
(b) ResolutionB



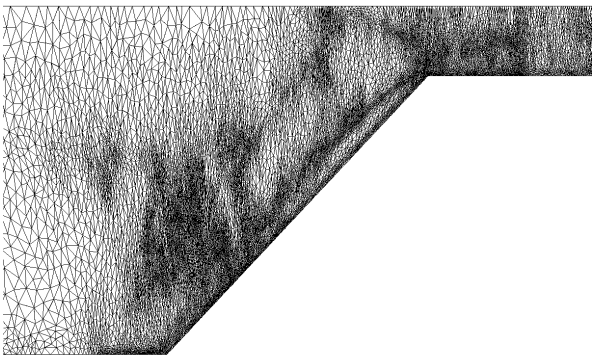
(c) ResolutionC



(d) ResolutionD



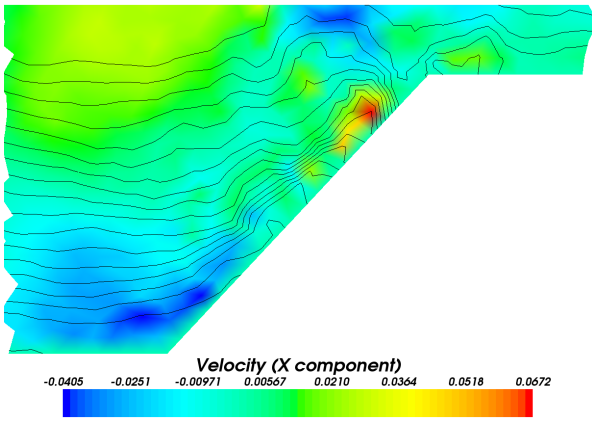
(e) Adaptive result



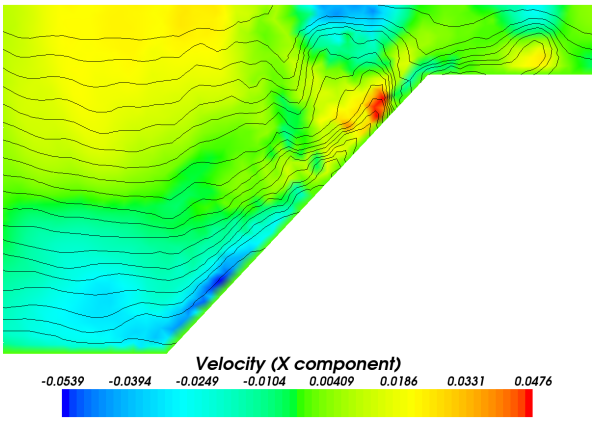
(f) Adaptive result: mesh

Figure 6.5: u–velocity (colour), $\mathrm{m\,s^{-1}}$, and perturbation density (contours) at time $t = 3.0\,T$. The results show the portion of the domain $x \in [1600, 4400]$. The domain has been stretched by a factor of 8 in the vertical to aid visualisation.

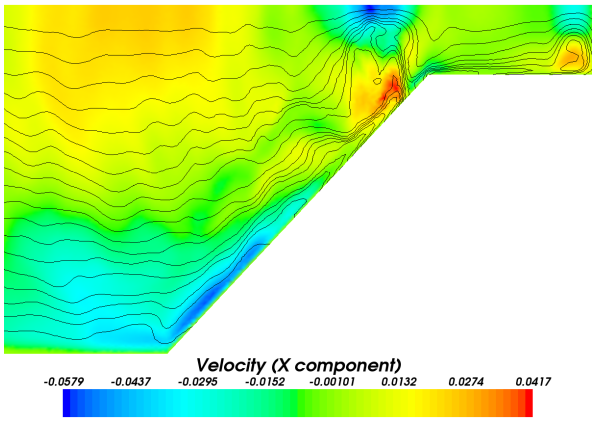
6.6. The no-slip boundary condition on the slope causes large curvature in the u-velocity field, and so extra resolution is placed on the slope to resolve the boundary layer. In panel



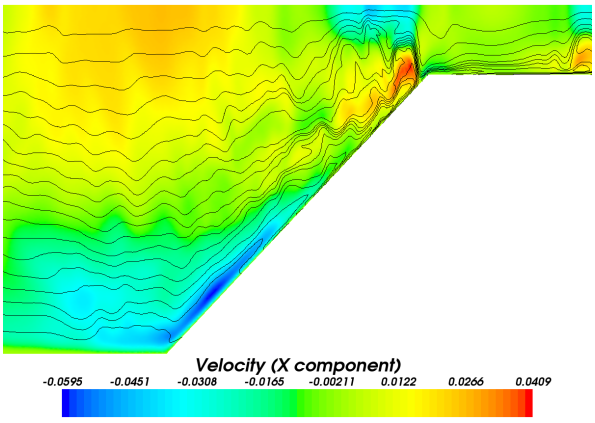
(a) ResolutionA



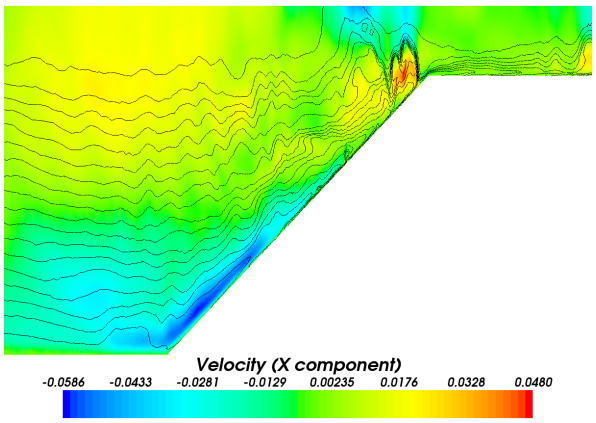
(b) ResolutionB



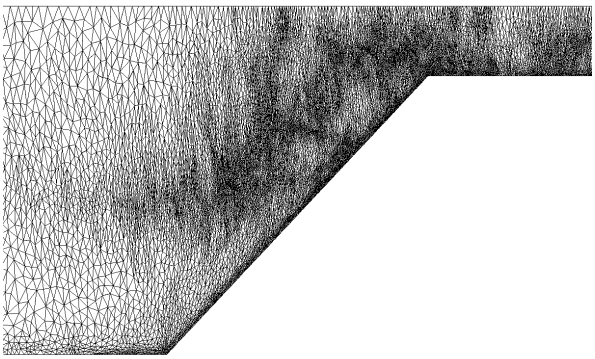
(c) ResolutionC



(d) ResolutionD



(e) Adaptive result



(f) Adaptive result: mesh

Figure 6.6: u–velocity (colour), $\mathrm{m\,s^{-1}}$, and perturbation density (contours) at time $t = 3.5\,T$. The results show the portion of the domain $x \in [1600, 4400]$. The domain has been stretched by a factor of 8 in the vertical to aid visualisation.

(e) of figure 6.5, the upper most contour highlights the curvature of the density field, and the extra resolution put in by the adaptive mesh algorithm can be seen in the same place in

panel (f) of figure 6.5. The density front is also well resolved as the density and u-velocity fields have high curvature there.

One of the merits of using an adaptive mesh model is that the breaking of internal waves can be accurately simulated in a more computationally efficient manner while still adequately resolving the flow. The CPU times taken to achieve the results shown in figure 6.5 and a further two periods are given in table 6.2.1.1. The adaptive mesh simulation is almost 13 times faster than the finest fixed mesh simulation (ResolutionD), and slightly faster than ResolutionC in calculating three periods in the simulation. The time taken for the adaptive mesh simulation to reach five periods is similar to that for SimulationC, and is approximately 8 times faster than ResolutionD.

Simulation	CPU time, s, to get to $3T$	CPU time, s, to get to $5T$
ResolutionA/LeggP	120	200
ResolutionB/LeggQ	1273	2181
ResolutionC/LeggR	13884	23275
ResolutionD/LeggS	124026	211856
Adaptive	9584	25585

Table 6.4: CPU time taken to simulate 3 and 5 periods for the wave breaking MITgcm comparison problem, *i.e.* the results shown in figure 6.5, and two periods later.

One diagnostic that can be used to examine the effectiveness of mesh adaptivity is to look at the total kinetic energy of the fluid in each of the fixed mesh simulations and compare the adaptive mesh result to these. The total kinetic energy (in the Boussinesq sense) in the system is

$$KE = \int_\Omega \frac{1}{2}\rho_0 |\mathbf{u}|^2 d\Omega, \tag{6.1}$$

where Ω is the domain. We use the square of the L^2 norm of velocity magnitude as a metric to compare the adaptive mesh result to the fixed mesh results:

$$\int_\Omega |\mathbf{u}|^2 d\Omega, \tag{6.2}$$

which is plotted against time in figure 6.7.

Figure 6.7 shows the integral over the whole domain of the square of the L^2 norm of velocity magnitude against time for increasing resolution, along with the adaptive mesh result. The four fixed mesh results indicate a convergence, particularly after three periods. Howvever, the adaptive mesh result does not seem to be accurately representing the kinetic

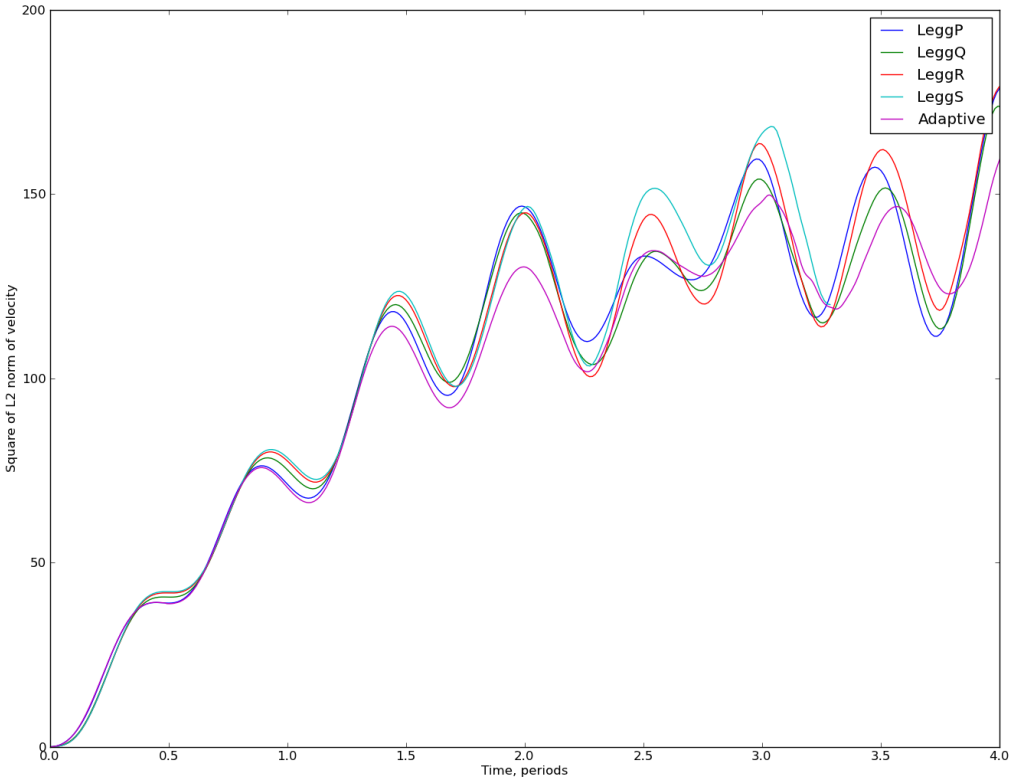


Figure 6.7: Square of the L^2 norm of velocity magnitude against time for increasing resolution for the wave breaking MITgcm comparison test case.

well at all. This is because there are still coarser regions of the mesh in areas of the domain where we are not as interested in the dynamics, but still contribute a significant amount to the total kinetic energy in the domain. At the boundary where the wave is generated, the element sizes are similar in the adaptive mesh result to those in ResolutionA, so the kinetic in the entire domain should not expect to be accurately represented.

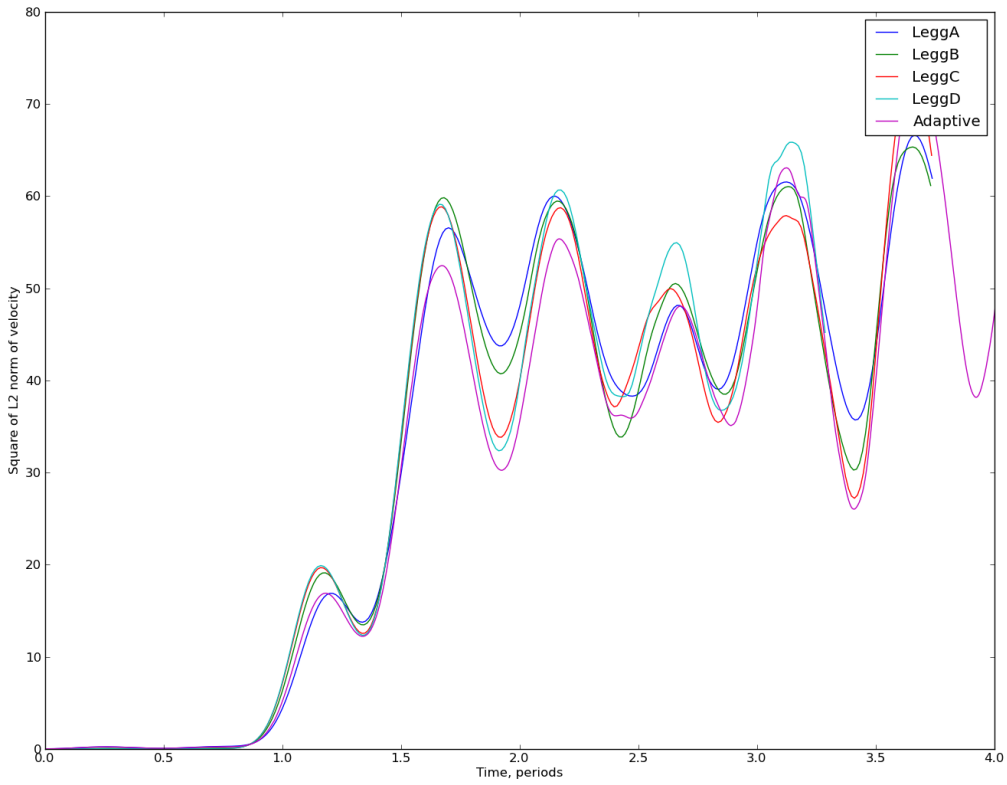


Figure 6.8: Square of the L^2 norm of velocity magnitude evaluated in the slope region, $x \in [2400, 3600]$, against time for increasing resolution for the wave breaking MITgcm comparison test case.

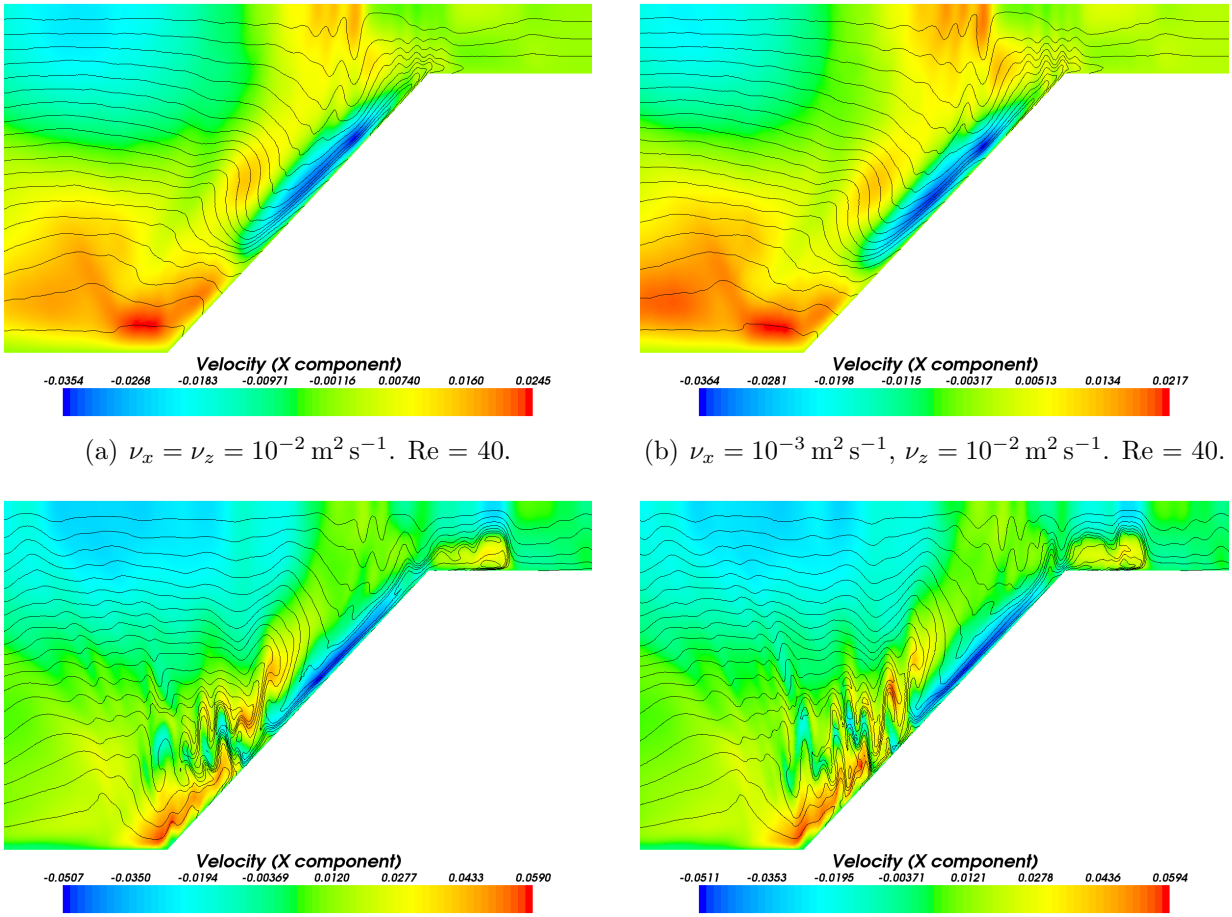
A more relevant metric to evaluate the adaptive mesh result is to calculate the kinetic energy of the system in the region of interest *i.e.* at the slope. Figure 6.8 shows the square of the L^2 norm of velocity magnitude in the region $x \in [2400, 3600]$ against time. In the first two periods, the adaptive mesh result most closely resembles the coarsest mesh result, ResolutionA, which is to be expected since the wave has not by then interacted with the slope, so the mesh will not yet have been refined. Later in the simulation, between 3 and 3.5 periods, the adaptive mesh result seems to be in between the finer mesh resolutions,

ResolutionC and ResolutionD.

These diagnostics could be improved by specifying smaller maximum element sizes, so that the regions with large kinetic energy density as well as the breaking region are both adequately resolved. However, it must be stated that it is difficult to capture the benefits of adaptivity in a single metric.

6.2.1.2 *The effect of viscosity — Reynolds number, Re*

We have performed simulations with the horizontal and vertical viscosities the same, and also with them different by a factor of 10. The Reynolds number is given by $\mathrm{Re} = \frac{UL}{\nu}$. We examine whether the horizontal or vertical component of the viscosity has more influence on the nature of the flow and so the appropriate Reynolds number to characterise that flow.



(a) $\nu_x = \nu_z = 10^{-2}\,\mathrm{m^2\,s^{-1}}$. $\mathrm{Re} = 40$.

(b) $\nu_x = 10^{-3}\,\mathrm{m^2\,s^{-1}}$, $\nu_z = 10^{-2}\,\mathrm{m^2\,s^{-1}}$. $\mathrm{Re} = 40$.

(c) $\nu_x = 10^{-2}\,\mathrm{m^2\,s^{-1}}$, $\nu_z = 10^{-3}\,\mathrm{m^2\,s^{-1}}$. $\mathrm{Re} = 400$.

(d) $\nu_x = \nu_z = 10^{-3}\,\mathrm{m^2\,s^{-1}}$. $\mathrm{Re} = 400$.

Figure 6.9: u–velocity (colour), $\mathrm{m\,s^{-1}}$, and perturbation density (contours) at time $t = 3.0\,T$. The results show the portion of the domain $x \in [1600, 4400]$.

The most viscous results show little wave breaking and reduced velocities. The results with vertical viscosity $\nu_z = 10^{-2}\,\mathrm{m^2\,s^{-1}}$ but with different horizontal viscosities are qualitatively similar with comparable velocity magnitudes. This suggests that vertical viscosity is more important than horizontal viscosity and so in our Reynolds number we use the vertical viscosity, $\mathrm{Re} = \frac{UL}{\nu_z}$, with $U = U_0$ and $L = \frac{U_0}{\omega}$ is an advective lengthscale.

For this experiment we used a fixed mesh (set as for simulation D, Figure 6.5) with viscosity increased by a factor of 10 (viscosity) in either the horizontal or vertical directions or both the horizontal and vertical directions. When viscosity is varied in horizontal direction panels (a) and (b) of figure 6.9, the resultant density contours and velocity magnitudes are very similar. However, when viscosity is varied in the vertical direction, panels (a) and (c) of figure 6.9, there is more overturning in the isopycnals and much larger horizontal velocity magnitudes. Comparing this to a simulation when we decrease both the horizontal and vertical viscosity by a factor of 10, (comparing panlels (c) and (d) of figure 6.9) suggests again that horizontal viscosity has no effect.

For the images in figure 6.9, the aspect ratio is stretched by a factor of 8 in the vertical to aid visualisation detail. Therefore the horizontal extent of the domain is much more than the vertical thus the dynamics will be much more sensitive to changes in the vertical viscosity. This demonstration that changes in the vertical viscosity is more important than changes in horizontal will inform future model runs.

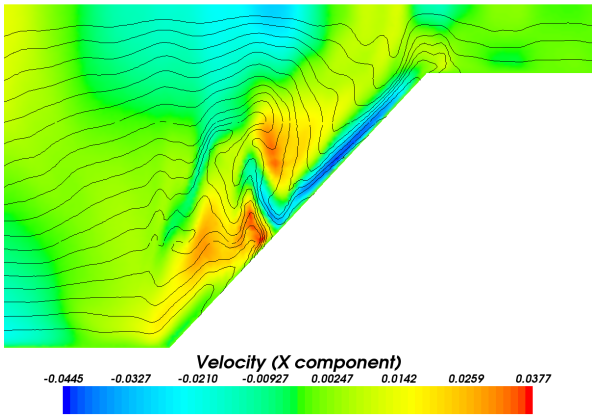
6.2.1.3 The effect of rotation — f. A 3D result.

Legg and Adcroft (2003) include Coriolis in their simulations, and calculate two Rossby numbers, $\mathrm{Ro} = \frac{U}{fL}$, based on an advective lengthscale $L = \frac{U_0}{\omega}$ and on a wavelength scale $L = \lambda_x = \frac{2\pi}{k}$. For the parameters used here, on the advection scale, $\mathrm{Ro} = 1.4$ and on the wavelength scale $\mathrm{Ro} = 0.08$ which suggests that rotation is important for the wave motion but may not influence the advective motions associated with mixing.

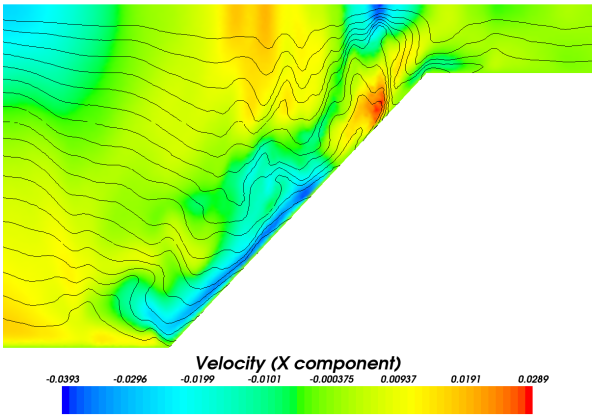
Simulations have been performed in three dimensions in a periodic domain with a Coriolis parameter $f = 1.0 \times 10^{-4}$. We change the buoyancy from the previous simulations to $N = 7.59 \times 10^{-4}\,\mathrm{rad\,s^{-1}}$ so that the angle of the wave beams is still critical, according to the dispersion relation (2.41).

Mesh adaptivity can not be used in periodic domains (as required by a rotating frame in this case), so we run this simulation on a fixed mesh. The results from Fluidity–ICOM and the MITgcm models are shown in figure 6.10. The two snapshots for each model are taken half a period apart, but not at the same times as the ratio of the length of the domain before the slope to the horizontal wavelength is not the same; we have thus matched up the corresponding results.

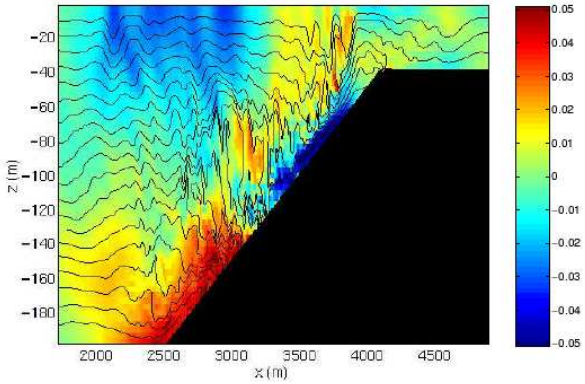
The most important difference to note is that the horizontal phase speed is much less than previously; the wave has propagated much less further towards the slope than after three tidal periods for the non-rotating case. See, for instance, figure 6.9. This is due to the fact that the wavenumber is not confined to the x-z plane; it also has a component in the y-direction, and the component of the wavenumber, and so the phase velocity, in the x-direction is smaller. So, rotation is important on the wavelength scale, but since the Rossby number for the advective motions is much larger, we do not include rotation in the subsequent simulations where we are interested in the smaller scale dynamics at the slope.



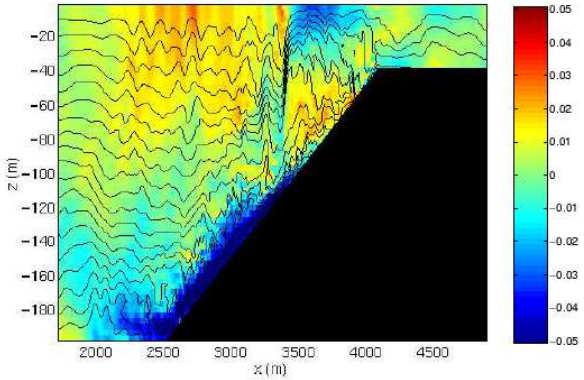
(a) Coriolis, $t = 5.25\,T$



(b) Coriolis, $t = 5.80\,T$



(c) MITgcm, $t = 5.39\,T$



(d) MITgcm, $t = 5.94\,T$

Figure 6.10: u–velocity (colour), $\mathrm{m\,s^{-1}}$, and perturbation density (contours) at various times. The results show the portion of the domain $x \in [1600, 4400]$. The domain has been stretched by a factor of 8 in the vertical to aid visualisation. The MITgcm results are taken from Legg and Adcroft (2003).

6.2.1.4 The effect of slope angle and slope shape — α

We now investigate how the angle of the planar slopes as well as slope shape influences the breaking problem. We perform six numerical simulations and compare two of these to those in Legg and Adcroft (2003). The slope angles for the simulations in a domain with a planar slope are listed in table .

Simulation	s	α°
Sub	$\frac{1}{10}$	5.71
Crit	$\frac{2}{15}$	7.60
Super	$\frac{1}{5}$	11.31

Table 6.5: Table of parameters used in the simulations of wave interaction with a planar slope.

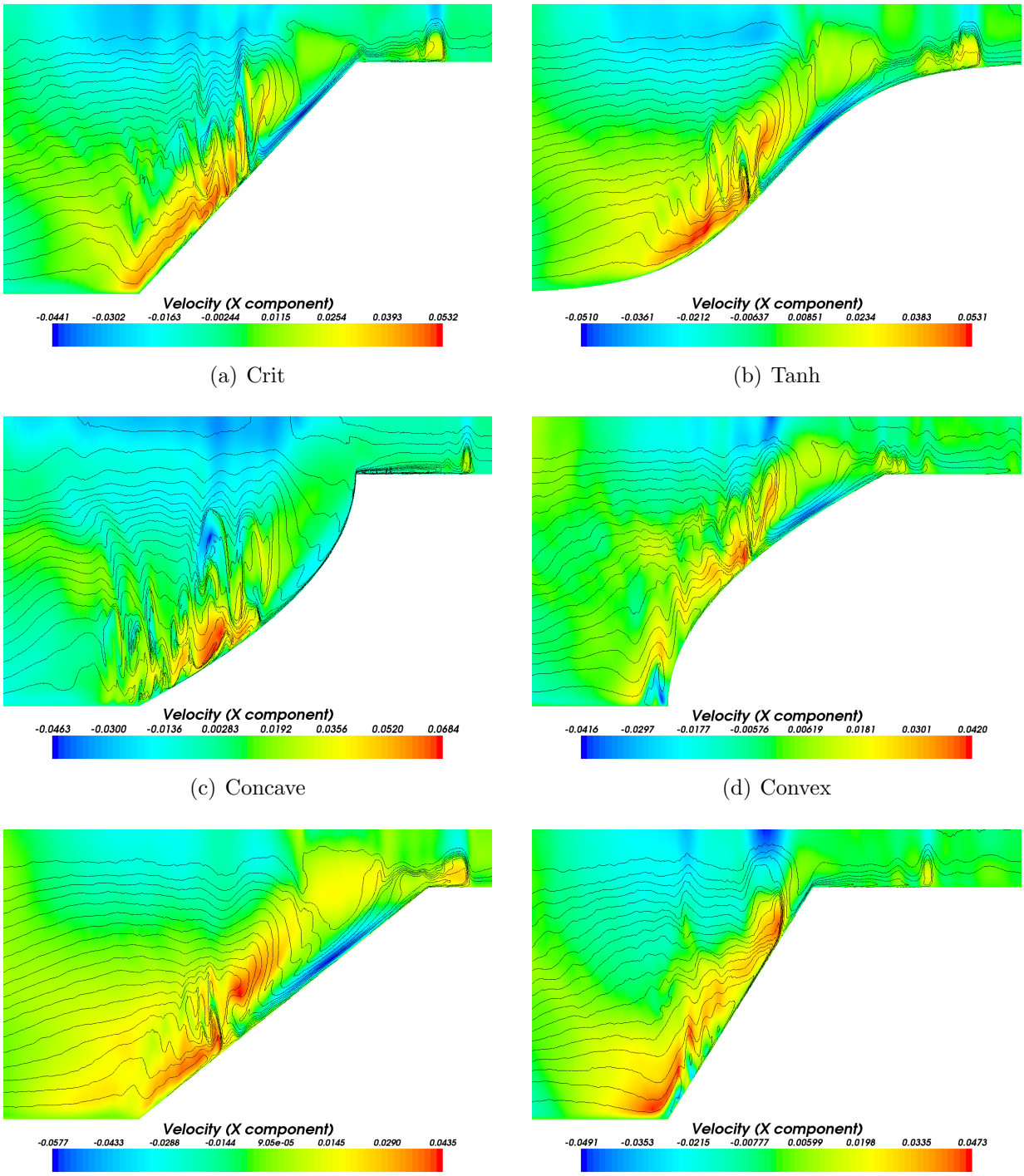
The simulations from the previous section suggested that Coriolis does have an affect on the wave propagation, but not on the wave breaking, and it is the wave breaking that is compared with Legg and Adcroft (2003). The simulations in this section do not include Coriolis, and although we compare these results with those from Legg and Adcroft (2003), which do include the Coriolis, the only significant difference is the horizontal phase speed, rather than the smaller scale advective motions at the slope.

In figure 6.11, a sharp density front, or bore, is visible almost halfway up the slope in the critical, tanh and concave simulations. This bore has reached slightly further in the convex and supercritical simulations, and is further downslope for the subcritical simulation.

There is a convergent flow associated with the bore, with upslope flow (shown in red) behind the bore and downslope flow (shown in blue) in front of it. The magnitudes of these flow–velocities are similar for the critical and the tanh results. The concave result exhibits the greatest horizontal velocity, as the flow has to accelerate up the slope which is increasing in gradient. There is also a bore clearly visible on the shelf, in particular in the critical, tanh and subcritical simulations.

Overturning of the isopycnals, associated with wave breaking, is most noticeable in the subcritical result, clearly demonstrating the non–hydrostatic capability of the model.

At a later time, as shown in figure 6.12, the flow associated with the bore is now divergent, the denser fluid that was carried up the slope accelerating back down under gravity, and the fluid in the bore is propagating up the slope. The bore that had made it up onto the shelf in the results at $3.1T$ (figure 6.11) has now propagated further along the shelf,



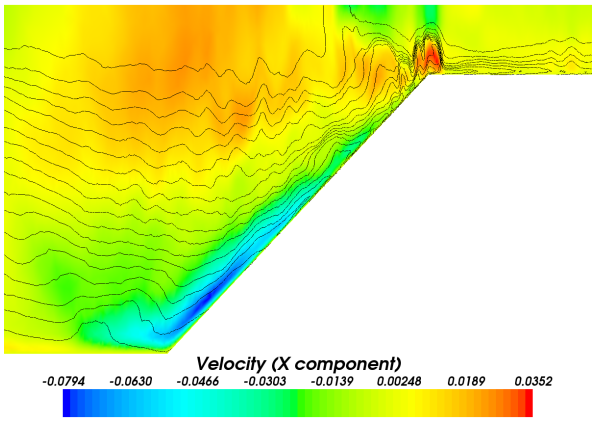
(a) Crit (b) Tanh

(c) Concave (d) Convex

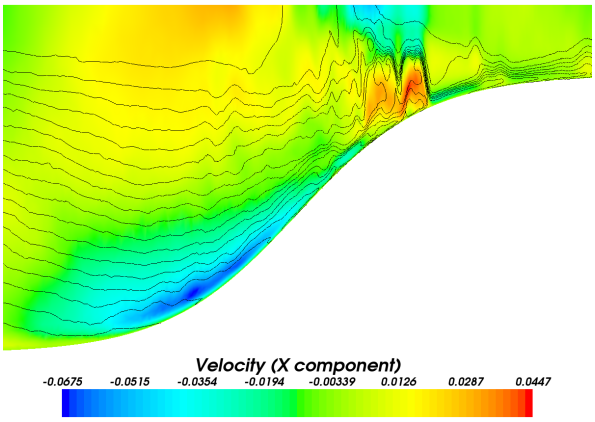
(e) Sub (f) Super

Figure 6.11: u–velocity (colour), $\mathrm{m\,s^{-1}}$, and perturbation density (contours) at time $t = 3.1\,T$. The results show the portion of the domain $x \in [1600, 4400]$. The domain has been stretched by a factor of 8 in the vertical to aid visualisation.

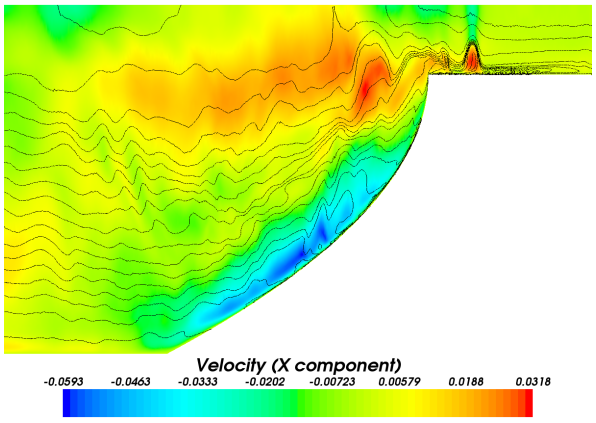
with another one forming at the top of the slope for the critical and convex simulations, and already propagating further along the shelf for the supercritical and concave simulations.



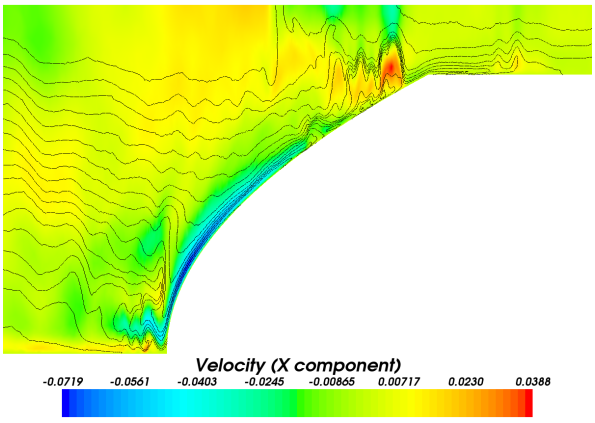
(a) Crit



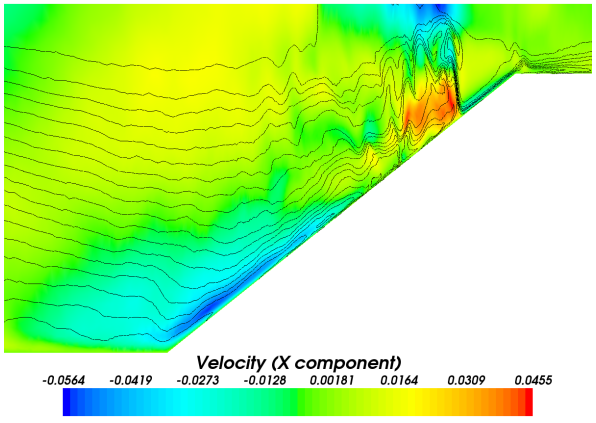
(b) Tanh



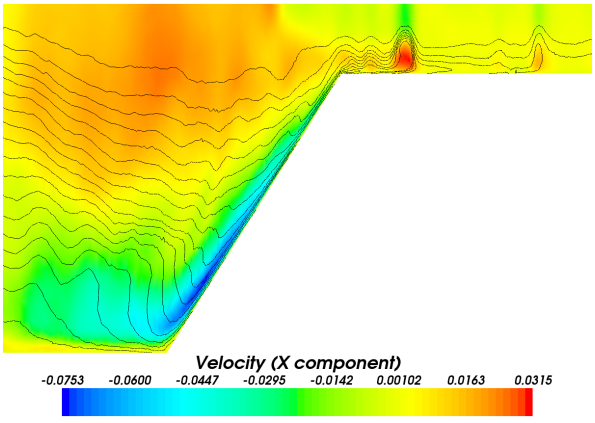
(c) Concave



(d) Convex



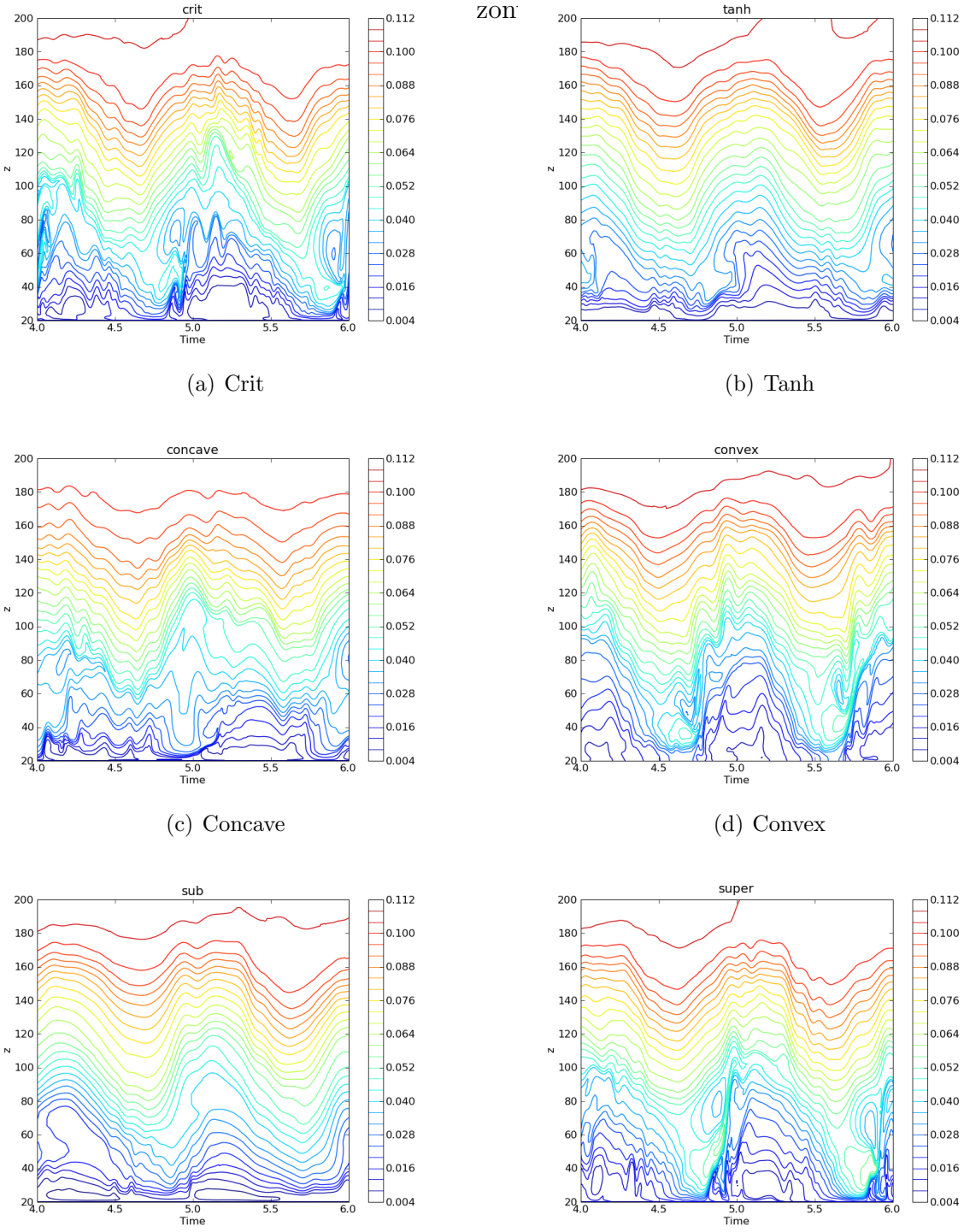
(e) Sub



(f) Super

Figure 6.12: u–velocity (colour), $\mathrm{m\,s^{-1}}$, and perturbation density (contours) at time $t = 3.6\,T$. The results show the portion of the domain $x \in [1600, 4400]$. The domain has been stretched by a factor of 8 in the vertical to aid visualisation.

The evolution of the flow can be also be examined with time–depth plots of the velocity and density fields at a vertical cross–section of the domain through a point on the slope.



(a) Crit (b) Tanh

(c) Concave (d) Convex

(e) Sub (f) Super

Figure 6.13: Contour plots of perturbation density against depth and time where $z = 20\,\mathrm{m}$.

The pertubation density plots, figure 6.13, show dense fluid displaced upslope. The tightly bunched contours in panel (a), at $t = 4T$, $t = 5T$ and $t = 6T$ show a periodic bore. These periodic bores are also seen in the convex case (panel (d)), one of which is visible in

panel (d) of figure 6.14 at the bottom of the slope near to $z = 20\,\mathrm{m}$ and also in the super critical case panel (f) of figure 6.14.

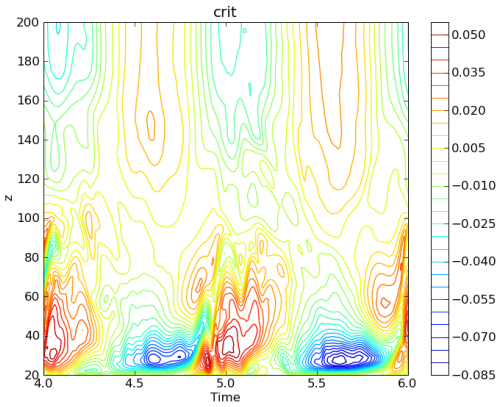
For the tanh simulation (panel (b) of figure 6.13) and the subcritical simulation (panel (e) of figure 6.13), the contours are less tightly bunched and this is due to the fact that the bore was only formed upslope of $z = 20\,\mathrm{m}$. For the concave case (panel (c) of figure 6.13), the odd behaviour of the contours in depths between $z = 20\,\mathrm{m}$ and $z = 60\,\mathrm{m}$ may be due to what appears to be multiple bores as seen in panel (c) of figure 6.11 towards the bottom of the slope.

Figure 6.14 shows that boundary layer is clearly resolved in all of the simulations. The critical planar slope (panel (a)) again shows larger velocity magnitudes and the most variability in velocity over time compared to the concave and subcritical slopes. The concave result (panel (c)), is similar to the subcritical case (e) in the overall shape of the contours. This is because the slope at the depth $z = 20\,\mathrm{m}$ of the concave case is similar to that of the sub-critical. However for velocity magnitude the concave case shows larger values. This could be because over the two periods fluid has been transported both up and down the slope, and the gradient of the bathymetry upslope means that the vertical component of the acceleration of the fluid from the top of the concave slope is greater leading to larger velocity magnitudes.

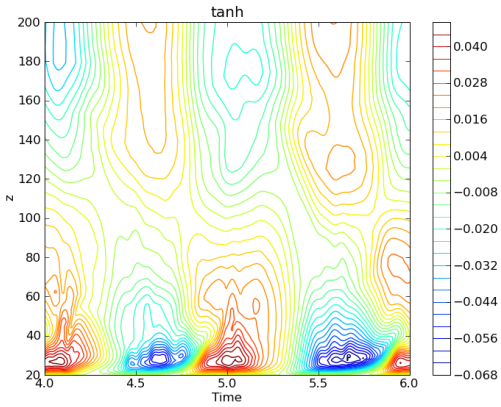
The tanh slope (panel (b)) also has similar contours to both the concave and sub critical slopes. The velocity magnitudes for the tanh slope are somewhere between those for the concave and subcritical slopes, because the gradient of the bathymetry upslope of $z = 20\,\mathrm{m}$ is smaller than the concave case but larger than the subcritical case.

The convex result (panel (d)) is similar to the super critical result (panel (f)), in terms of the shape of the contours, again as the two cases have the same slope at $z = 20\,\mathrm{m}$. However this time it is the supercritical case which has larger velocity magnitudes this is once again due to the gradient of the bathymetry upslope being steeper for the supercritical case than for the convex case.

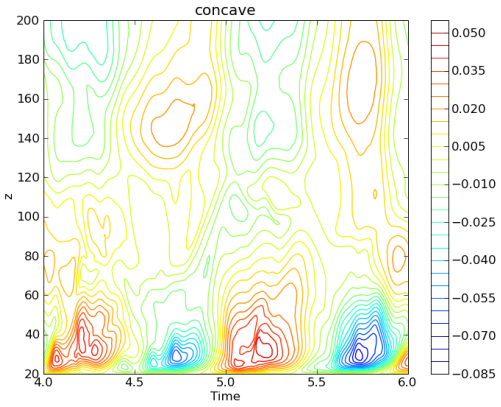
The direction of phase propagation can be inferred from these contour plots. There is a slight downward phase propagation visible in the flow at a depth of approximately $z = 70\,\mathrm{m}$. This could be as a result of the decoupling of the upward and downward propagating wave beams.



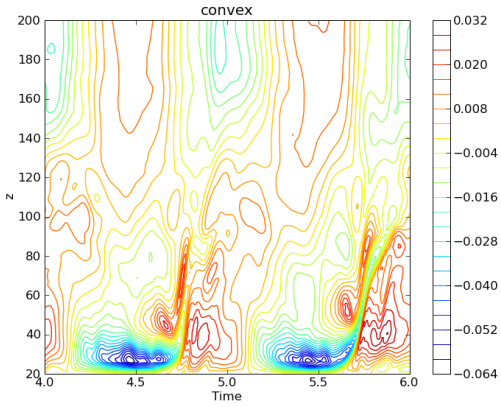
(a) Crit



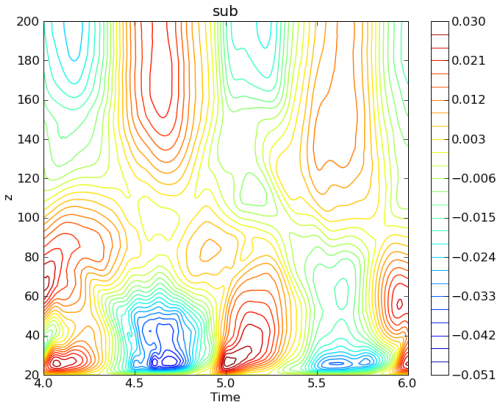
(b) Tanh



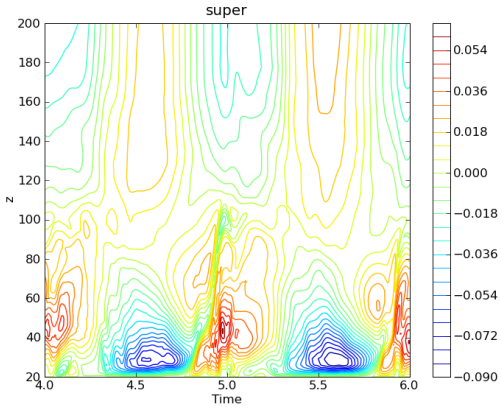
(c) Concave



(d) Convex

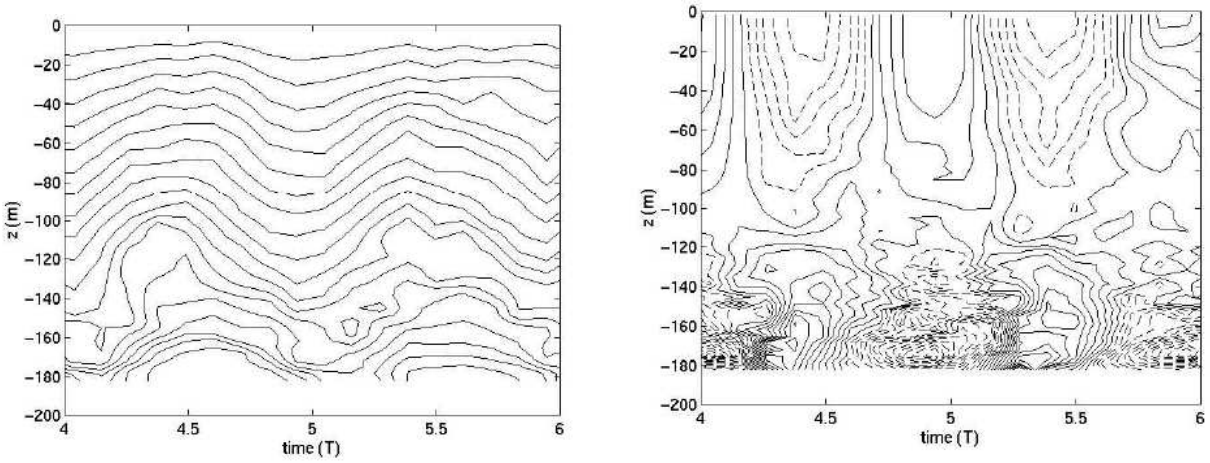


(e) Sub



(f) Super

Figure 6.14: Contour plots of u–velocity, $\mathrm{m\,s^{-1}}$, against depth and time where $z = 20\,\mathrm{m}$.



(a) MITgcm - perturbation density

(b) MITgcm - u velocity

Figure 6.15: MITgcm results. Contour plots of perturbation density and u velocity against depth and time where the $z = 20\,\text{m}$. Taken from Legg and Adcroft (2003).

Contour plots of the perturbation density and horizontal velocity from the results from the MITgcm model are shown in figure 6.15. The boundary layer does not seem to be resolved, but there is suggestion of the periodic bore in the contour plot for horizontal velocity.

6.2.1.5 Conclusions

The breaking of internal waves at slopes of various shapes has been investigated. Fixed mesh simulations were carried out on meshes of increasing resolution, as well as adaptive mesh simulations. The adaptive mesh simulation captured the dynamics of the wave breaking but did not accurately represent the kinetic energy of the entire domain. The kinetic energy at the slope was better modelled by the adaptive mesh result but further work to tune the adaptivity parameters and to devise an appropriate diagnostic for how well adaptivity is performing is needed. The adaptive mesh results demanded less computational resources, and adequately captured the most important features of the wave breaking. It must be stated that there can be an additional overhead with adaptivity, in that several simulations may have to be run to achieve an adaptive mesh result which captures certain dynamics.

Simulations with different viscosities in the horizontal and vertical were performed and it was found that vertical viscosity has more impact on the dynamics than horizontal

viscosity. The effect of rotation was included in two (fixed mesh) simulations and this showed that rotation is important on the wavelength scale, but not in the smaller scale dynamics of the wave breaking at the slope.

Internal wave breaking at six differently shaped slopes has been studied, and the dynamics of the breaking event for each case have been discussed. All of the shapes led to the generation of upslope propagating bores. Further work is required is quantify the net change in stratification to quantify the mixing at the slope.

6.2.2 Comparison with SUNTANS — a laboratory scale numerical simulation

6.2.2.1 Adaptive mesh results

As the incident wave interacts with the slope, a front is generated at the bottom of the slope followed by overturning of the isopycnals (c and d of figure 6.16). The overturned fluid travels upslope (e and f) and generates a "bolus" that continues to propagate along the shelf (g onwards). The more dense fluid on the slope behind the bolus slumps back downslope (g and h) and interacts with the new wave arriving at the slope (i) with even more overturning of the isopycnals and subsequent mixing. Again, dense fluid travels upslope (j and k), and another bolus, less dense than the first, is formed (l onwards).

There is good qualitative comparison with the SUNTANS result, figure 6.18. The formation of a bore and transport of more dense fluid onto the shelf is in good agreement. The extra resolution supplied by the adaptive mesh algorithm in the Fluidity–ICOM simulation means that smaller scale features are more accurately resolved than for the SUNTANS result.

The extra resolution that the adaptive mesh algorithm employs can clearly be seen in figure 6.17. As the wave interacts with the slope where smaller scale processes begin to take place, more resolution is focused in on those regions while maintaining coarser, but sufficient, resolution in other regions.

6.2.2.2 Nonlinear effects — Froude number, Fr

The effect of increasing the Froude number, defined as the ratio of the velocity magnitude of the incoming wave U_0 to the phase speed $c_p = \frac{\omega}{k}$, is examined through a series of simulations with Fluidity–ICOM. Five different Froude numbers are considered; 0.2, 0.4, 0.6, 0.8 and 1.0.

Figure 6.19 shows the simulation with a Froude number of 0.2. There is some overturning at the slope, no propagation of a bolus onto the shelf.

Figure 6.20 shows the simulation with a Froude number of 0.4. Again, there is some overturning at the slope. A small amount of denser fluid has been transported onto the shelf (panel (c)), but this quickly diffuses away as it travels along the shelf (panel (d)).

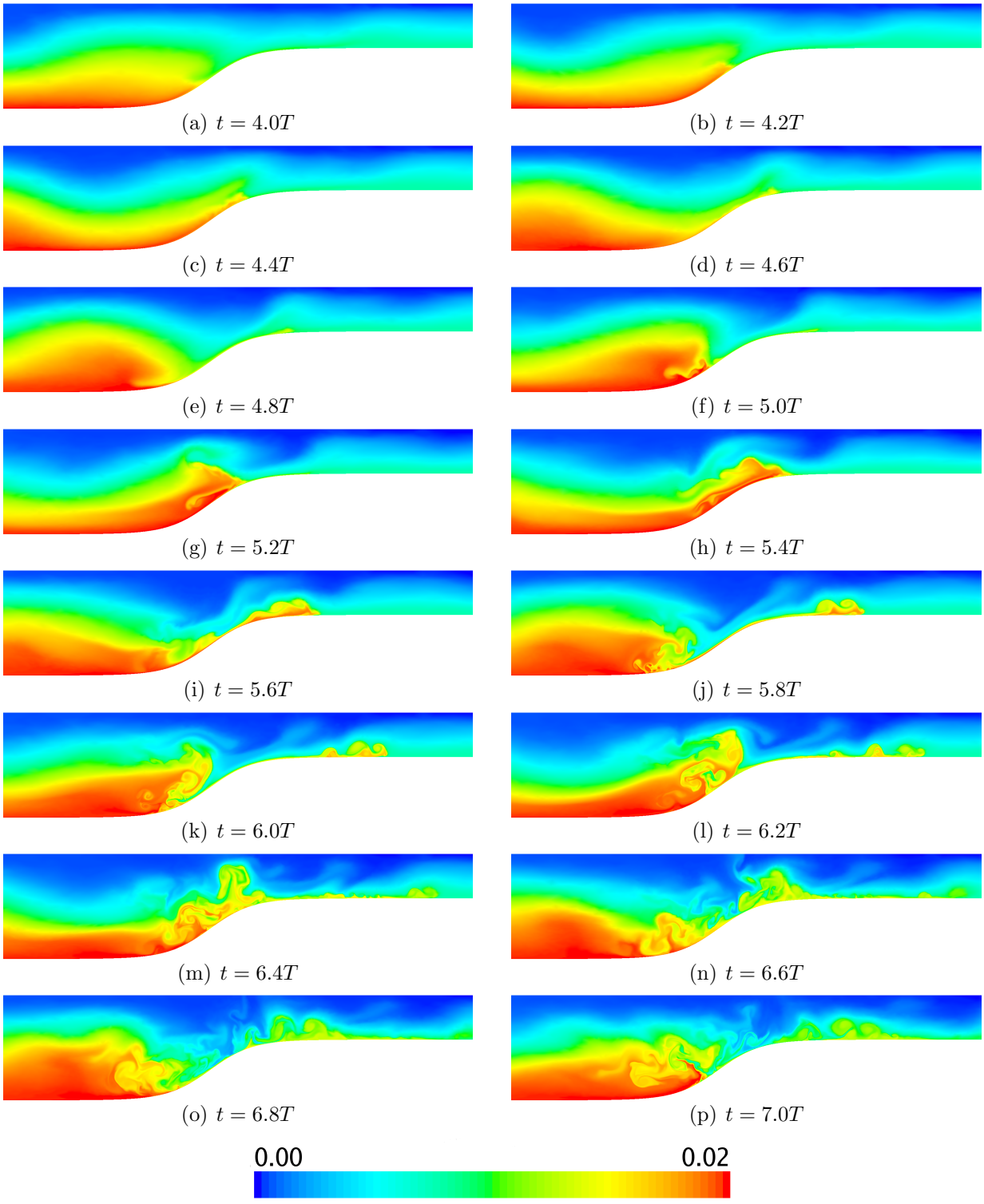
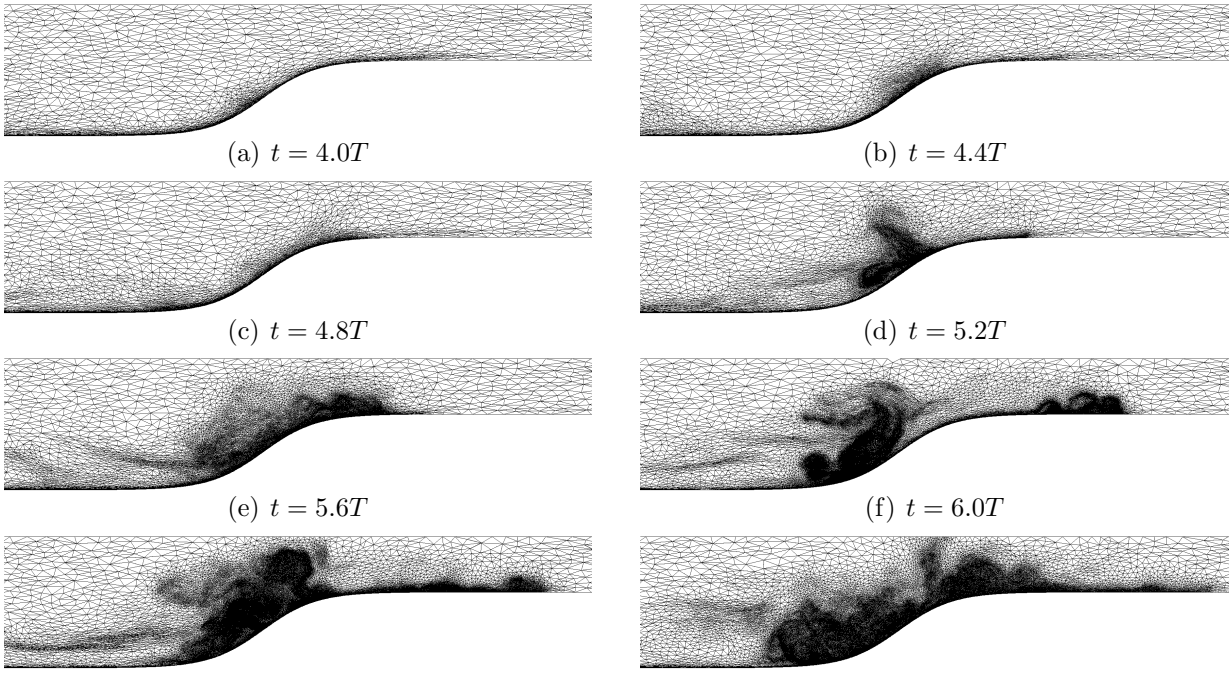


Figure 6.16: Perturbation density, $\frac{\rho(\mathbf{x},t)}{\rho_0} - 1$, in the adaptive mesh Fluidity-ICOM simulation of the laboratory scale wave breaking problem. T is the period of the forcing. Compare with the corresponding SUNTANS result shown in figure 6.18.



(a) $t = 4.0T$ (b) $t = 4.4T$ (c) $t = 4.8T$ (d) $t = 5.2T$ (e) $t = 5.6T$ (f) $t = 6.0T$ (g) $t = 6.4T$ (h) $t = 6.8T$

Figure 6.17: The adaptive mesh in the Fluidity-ICOM simulation of the laboratory scale wave breaking problem. T is the period of the forcing.

Figure 6.21 shows the simulation with a Froude number of 0.6. There is some overturning at the slope, and a bolus has developed which has propagated along the shelf (panel (c)). The bolus dissipates as it travels along the shelf (panel (d)).

Figure 6.22 shows the simulation with a Froude number of 0.8. There is a shear instability as the denser fluid is pushed up onto the shelf (panel (b)), and again a bolus has developed which has propagated along the shelf (panel (c)). The bolus dissipates as it travels along the shelf (panel (d)).

Figure 6.23 shows the simulation with a Froude number of 1.0. This simulation exhibits the most dynamic features, with shear instability already developed in panel (a), and further shear instability shown later in the simulation as denser fluid propagates along the shelf (panel (b)), and gravitational instability as overturned dense fluid collapses on top of the less dense fluid running back down the slope (panel (c)).

6.2.2.3 Conclusions

The breaking of nonlinear internal waves at a slope has been simulated with Fluidity–ICOM. Good qualititave comparison with SUNTANS has been found, with Fluidity–ICOM

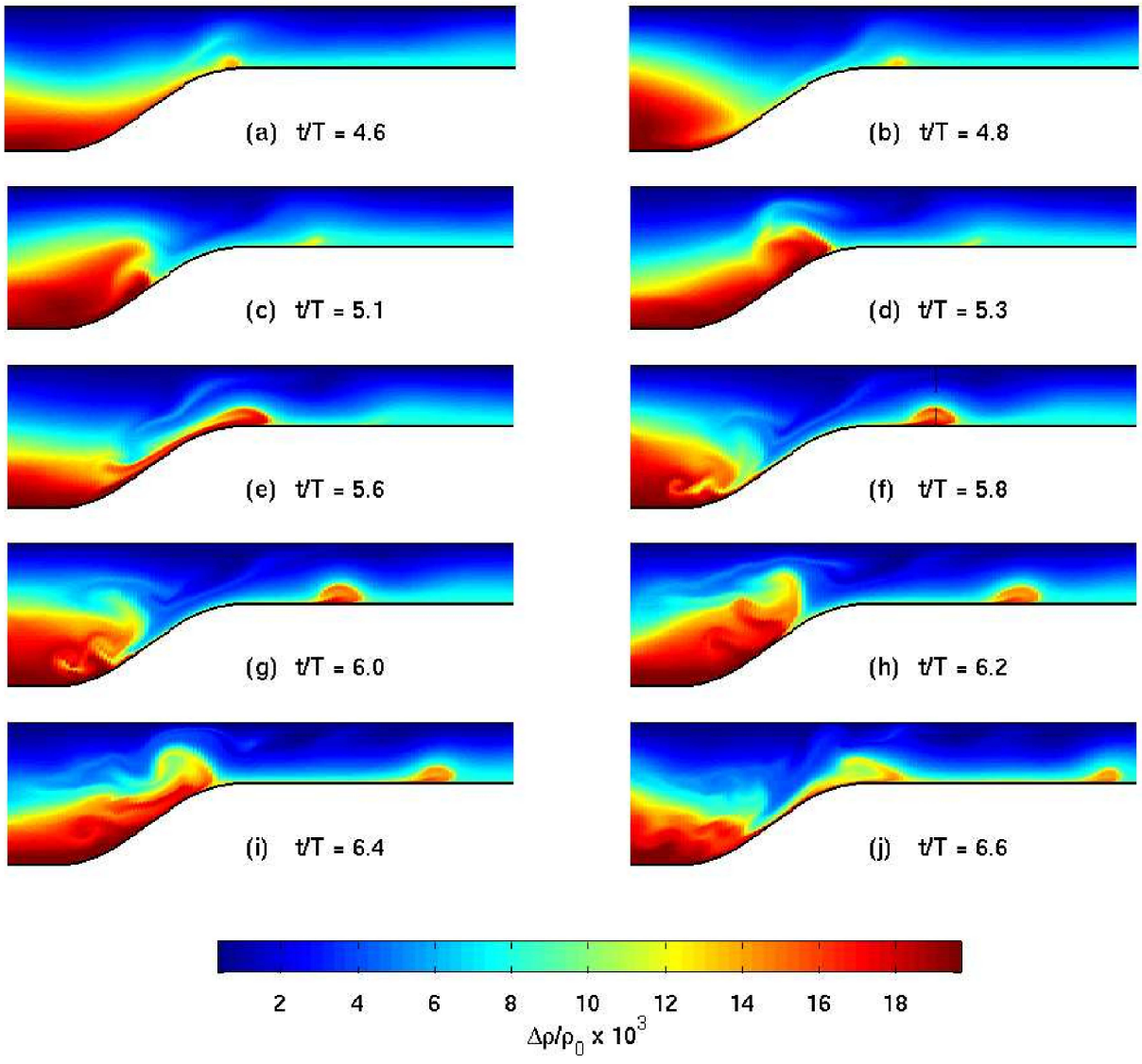
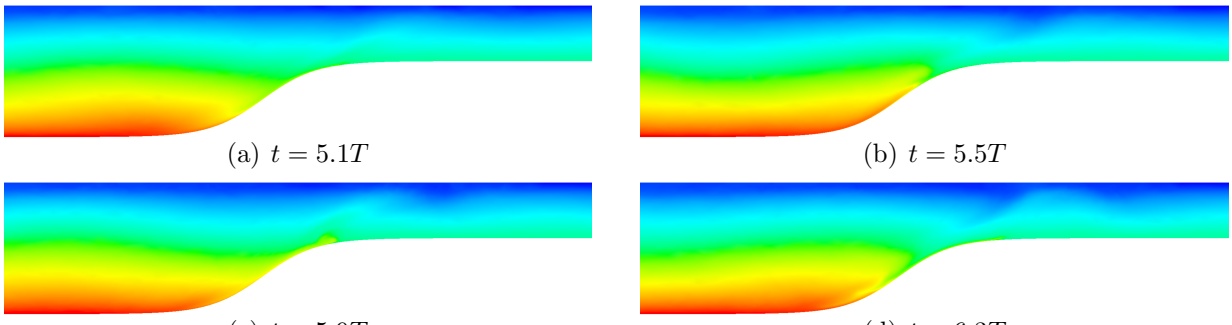


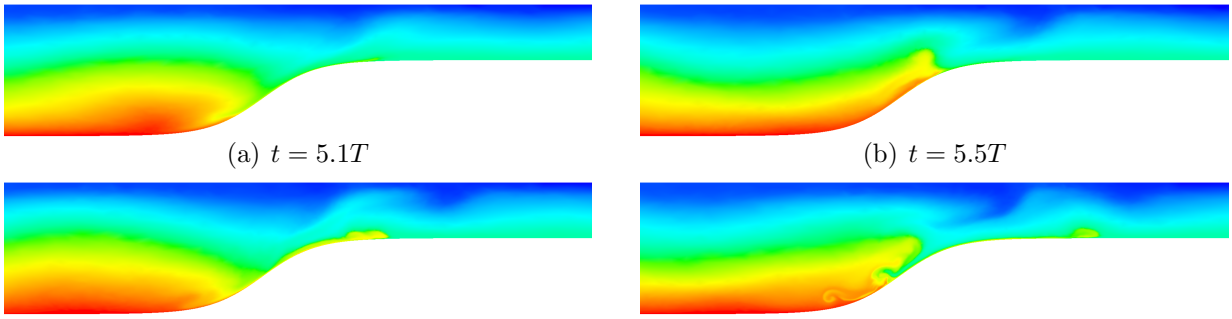
Figure 6.18: SUNTANS result; perturbation density. Taken from Venayagamoorthy and Fringer (2007).



(a) $t = 5.1T$ (b) $t = 5.5T$

(c) $t = 5.9T$ (d) $t = 6.3T$

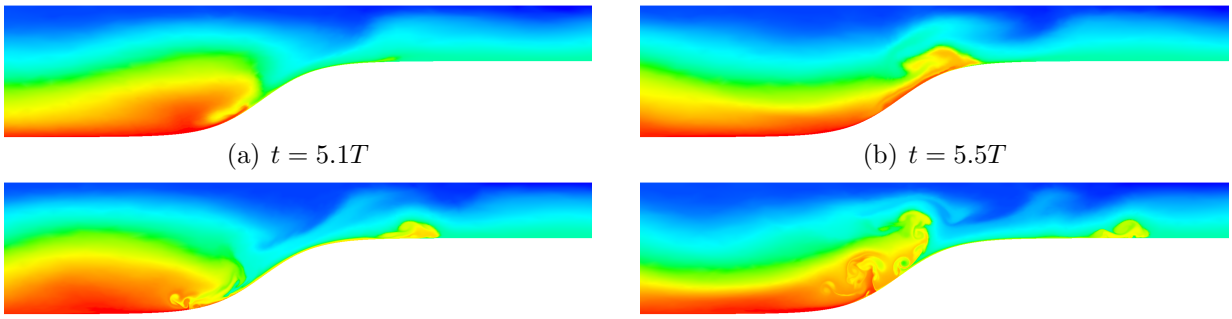
Figure 6.19: Fluidity-ICOM simulation of the laboratory scale wave breaking problem with Froude number Fr $= 0.2$.



(a) $t = 5.1T$ (b) $t = 5.5T$

(c) $t = 5.9T$ (d) $t = 6.3T$

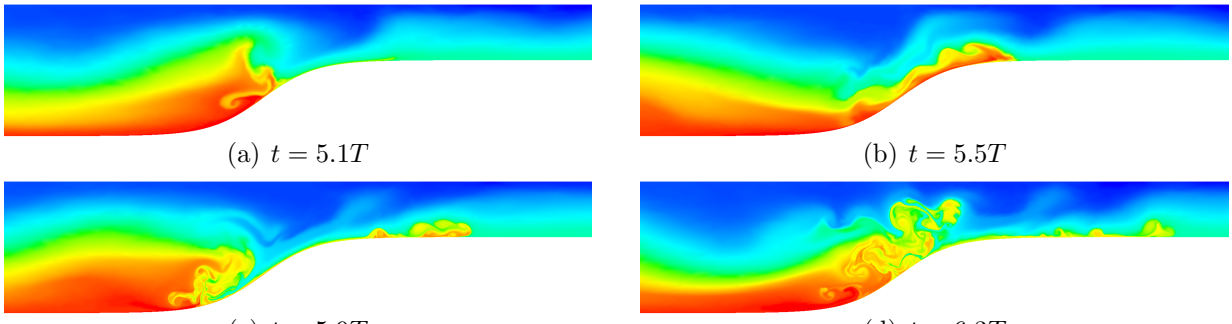
Figure 6.20: Fluidity-ICOM simulation of the laboratory scale wave breaking problem with Froude number Fr $= 0.4$.



(a) $t = 5.1T$ (b) $t = 5.5T$

(c) $t = 5.9T$ (d) $t = 6.3T$

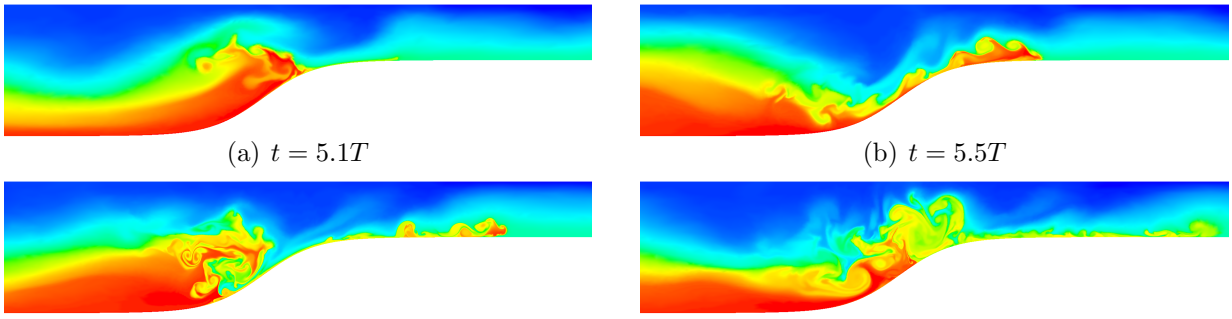
Figure 6.21: Fluidity-ICOM simulation of the laboratory scale wave breaking problem with Froude number Fr $= 0.6$.



(a) $t = 5.1T$ (b) $t = 5.5T$

(c) $t = 5.9T$ (d) $t = 6.3T$

Figure 6.22: Fluidity-ICOM simulation of the laboratory scale wave breaking problem with Froude number Fr $= 0.8$.



(a) $t = 5.1T$ (b) $t = 5.5T$

(c) $t = 5.9T$ (d) $t = 6.3T$

Figure 6.23: Fluidity-ICOM simulation of the laboratory scale wave breaking problem with Froude number Fr = 1.0.

resolving finer details of the dynamics of the simulation than SUNTANS. The effect of increasing the nonlinearity of the internal waves has been briefly investigated, but further work is needed to quantify the energy reflected at the slope.

6.3 Conclusions

The propagation of small amplitude internal waves has been simulated with Fluidity–ICOM, to show model convergence with increasing mesh resolution which was found to be the theoretically expected quadratic value. It can now be said with confidence that Fluidity–ICOM can accurately model internal wave propagation.

Breaking of internal waves in a linearly stratified fluid at a slope was also considered. The adaptive mesh simulation captured the dynamics of the wave breaking but did not accurately represent the kinetic energy of the entire domain. A more appropriate diagnostic for how well adaptivity is performing needs to be devised. The adaptive mesh results demanded less computational resources, and adequately captured the most important features of the wave breaking. It must be stated that there can be an additional overhead with adaptivity, in that several simulations may have to be run to achieve an adaptive mesh result which captures certain dynamics.

Significant progress has been made to validate Fluidity–ICOM. This is the first time internal waves have been simulated with a fully unstructured adaptive mesh model. The adaptive mesh capability of Fluidity–ICOM was tested against fixed mesh simulations, and while there is still work to be done evaluate how well adaptivity works, progress has been made to show that Fluidity–ICOM is indeed capable of modelling internal wave breaking.

Chapter 7

Internal waves in a two–layer fluid

Contents

7.1 Generation 129

7.1.1 Internal lee wave generation in a two–layer fluid 130

7.1.2 Tilting tank 132

7.2 Breaking 138

7.2.1 Dynamics of a shoaling and breaking event 138

7.2.2 Adaptive mesh results with different interpolation errors 142

7.2.3 The effect of diffusivity 144

7.2.4 The effect of the angle of the slope on shoaling and breaking . . 149

7.2.5 Reflectance of pseudoenergy 156

7.3 Conclusions 158

In this chapter the generation and breaking at a slope of internal solitary waves in an idealized, quasi-two layer continuously stratified fluid are investigated numerically with Fluidity–ICOM.

The generation of internal lee waves in a two–layer fluid as a result of flow over a topographic feature are examined, and the results compared with the analytical and laboratory results of Kranenburg and Pietrzak (1989). The wavelength of the lee wave shows favourable comparison with both the analytical and laboratory results; however the wave amplitude is not well–captured by Fluidity–ICOM.

The degeneration of large–scale interfacial waves into a train of solitary waves is modelled numerically with Fluidity–ICOM, and compared with the "tilting tank" results of Horn et al. (2001). Both the high resolution fixed mesh simulations and the adaptive mesh simulations capture all the solitons in the generated wave train, with the adaptive mesh simulation showing a 200–fold increase in computational efficiency.

Finally, the breaking of internal solitary waves at a slope is considered. The results are compared with both experimental laboratory data (Kao et al. (1985); Helfrich (1992); Michallet and Ivey (1999)), and numerical simulations carried out on fixed uniform meshes (Vlasenko and Hutter (2002); Berntsen et al. (2006); Bourgault and Kelley (2007); Lamb and Nguyen (2009)) and meshes with adaptive mesh refinement (AMR) (Barad et al. (2009); Rickard et al. (2009)). The effect of several physical parameters (the amplitude and wavelength of the solitary waves, the diffusivity, and the gradient of the slope) are investigated in relation to the energy reflected at a slope and the mixing that occurs as internal solitary waves break at a slope. Similarly the the sensitivity of the results to parameters in the adaptivity algorithm are also considered.

7.1 Generation

The generation of internal waves in a two–layer fluid is examined in this section. Two generation mechanisms are considered: the internal lee wave generation as a result of stratified flow over topography; and the degeneration of large–scale interfacial waves into

a train of solitary waves.

7.1.1 Internal lee wave generation in a two–layer fluid

7.1.1.1 Fixed mesh results

The simulation did not achieve a steady state as expected, so we compare the result after 90 s of simulation time with the analytical result. Figure 7.1 shows the perturbation density after 90 s. Figure 7.1 shows the interface after 90 s along with the analytical result. The

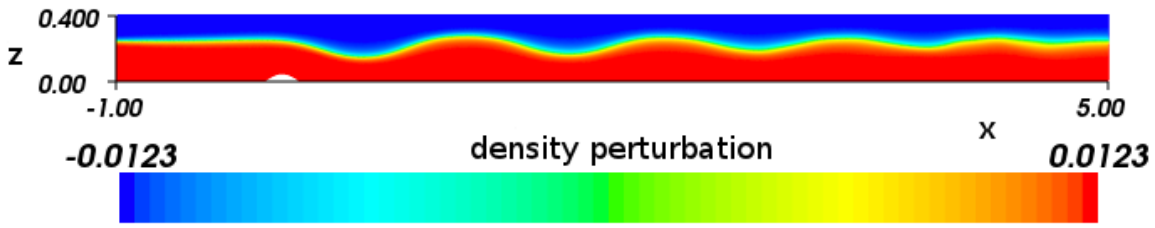


Figure 7.1: Density after 90 seconds in the lee wave generation problem.

wavelength shows favourable comparison, but the amplitude and the displacement from the ambient stratification do not. This is likely due to the fact that the simulation has not reached a steady state. Figure 7.3 shows the results from the laboratory experiment along

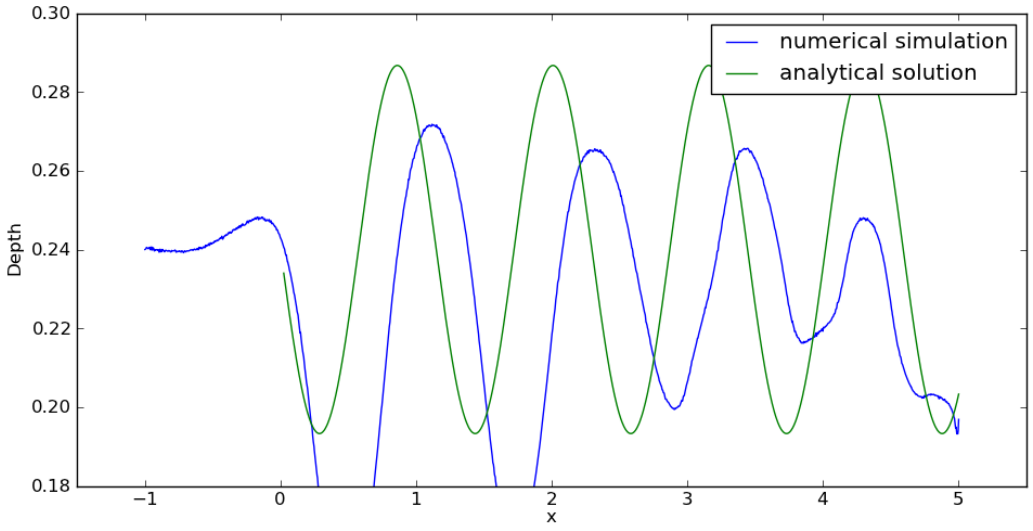


Figure 7.2: Numerical and analytical results for the lee wave generation problem.

with the analytical result. The good agreement suggests that the analytical derivation is correct.

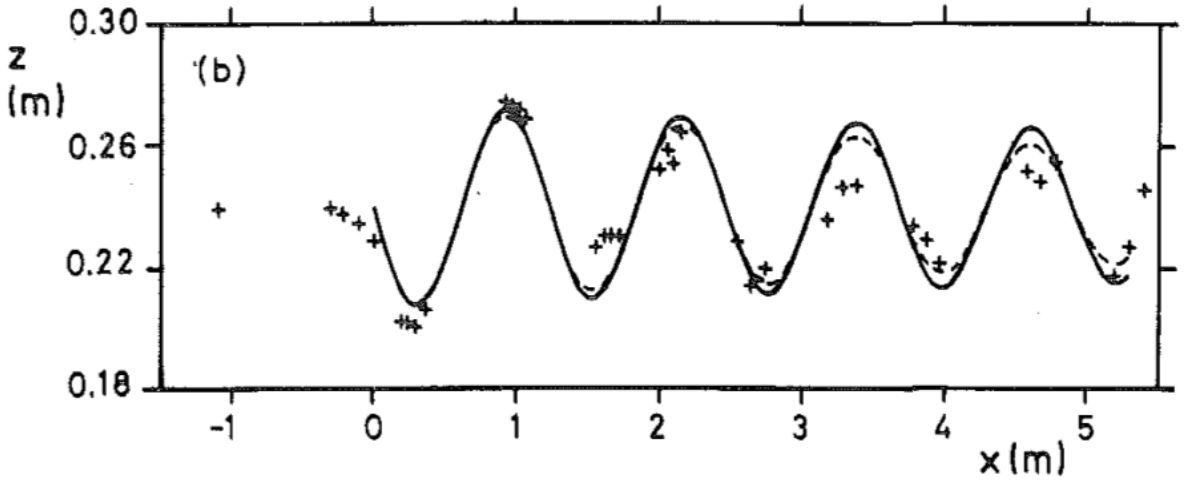


Figure 7.3: Experimental result taken from Kranenburg and Pietrzak (1989). The crosses are the data from the laboratory experiment.

7.1.1.2 Conclusions

We have found good agreement with wavelength predicted from the theoretical analysis. However, the amplitude and displacement from the ambient stratification showed little similarity. Adaptivity is perhaps not much use in this case, since the simulation is expected to reach a steady state. It would be interesting to pursue this test–case further to see if we can reach a steady state with both fixed and adaptive mesh simulations.

The topographic bump in this case has discontinuous gradient, which in the laboratory simulation led to a recirculation region downstream of the bump. It may help to use a smoother topography *e.g.* a Gaussian bump, or, with recent developments in Fluidity–ICOM, a discontinuous Galerkin scheme could be employed.

7.1.2 Tilting tank

7.1.2.1 Fixed mesh results

The fixed mesh results were run in parallel on 64 processors on a uniform mesh with mesh spacing of $\Delta x = \Delta z = 0.001\,\mathrm{m}$ which results in a mesh of 1,746,291 nodes and 3,480,000 elements. The timestep used was $\Delta t = 0.025\,\mathrm{s}$. The evolution of the departure of the interface from its initial position at $x = 0.1\,\mathrm{m}$ is shown in figure 7.5 along with the data from the laboratory experiment of Horn et al. (2001).

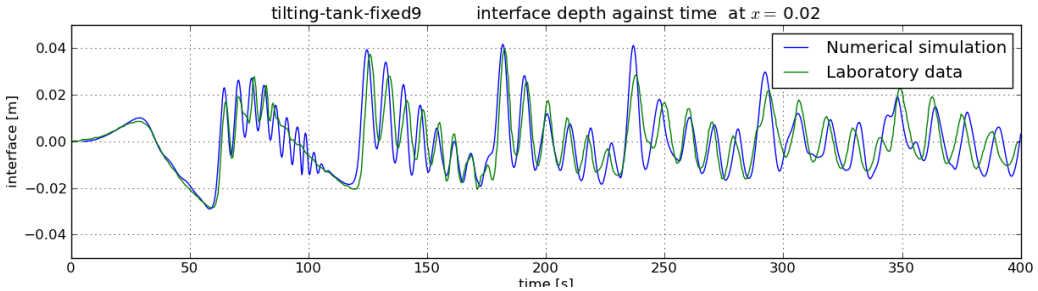


Figure 7.4: Evolution of the interface with time at $x = 0.02$ for the tilting tank test.

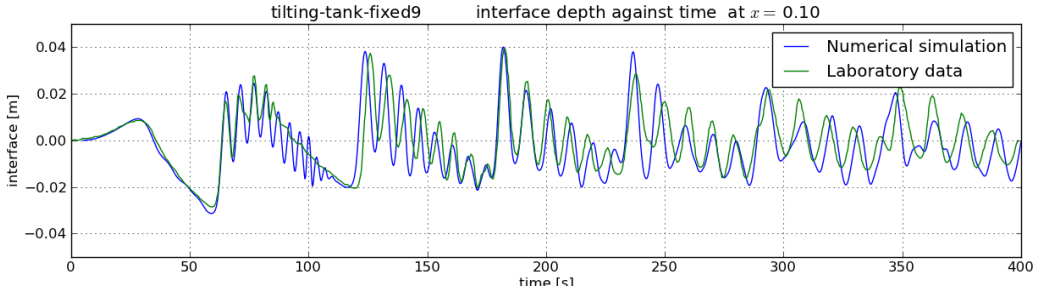


Figure 7.5: Evolution of the interface with time at $x = 0.1$ for the tilting tank test.

The numerical simulation is shifted to the right a small amount to account for the finite time taken to tilt the tank in the laboratory experiments.

Horn et al. (2001) measure the interface "near to" the centre of the tank ($x = 0.02\,\mathrm{m}$), but Figure 4 in that paper suggests that the ultrasonic probe measuring the interface depth could be as much as 0.1 m from the centre of the tank.

When measured at $x = 0.02\,\mathrm{m}$ we see no evidence for the emergence of the eighth soliton at approximately $t = 175\,\mathrm{s}$ in figure 7.4; but the eighth soliton *is* observed when the interface is measured at $x = 0.1\,\mathrm{m}$ in figure 7.5. However, the time at which the leading soliton passes $x = 0.1\,\mathrm{m}$ does seem to be a little ahead for the leftward travelling waves

(at approximately $t = 125\,\mathrm{s}$ and $t = 240\,\mathrm{s}$), but slightly behind for the rightward travelling waves (at approximately $t = 60\,\mathrm{s}$ and $t = 180\,\mathrm{s}$) which suggests that the probe is indeed closer to the centre of the tank than 0.1 m.

7.1.2.2 Adaptive mesh results

The adaptive mesh simulations were run on a single processor with a timestep of $\Delta t = 0.025\,\mathrm{s}$. Every 5 timesteps the mesh was adapted, absolute interpolation errors of 0.001 for u and w, and 0.0005 for perturbation density were used.

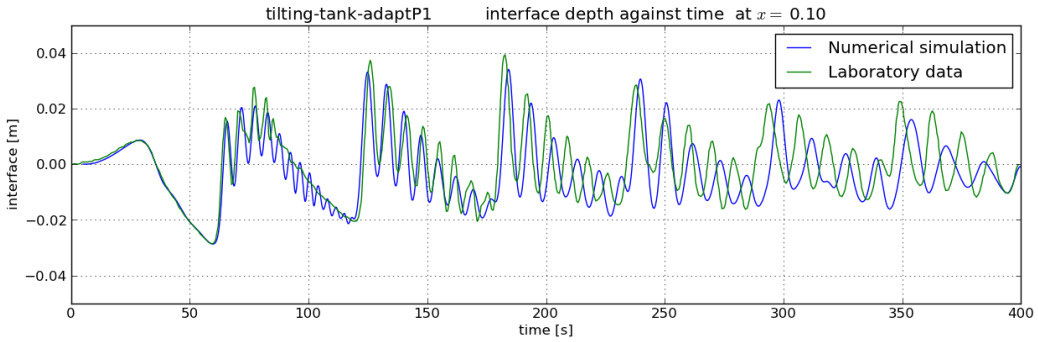


Figure 7.6: Evolution of the interface with time at $x = 0.1$ for the adaptive mesh simulation for the tilting tank test case.

Figure 7.6 shows how the interface at $x = 0.01\,\mathrm{m}$ evolves with time in the adaptive mesh simulation. The eighth soliton at approximately $t = 175\,\mathrm{s}$ is captured, though it is less pronounced than in the fixed mesh simulation. The wave is also slowing down, which is due to the thickening of the interface with time. The simulation time for this simulation was approximately 36 hours.

Figure 7.8 shows the perturbation density and mesh at various times during the simulation. At the start of the simulation, there are extra elements at the interface to resolve it (panel (a)).Later in the simulation, we can see that there is extra resolution at the top and bottom boundaries to resolve the no-slip boundary layers (panel (b) onwards).

The adaptive mesh simulation has been rerun with a smaller interpolation error for perturbation density of 0.0001 rather than 0.0005, and the same interpolation errors for u and w in an attempt to prevent the thickening of the interface and the slowing down of the wave. Figure 7.10 shows the evolution of the interface with time at $x = 0.1\,\mathrm{m}$.

The evolution of the interface in this case is more similar to the fixed mesh and lab-

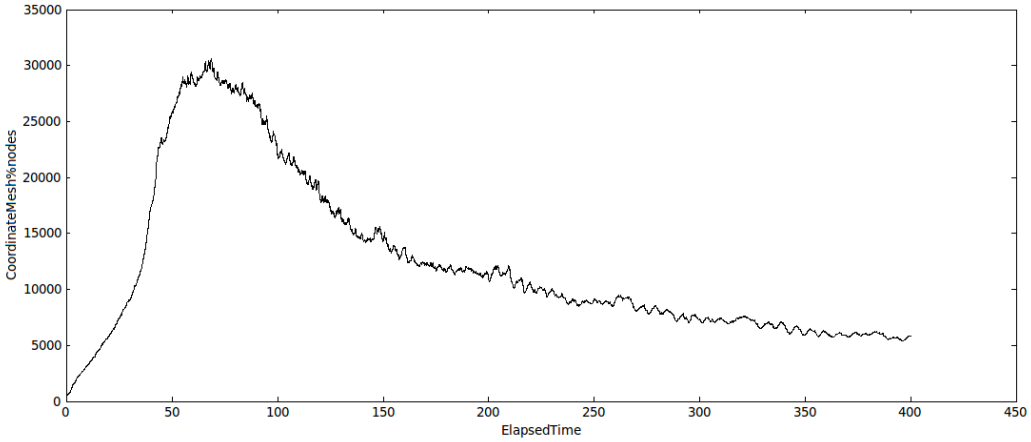


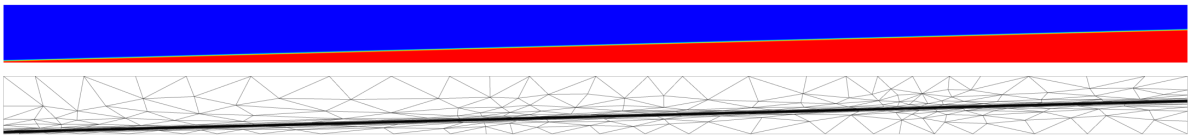
Figure 7.7: Number of nodes in mesh for the adaptive result against time.

oratory results than the adaptive mesh simulation with a larger interpolation error for perturbation density. The eighth soliton at approximately $t = 175\,\mathrm{s}$ is again well captured. The wave shows no sign of slowing down, but this comes at a cost. The number of nodes used in this simulation peaks at 120,000, compared to 30,000 for the adative mesh simulation with a larger interpolation error for perturbation density. The CPU time for this simulation was approximately 220 hours.

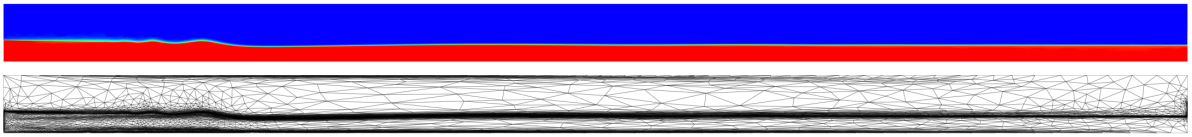
Van der Boon (2011) used Finlab (a successor to FINEL3D Labeur and Pietrzak (2004)) to simulate the degeneration of interfacial waves to solitary waves. The use of a turbulence closure model seems to accurately capture the correct solitary wave amplitude without having to incorporate sidewall friction in the model. It would be informative to run the simulation with an LES scheme to see the effect on the amplitude of the leading solitary wave.

7.1.2.3 Discussion

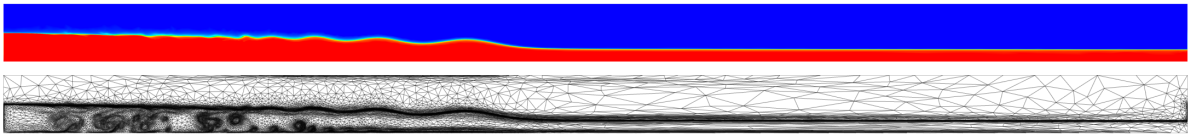
The results shown in 7.6 and 7.10 show that the adaptive mesh simulations can accurately capture the evolution of the interface with time, in a more computationally efficient manner than fixed mesh simulations. By decreasing the interpolation errors which inform the adaptive mesh algorithm, more resolution is used to represent the interface between the two layers, as well as the boundary layers, which leads to a better result. However, there is a trade off between putting in more resolution to capture the interface, and resources required. This can mean that several adaptive mesh simulations have to be performed



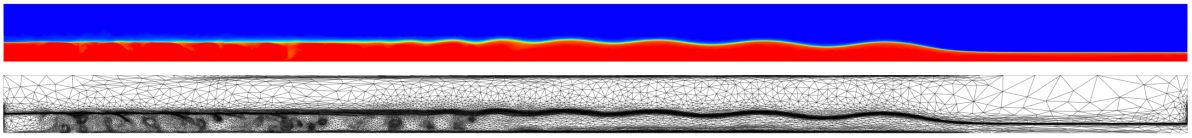
(a) Time 0 s



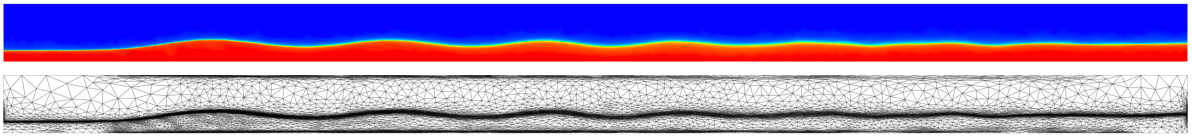
(b) Time 33 s



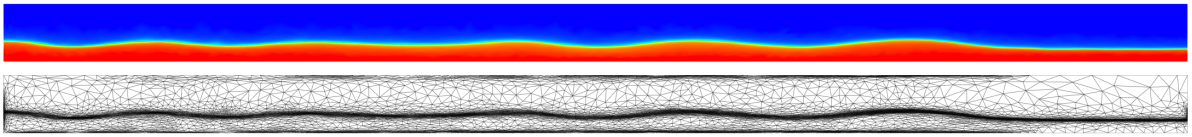
(c) Time 52 s



(d) Time 75 s



(e) Time 139 s



(f) Time 193 s

Figure 7.8: Density and adapted mesh at different times for the tilting tank test case. The times at which the images have been taken are chosen to compare to those in figure 7.9.

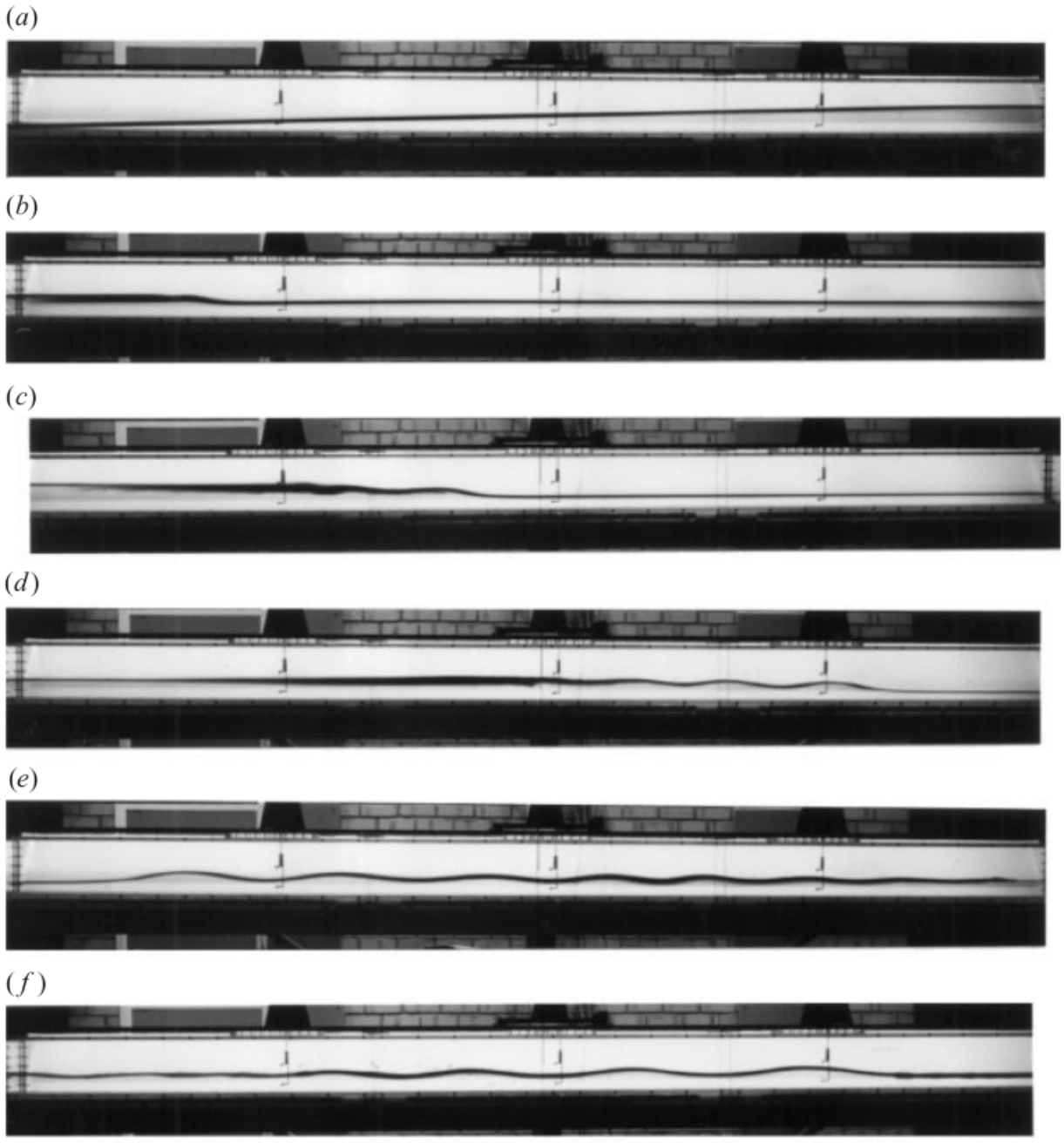


Figure 7.9: Density at various times taken from Horn et al. (2001). The caption in Horn et al. (2001) is "Photographs showing the steepening of an initial basin–scale wave to form a packet of solitons. The photographs show the whole 6 m of the tank. The evolving train of solitons is propagating from left to right in panels (b)–(d), from right to left in panel (e) and from left to right in panel (f)." Note the ultrasonic gauge close to the centre of the tank, which we estimate could be up to 0.1 m from the centre of the tank.

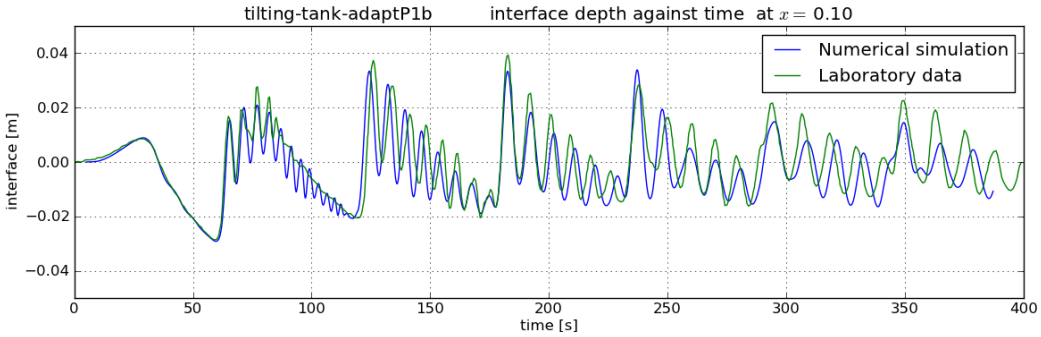


Figure 7.10: Evolution of the interface with time at $x = 0.1$ for the adaptive mesh simulation with smaller interpolation errors for the tilting tank test case.

before it is known whether the interface is being resolved sufficiently well.

The fixed mesh result took approximately 120 hours when run on 64 processors, while the adaptive mesh result with an interpolation error of 0.0005 for perturbation density took approximately 36 hours on a single processor. This represents more than a 200 fold increase in computational efficiency. For the adaptive mesh simulation with an interpolation of 0.0001 for perturbation density, which captured the eighth soliton as well as not showing any thickening of the interface and no slowing down of the wave, the increase in compuational efficiency was a factor of 35.

7.1.2.4 Conclusion

We have successfully simulated the degeneration of large–scale interfacial waves into solitary waves with both fixed and adaptive meshes. There is a large increase in computational efficiency when using adaptivity, to achieve a result that compares favourably with both high resolution fixed mesh results and with laboratory simulations.

7.2 Breaking

This section considers the shoaling and breaking of solitary waves at a slope and the subsequent energetics and mixing. First, a typical shoaling and breaking event is described, and the evolution of the kinetic energy, background and available potential energies and the energy lost through mixing are examined. Second, the effect of changing the interpolation error that guides the adaptivity is briefly examined. Third, the angle (and so also the length) of the slope are changed to see how this effects the breaking process. Finally, we combine the wave amplitude and slope into a single parameter, the Iribarren number, and calculate the reflectance of pseudoenergy (the sum of the kinetic and available potential energy) as a function of this parameter.

7.2.1 Dynamics of a shoaling and breaking event

As internal solitary waves in a quasi-two-layer stratification propagate towards a sloping bathymetry, they change their shape, as it is the relative depths of the two layers that determine their amplitude, wave lengthscale and phase speed. This process is called shoaling. The waves continue to change their shape and overturning can occur where the waves then break. This can result in an intense mixing event which can be crucially important for biology and climate. Figure 7.11 shows a time series of a typical shoaling and breaking event. The wave can be observed to have changed shape between panels (a) and (b). In (c), the wave has started to break, with some overturning of the isopycnals. In (d), an anti-clockwise circulation has developed (figure 7.12 shows the velocity vectors) which leads to intense mixing. This is the start of the mixing event and is when energy is irreversibly lost. This mixing event can be identified in figure 7.13 as the point which the energy lost through mixing starts to increase. The bolus that is generated continues to propagate up the slope with more entrainment of fluid and the generation of shear instabilities which promote further mixing (g) to (l). Later in the simulation, the wave is reflected back towards the left-hand side of the domain where the wave is once again reflected, this time with no mixing. This can be seen in the energy evolution at approximately 65 s where there is a local minimum in the kinetic energy.

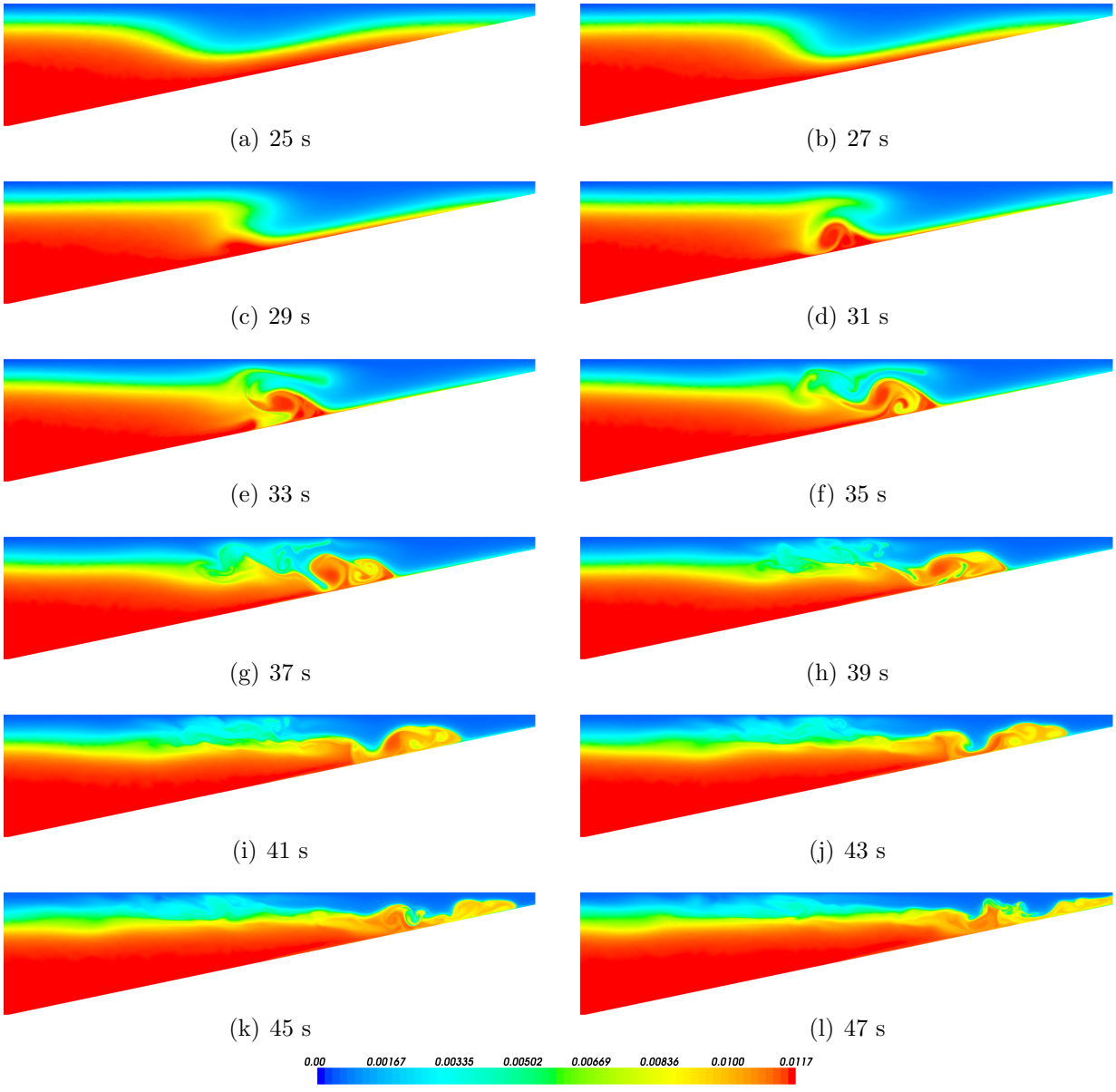


Figure 7.11: Density field, showing the shoaling and breaking of a solitary wave.

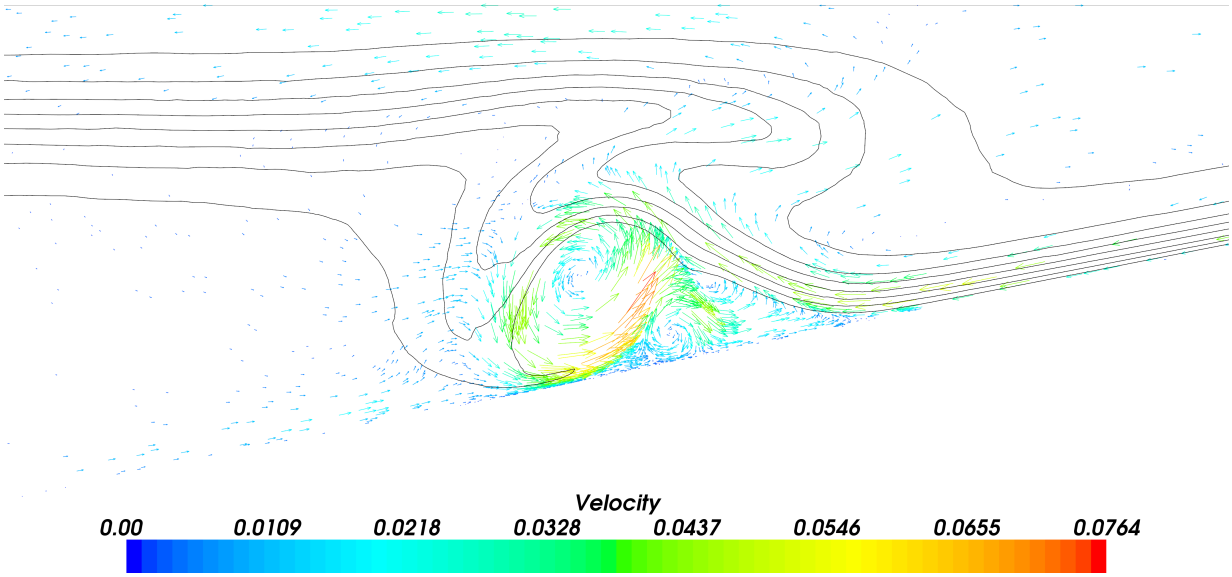


Figure 7.12: Velocity vectors and density contours at 31 s of simulated time in the shoaling breaking wave simulation. A relatively large scale anti–clockwise circulation can be seen to have developed, with a smaller scale clockwise secondary circulation close to the boundary.

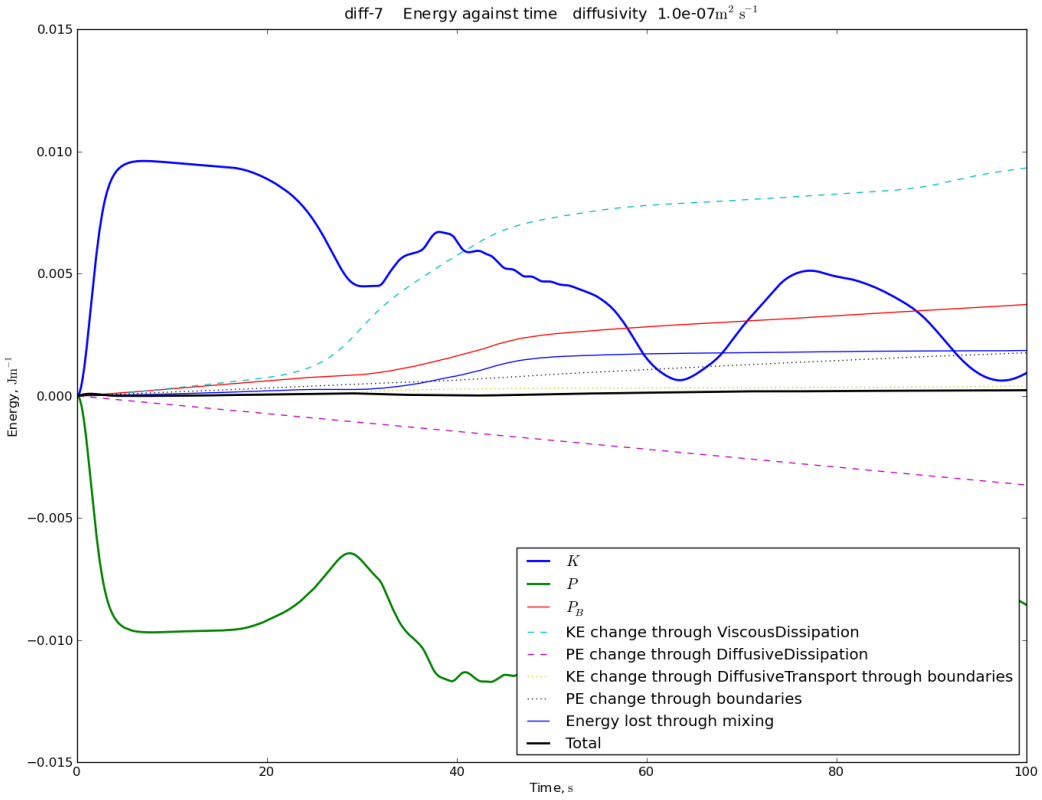


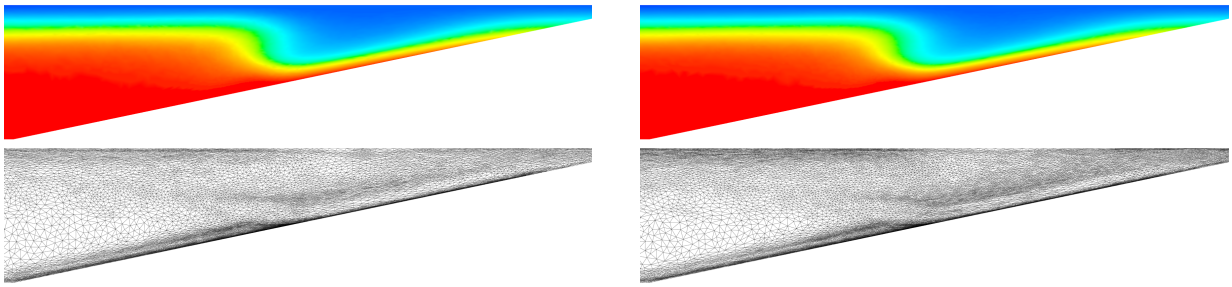
Figure 7.13: Evolution of the energy in the shoaling breaking wave simulation. Note the start of the mixing event at approximately 30 s, where the energy lost through mixing starts to increase. The wave is reflected at the left-hand boundary of the domain at approximately 60 s, where there is a local minimum in the kinetic energy.

7.2.2 Adaptive mesh results with different interpolation errors

The simulations described in the previous section were run with a relative interpolation error for perturbation density of 2%. To check for mesh convergence, the effect of running with a smaller interpolation error of 1% is now briefly investigated. These simulations are run with a diffusivity of $\kappa = 10^{-7}\,\mathrm{m^2\,s^{-1}}$.

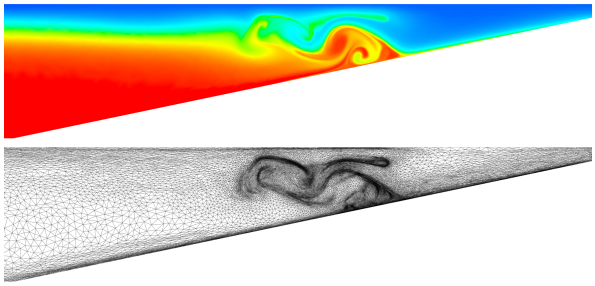
Figure 7.14 shows the perturbation density fields at various times for two simulations run with different interpolation errors for perturbation density. It can be seen that more nodes are used in the simulation with a smaller interpolation error (right hand panels in figure 7.14), particularly later on in the simulation after the wave has broken and the mixing has started (lower panels of 7.14). While more structure can be seen in the images that used higher resolution, qualitatively the results look extremely similar indicating that a reasonable degree of mesh convergence has been attained.

The minimum edge lengths in the simulation are approximately 0.1 mm. If this simulation was to be run on a fixed mesh with uniform resolution with mesh spacing of 0.1 mm, it would require approximately 27 million nodes and 54 million elements, which is prohibitively large.

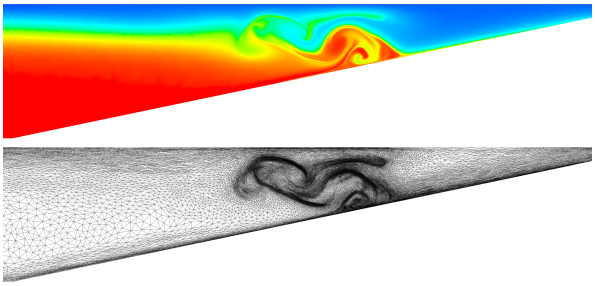


(a) Time 28s. 2% interpolation error. 15,852 nodes.

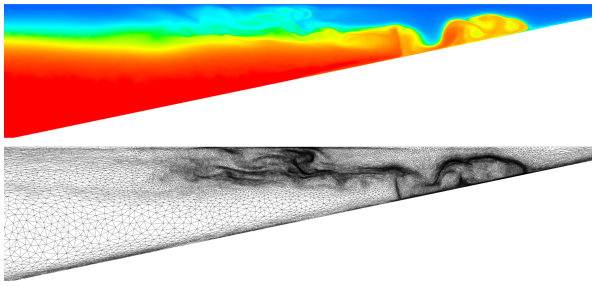
(b) Time 28s. 1% interpolation error. 20,425 nodes.



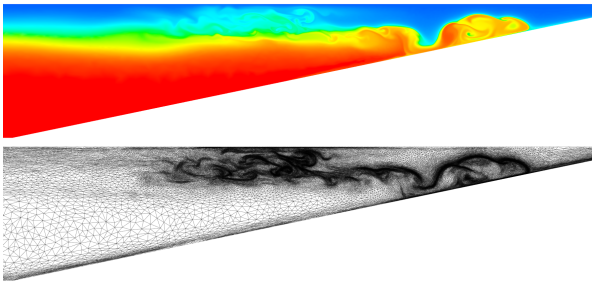
(c) Time 35s. 2% interpolation error. 30,294 nodes.



(d) Time 35s. 1% interpolation error. 41,154 nodes.



(e) Time 42s. 2% interpolation error. 45,955 nodes.



(f) Time 42s. 1% interpolation error. 81,993 nodes.

Figure 7.14: Perturbation density and meshes for different adaptivity options at various times for the shoaling breaking wave problem.

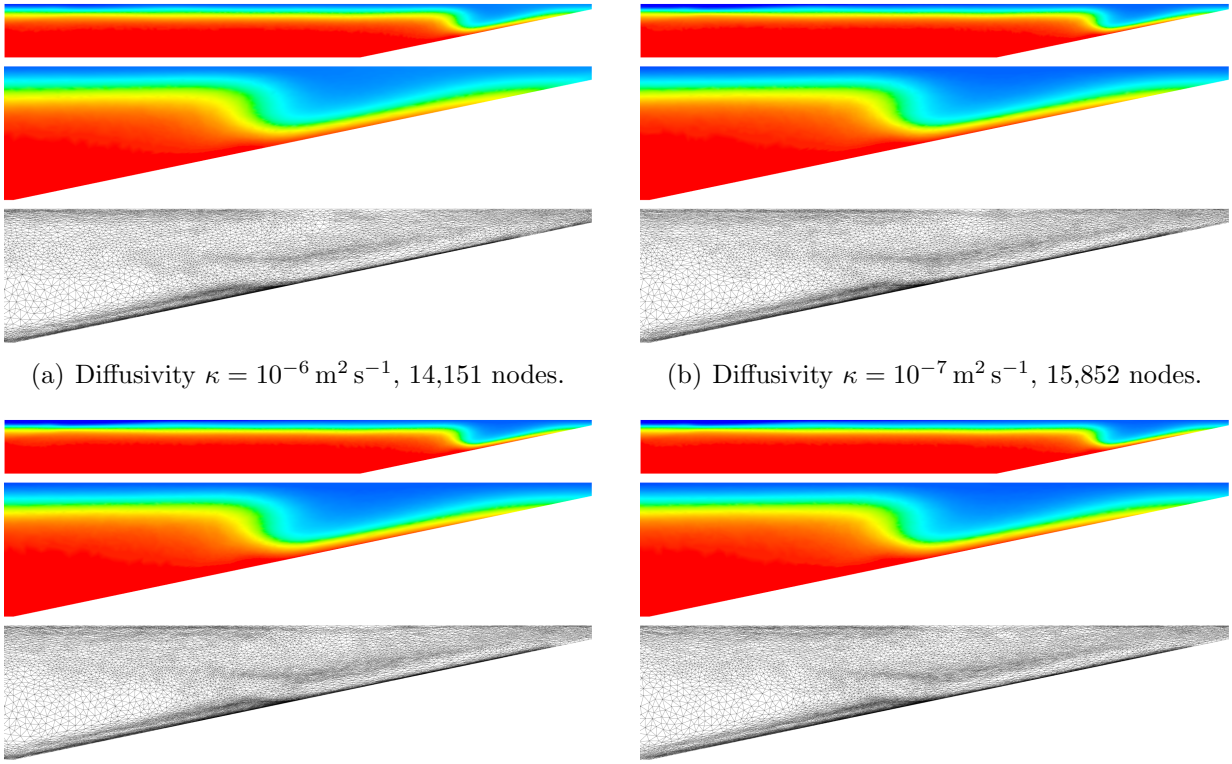
7.2.3 The effect of diffusivity

Four simulations have been performed to investigate the effect of diffusivity for shoaling and breaking of solitary waves at a slope. The values considered are zero explicit diffusivity and diffusivities of $\nu = 10^{-6}, 10^{-7}$, and $10^{-8}\,\mathrm{m^2\,s^{-1}}$.

In all the simulations the wave has shoaled after approximately 28 seconds (figure 7.15) at which time they all look qualitatively similar. After 35 seconds (figure 7.16) the simulations with diffusivities of zero, 10^{-7}, and $10^{-8}\,\mathrm{m^2\,s^{-1}}$ again look qualitatively very similar. However, for the simulation with a diffusivity of $10^{-6}\,\mathrm{m^2\,s^{-1}}$, the pycnocline has thickened appreciably and the overturned fluid exhibits a flatter front as it propagates up the slope. At 42 seconds (figure 7.17), the front has propagated the same distance up the slope in all cases. However, the structure of the overturned fluids differs significantly with less detail being shown as the diffusivity is increased.

The simulations with smaller diffusivities have extra resolution in the meshes after 35 seconds, but not after 28 seconds. The more diffuse simulation diffuses away density gradients and so the adaptive mesh algorithm, which puts in resolution based on the derivatives of the field, does not increase the resolution. For the simulations with smaller diffusivity, the density gradients are not diffused away and extra resolution is put in to resolve them. Consequently more fine-scale structure is seen in the solutions at later times.

Figure 7.18 shows plots of energy against time for the simulations of four different diffusivities. The kinetic energy in each case evolves in a similar fashion as well as the viscous dissipation. However, the potential energy shows a general increase for the simulation with diffusivity $10^{-6}\mathrm{m^2\,s^{-1}}$. This is because the background potential energy is increasing due to diffusion of the background stratification more than the increase caused by mixing. As we decrease the diffusivity (figures b and c) the background potential energy converges on the energy lost through mixing, because less energy is lost through vertical diffusion. For the simulation with zero explicit diffusivity, the change in background potential energy is the same as the energy loss through mixing. In each case the total energy increases slightly due to numerical effects and the total energy loss through mixing is the same for each case, which would suggest that diffusion has an effect on the smaller scale dynamics but not on the overall energy budget.



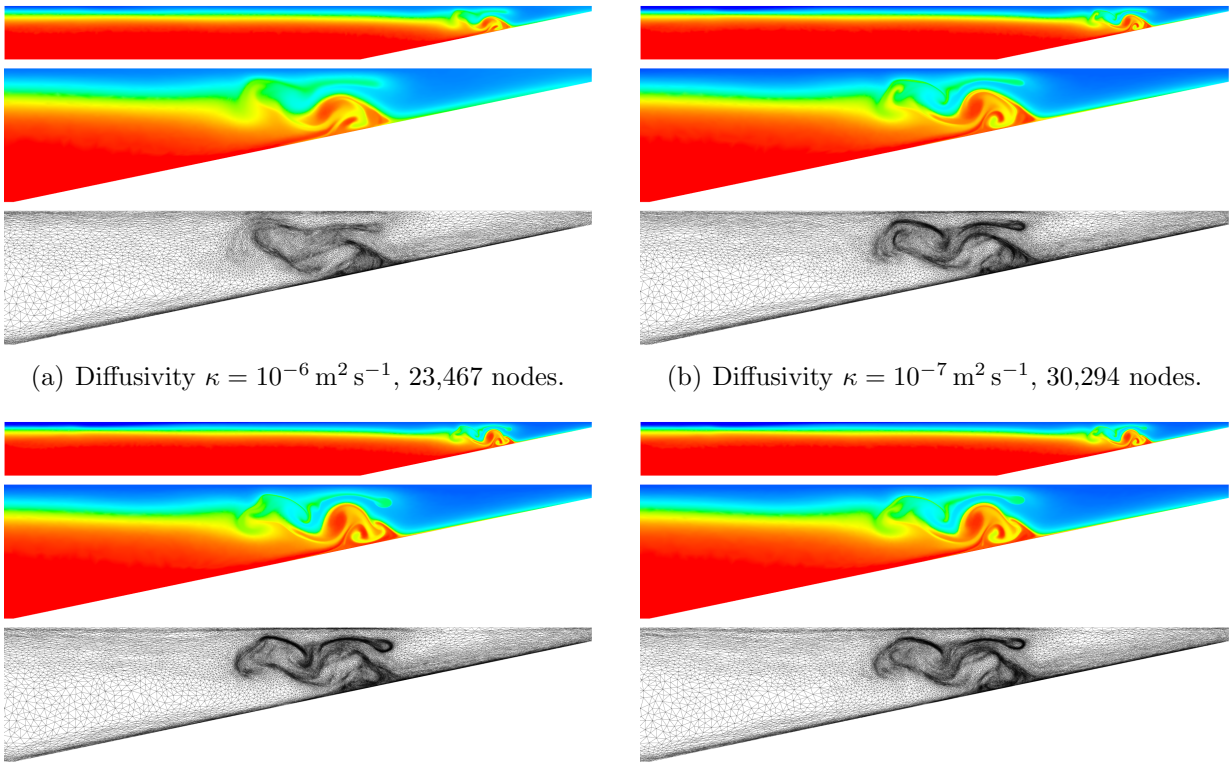
(a) Diffusivity $\kappa = 10^{-6}\,\mathrm{m}^2\,\mathrm{s}^{-1}$, 14,151 nodes.

(b) Diffusivity $\kappa = 10^{-7}\,\mathrm{m}^2\,\mathrm{s}^{-1}$, 15,852 nodes.

(c) Diffusivity $\kappa = 10^{-8}\,\mathrm{m}^2\,\mathrm{s}^{-1}$, 16,832 nodes.

(d) Diffusivity $\kappa = 0\,\mathrm{m}^2\,\mathrm{s}^{-1}$, 17,163 nodes.

Figure 7.15: Perturbation density (including a zoom of the shoaling region) and adaptive mesh for different diffusivities after 28 seconds in the shoaling breaking wave problem.



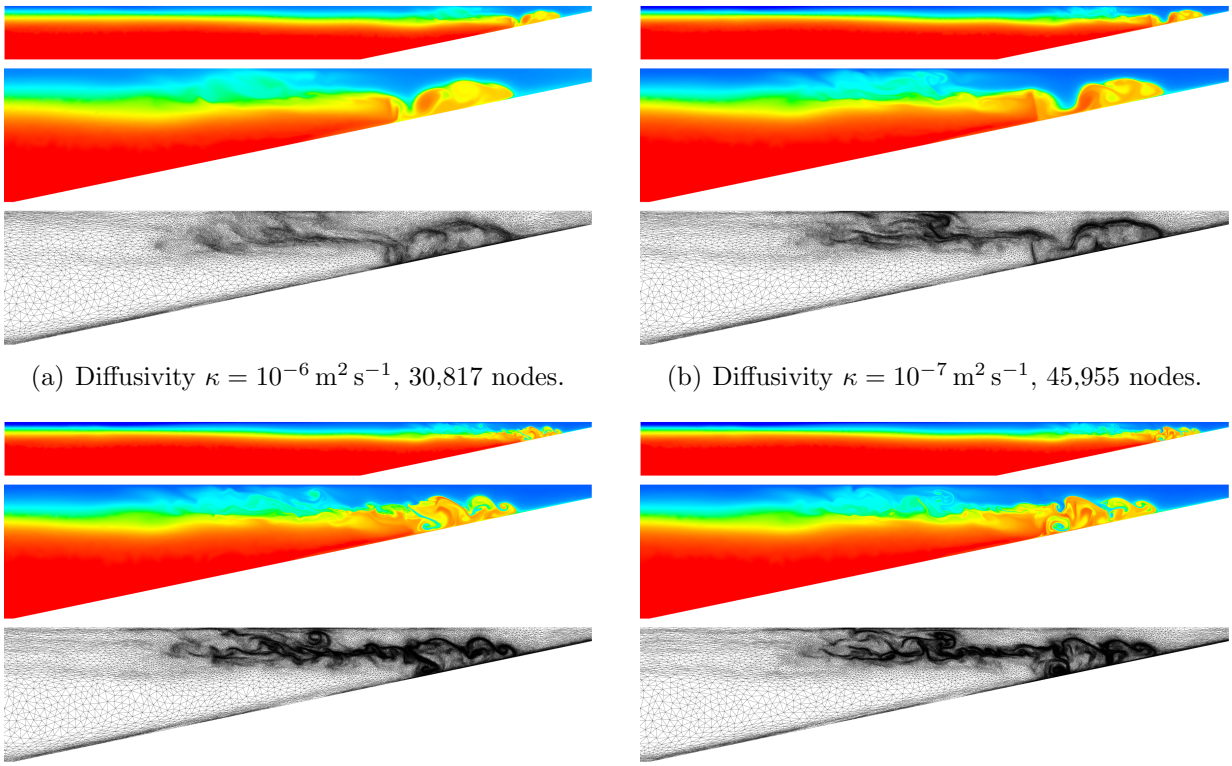
(a) Diffusivity $\kappa = 10^{-6}\,\mathrm{m}^2\,\mathrm{s}^{-1}$, 23,467 nodes.

(b) Diffusivity $\kappa = 10^{-7}\,\mathrm{m}^2\,\mathrm{s}^{-1}$, 30,294 nodes.

(c) Diffusivity $\kappa = 10^{-8}\,\mathrm{m}^2\,\mathrm{s}^{-1}$, 34,034 nodes.

(d) Diffusivity $\kappa = 0\,\mathrm{m}^2\,\mathrm{s}^{-1}$, 35,668 nodes.

Figure 7.16: Perturbation density (including a zoom of the shoaling region) and adaptive mesh for different diffusivities after 35 seconds in the shoaling breaking wave problem.



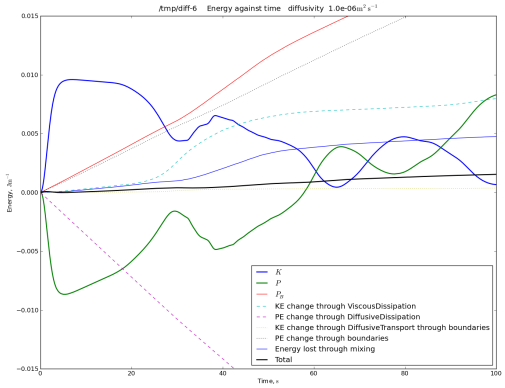
(a) Diffusivity $\kappa = 10^{-6}\,\mathrm{m}^2\,\mathrm{s}^{-1}$, 30,817 nodes.

(b) Diffusivity $\kappa = 10^{-7}\,\mathrm{m}^2\,\mathrm{s}^{-1}$, 45,955 nodes.

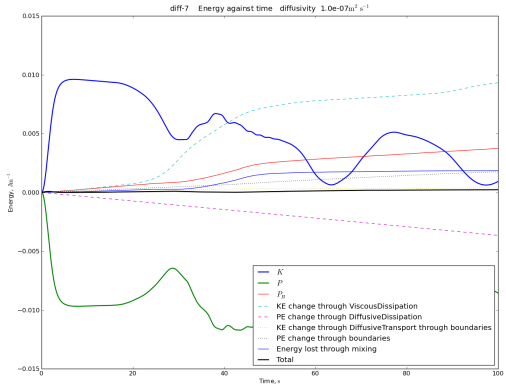
(c) Diffusivity $\kappa = 10^{-8}\,\mathrm{m}^2\,\mathrm{s}^{-1}$, 92,587 nodes.

(d) Diffusivity $\kappa = 0\,\mathrm{m}^2\,\mathrm{s}^{-1}$, 103,134 nodes.

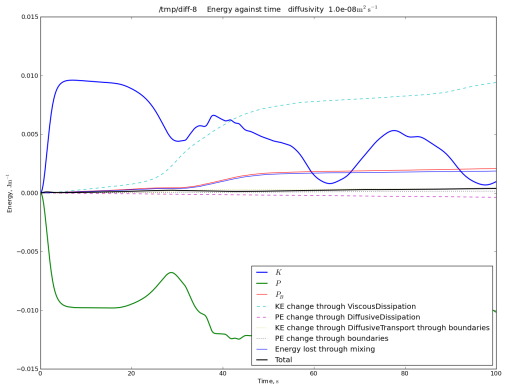
Figure 7.17: Perturbation density (including a zoom of the shoaling region) and adaptive mesh for different diffusivities after 42 seconds in the shoaling breaking wave problem.



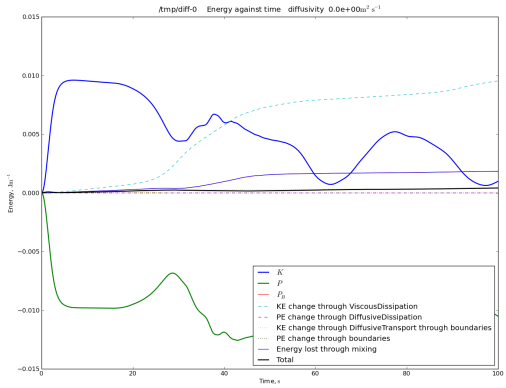
(a) Diffusivity $\kappa = 10^{-6}\,\mathrm{m}^2\,\mathrm{s}^{-1}$



(b) Diffusivity $\kappa = 10^{-7}\,\mathrm{m}^2\,\mathrm{s}^{-1}$



(c) Diffusivity $\kappa = 10^{-8}\,\mathrm{m}^2\,\mathrm{s}^{-1}$



(d) Diffusivity $\kappa = 0.0\mathrm{m}^2\,\mathrm{s}^{-1}$

Figure 7.18: Plots of energy against time for different diffusivities in the shoaling breaking wave problem. Energy lost through mixing is similar for each case except for that with a diffusivity of $\kappa = 10^{-6}\,\mathrm{m}^2\,\mathrm{s}^{-1}$.

7.2.4 The effect of the angle of the slope on shoaling and breaking

A series of simulations have been performed with different slope lengths. Table 7.2.4 lists the simulation names, the length of the slope (L_s) and the corresponding slopes (s) and angles in degrees. All of these simulations are carried out with a diffusivity of $10^{-7}\mathrm{m}^2\,\mathrm{s}^{-1}$ and wave amplitude of 31 mm.

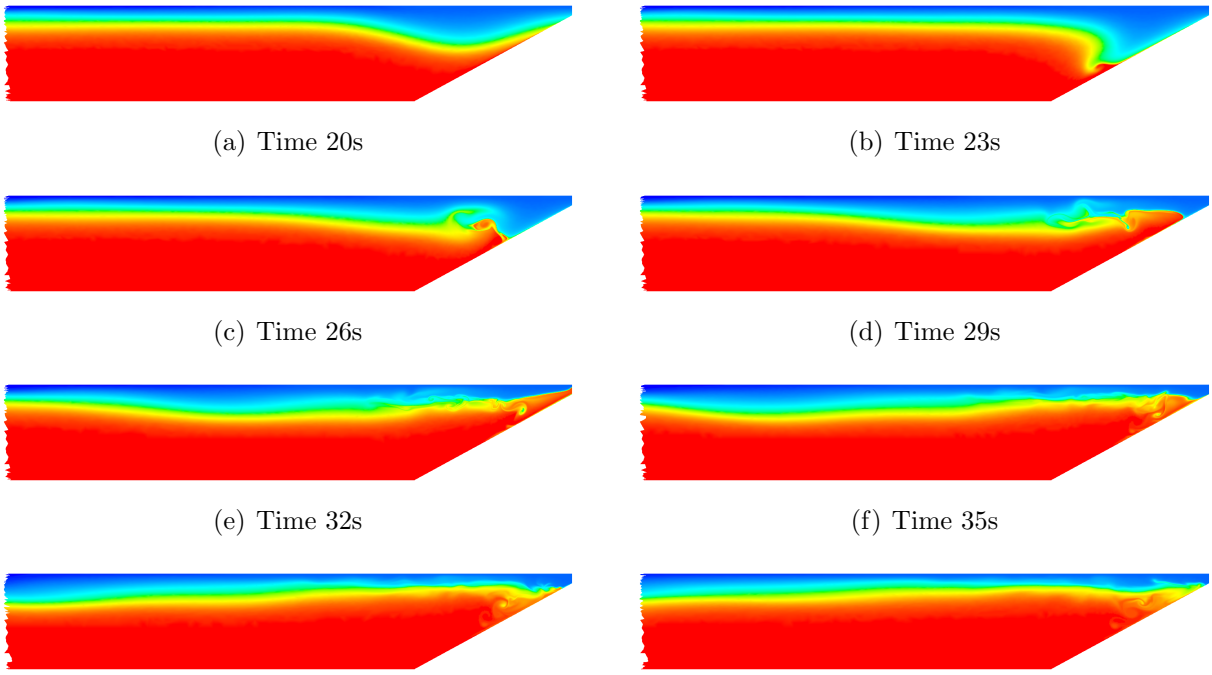
simulation name	L_s, mm	slope, degrees	s	$\kappa, \mathrm{m}^2\,\mathrm{s}^{-1}$	a, mm
slope0027	27	78.7	5.0	10^{-7}	31
slope0060	60	66.0	2.25	10^{-7}	31
slope0100	100	53.5	1.35	10^{-7}	31
slope0135	135	45.0	1.0	10^{-7}	31
slope0200	200	34.0	0.675	10^{-7}	31
slope0250	250	28.4	0.54	10^{-7}	31
slope0350	350	21.1	0.386	10^{-7}	31
slope0450	450	16.7	0.3	10^{-7}	31
slope0550	550	13.8	0.246	10^{-7}	31
slope0650	650	11.7	0.208	10^{-7}	31
slope0750	750	10.2	0.18	10^{-7}	31
slope0900	900	8.5	0.15	10^{-7}	31
slope1000	1000	7.7	0.135	10^{-7}	31
slope1350	1350	5.7	0.1	10^{-7}	31
slope1500	1500	5.1	0.09	10^{-7}	31
slope1800	1800	4.3	0.075	10^{-7}	31
slope3000	3000	2.6	0.045	10^{-7}	31

Table 7.1: Table of parameters used in the simulations examining the effect of the angle of the slope on shoaling and breaking. The simulation names shown in bold are those simulations which are examined in more detail.

Figure 7.19 shows perturbation density at various times in the simulation with a slope length of 250 mm. The wave exhibits steepening, but there is little overturning and a comparatively small amount of energy is lost through mixing, panel (a) of figure 7.2.4.

Figure 7.20 shows perturbation density at various times in the simulation with a slope length of 450 mm. As the wave breaks at the slope, there is overturning and energy is lost through mixing, panel (b) of figure 7.2.4.

Figure 7.21 shows perturbation density at various times in the simulation with a slope length of 900 mm. The wave overturns and an anti–clockwise circulation develops. This travels along the slope and some shear instabilities develop. The mixing is more intense than that in simulations slope0250 and slope0450, which can be seen in the amount of energy lost through mixing, panel (c) of figure 7.2.4.



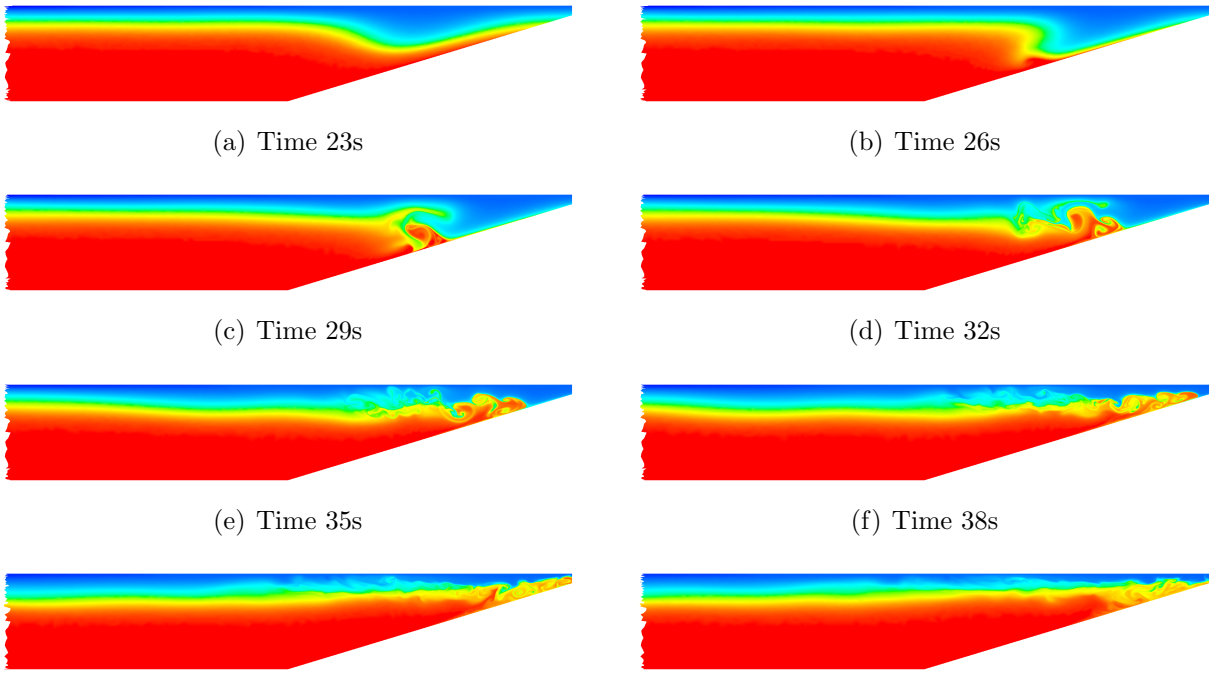
(a) Time 20s (b) Time 23s

(c) Time 26s (d) Time 29s

(e) Time 32s (f) Time 35s

(g) Time 38s (h) Time 41s

Figure 7.19: Perturbation density at different times for slope 0.54, simulation 'slope0250'. Diffusivity is set to $\kappa = 10^{-7}\,\mathrm{m^2\,s^{-1}}$.



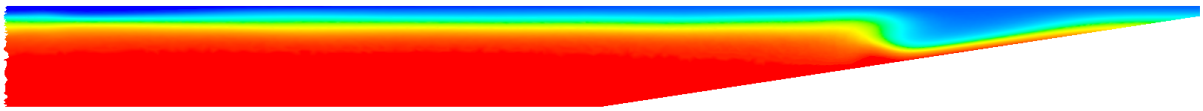
(a) Time 23s (b) Time 26s

(c) Time 29s (d) Time 32s

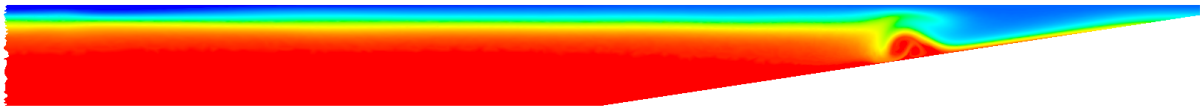
(e) Time 35s (f) Time 38s

(g) Time 41s (h) Time 44s

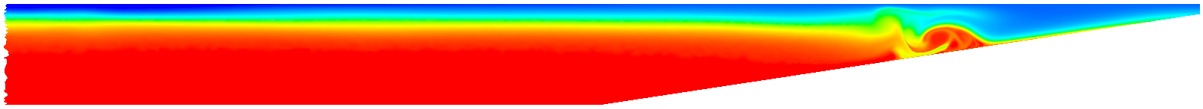
Figure 7.20: Perturbation density at different times for slope 0.3, simulation 'slope0450'. Diffusivity is set to $\kappa = 10^{-7}\,\mathrm{m^2\,s^{-1}}$.



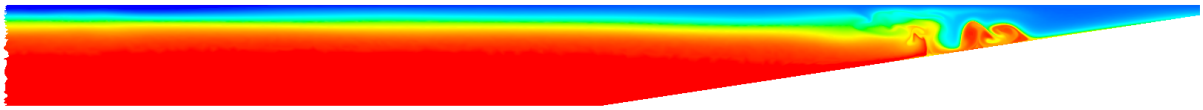
(a) Time 32s



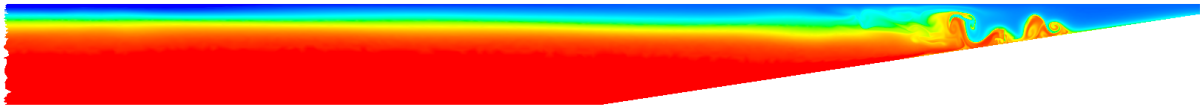
(b) Time 35s



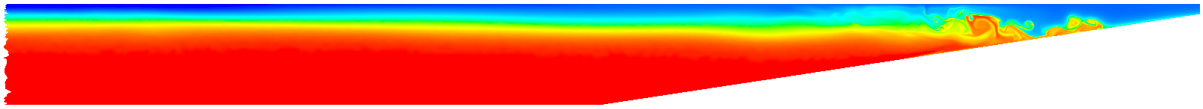
(c) Time 38s



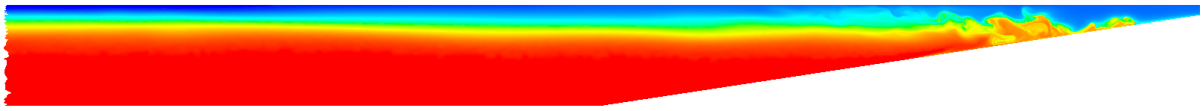
(d) Time 41s



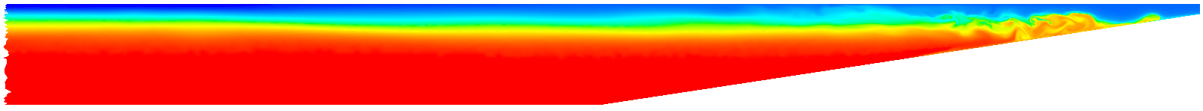
(e) Time 44s



(f) Time 47s



(g) Time 50s



(h) Time 53s

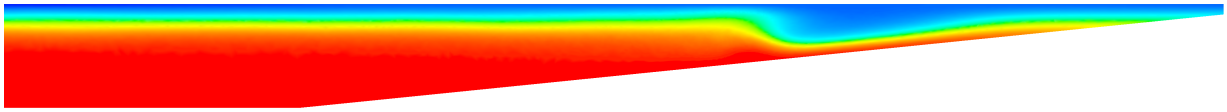
Figure 7.21: Perturbation density at different times for slope 0.15, simulation 'slope0900'. Diffusivity is set to $\kappa = 10^{-7}\,\mathrm{m^2\,s^{-1}}$.

Figure 7.22 shows perturbation density at various times in the simulation with a slope length of 1350 mm. Again, the wave overturns and develops shear instabilities as it travels up the slope. Panel (d) of figure 7.2.4 shows the energy evolution in this case. More (kinetic) energy is lost through viscous dissipation in this case.

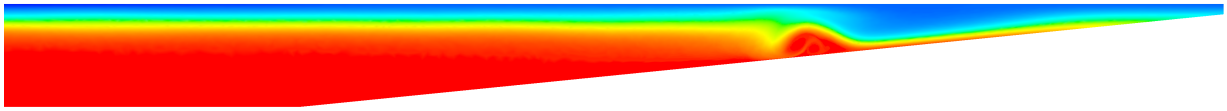
Figure 7.23 shows perturbation density at various times in the simulation with a slope length of 3000 mm. In this case, there is no overturning and the soliton degenerates into a group of solitary waves. The energy evolution for this case is not included in figure 7.2.4.

Figure 7.2.4 shows how the various energies in the system evolve with time, for four different slopes. The total energy (bold black line) remains approximately constant. The energy lost through viscous dissipation (dashed blue line), is greater for longer slopes, as a result of dissipation in the viscous boundary layer, which is longer for longer slopes.

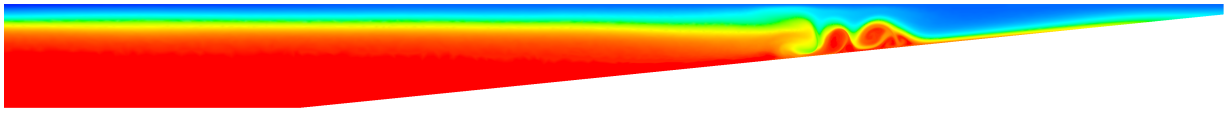
The change in potential energy through diffusive dissipation is due to the thickening of the interface with time, and it can be seen that the longer the slope, the greater this is, because the length of the interface is larger.



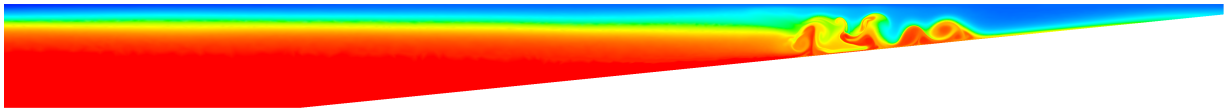
(a) Time 38s



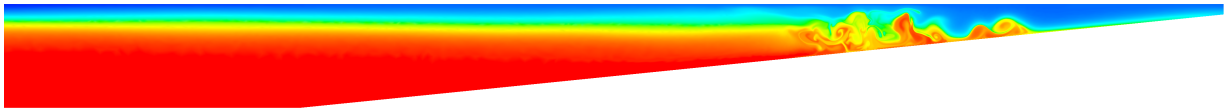
(b) Time 42s



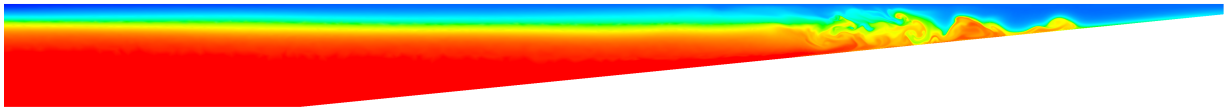
(c) Time 46s



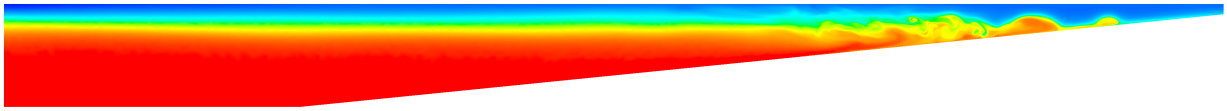
(d) Time 50s



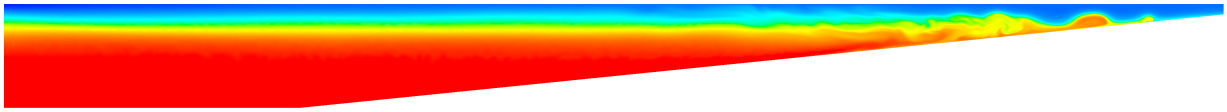
(e) Time 54s



(f) Time 58s

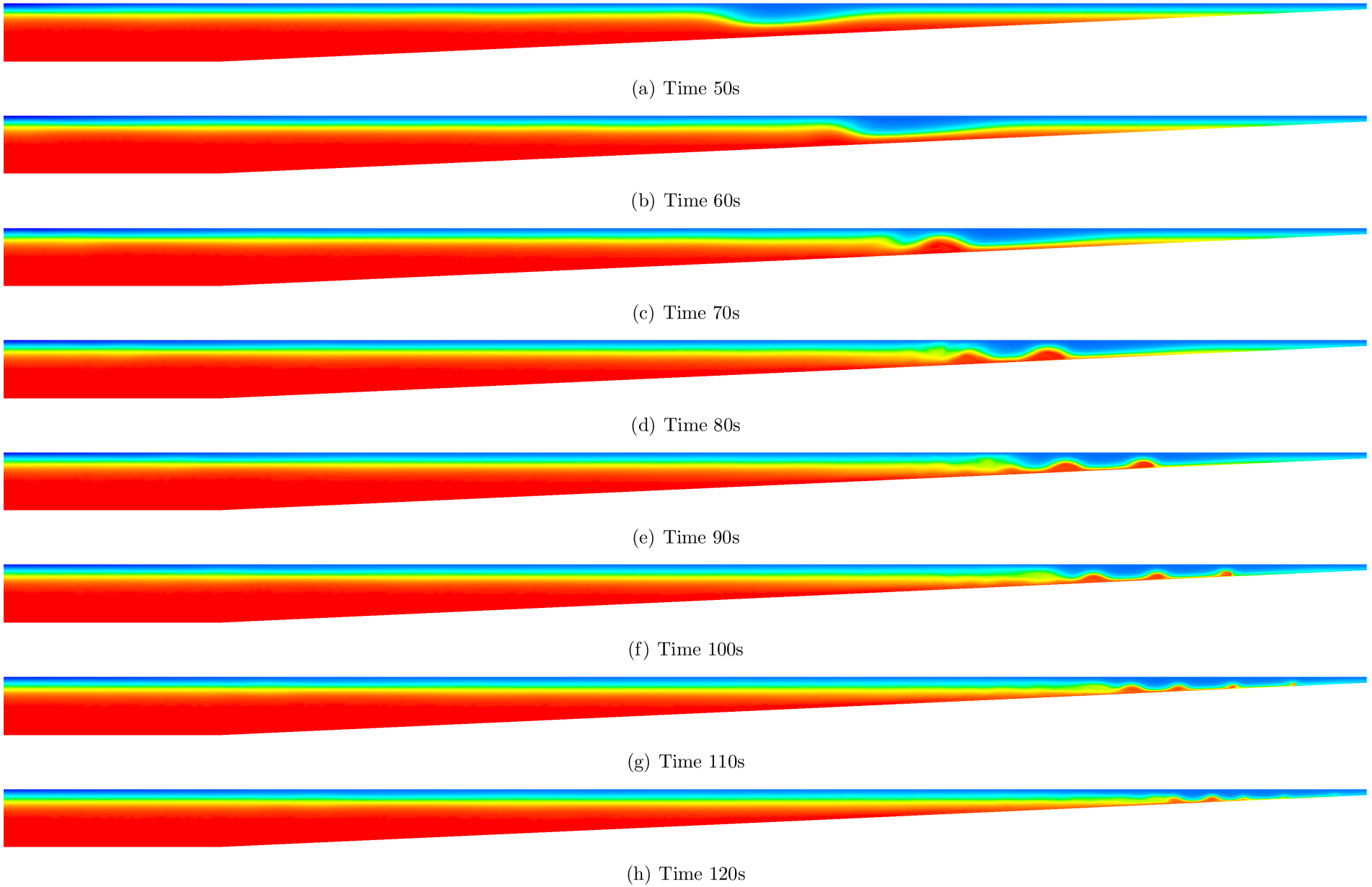


(g) Time 62s



(h) Time 66s

Figure 7.22: Perturbation density at different times for slope 0.1, simulation 'slope1350'. Diffusivity is set to $\kappa = 10^{-7}\,\mathrm{m^2\,s^{-1}}$.



(a) Time 50s

(b) Time 60s

(c) Time 70s

(d) Time 80s

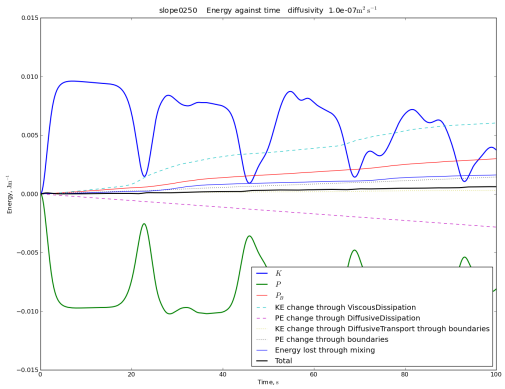
(e) Time 90s

(f) Time 100s

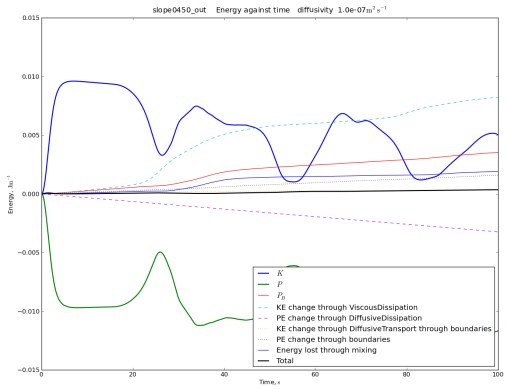
(g) Time 110s

(h) Time 120s

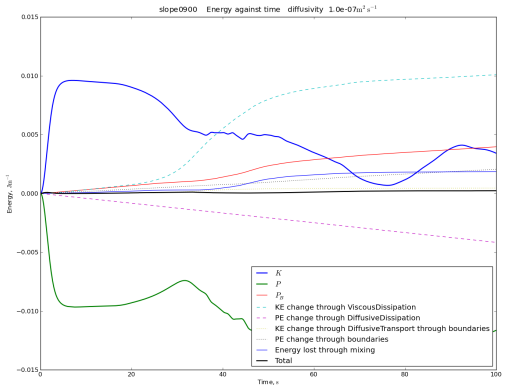
Figure 7.23: Perturbation density at different times for slope 0.045, simulation 'slope3000'. Diffusivity is set to $\kappa = 10^{-7}\,\mathrm{m^2\,s^{-1}}$.



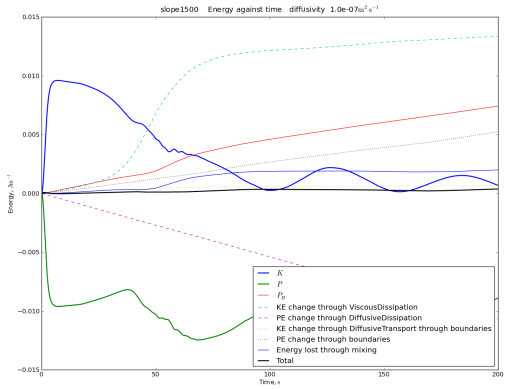
(a) Slope 0.54



(b) Slope 0.30



(c) Slope 0.15



(d) Slope 0.1

Figure 7.24: Plots of energy against time for different slopes. Diffusivity is set to $\kappa = 10^{-7}\,\mathrm{m}^2\,\mathrm{s}^{-1}$.

7.2.5 Reflectance of pseudoenergy

The Iribarren number is defined as

$$\xi = \frac{s}{|a/L_w|^{1/2}}, \tag{7.1}$$

where s is the slope, and a and L_w are the amplitude and the wavelength of the shoaling wave respectively. This dimensionless number, also known as a 'surf similarity parameter', was originally developed to classify surface waves breaking at the shore, but Boegman et al. (2005) found it also applied to internal solitary wave breaking at a slope.

The sum of the kinetic and available potential energies is the pseudoenergy. The energy reflectance is the ratio of reflected to incident pseudoenergy flux, and this is calculated for a series of simulations with wave amplitudes of 21, 26, 31, 36 and 41 mm, and slope lengths of 250, 450, 650, 900 and 1350 mm.

The results are shown in figure 7.25, along with an exponential function of the form

$$R = 1 - e^{\xi/\xi_0}, \tag{7.2}$$

as suggested by Bourgault and Kelley (2007).

The good fit of the simulated reflectances to the functional indicates that the numerical model has accurately captured the dynamics of the wave breaking at the slope, and that the analysis of the energetics of the wave breaking process is robust.

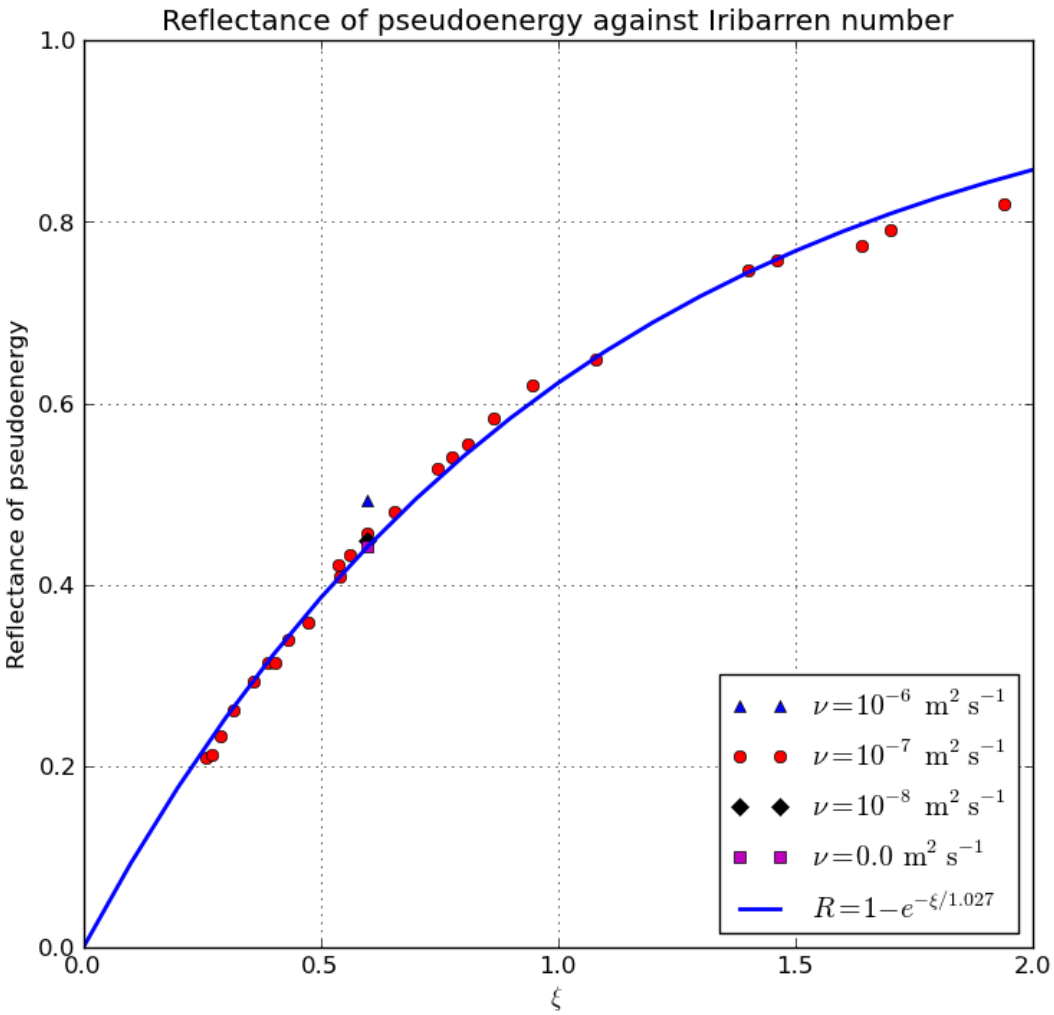


Figure 7.25: Reflectance of pseudoenergy as a function of Iribarren number.

7.3 Conclusions

The generation of internal waves in a two–layer fluid has been studied with Fluidity–ICOM. Two test cases for the generation of internal waves in a two-layer fluid were examined: internal lee wave generation by flow over a topographic bump; and the degeneration of large–scale interfacial waves into solitary waves in a tilting tank. In the case of flow over a topographic bump the wavelength of the lee wave that was generated compared favourably to both analytical and laboratory results. However, further work is needed to accurately model the amplitude of the lee wave. The solitary waves generated in the tilting tank test case were well modelled with Fluidity–ICOM, both in high resolution fixed mesh simulations and adaptive mesh simulations, with the latter results capturing the main dynamics of the flow with between 35 and 200–fold increase in computational efficiency.

The breaking of internal solitary waves at a slope has also been studied with Fluidity–ICOM. A typical wave breaking event has been described, along with the evolution of an energy budget with time, which allowed the amount of energy lost as a result of diapycnal mixing to be quantified. Two simulations with different user-defined interpolation errors specified for perturbation density have illustrated how the adaptive mesh capability of Fluidity–ICOM focuses resolution in (user–guided) regions of interest and dynamical features. In the case considered here this naturally results in the focusing in of computational effort on the overturning of isopycnals and areas of diapycnal mixing. The good qualitative comparison between the dynamical features of the two simulations indicate that a reasonable degree of mesh convergence has been achieved. More simulations would have to be performed to make a more quantitative statement about convergence to a solution with ever decreasing interpolations errors, but this would require an appropriate measure of, for instance, typical mesh spacing, which is quite tricky for an unstructured adaptive mesh.

The effect of diffusivity on the dynamics of the internal solitary wave breaking and the evolution of the energy budget has also been investigated. It has been found that diffusivity has an impact on the smaller scale dynamics, as expected, but not on the amount of energy lost as a result of diapycnal mixing. Changing the length of the slope

at which internal solitary waves break changes the subsequent dynamics of the wave as well as the energy budget. Internal solitary waves interacting at longer slopes did not break, but degenerated into a series of solitary waves as they propagated upslope, with more energy being lost through viscous dissipation. For shorter, steeper slopes, the internal solitary wave showed steepening, but little overturning and less energy was lost through mixing. Finally, simulations with both different wave amplitude and slope length have been performed and the reflectance of pseudoenergy (the sum of kinetic and available potential energies) at the slope calculated. This can be expressed as a function of of the Iribarren number, a non-dimensional quantity that takes into account both the slope of the wave $\frac{a}{L_w}$ and the slope of the geometry s. The good fit between the calculated reflectances and the functional dependence of reflectance on the Iribarren number indicates that the energetic analysis and the numerical simulations are robust.

The evolution of a steady propagating internal solitary wave towards a slope, to a breaking wave with intense vertical mixing highlights the large range of scales that occur in a typical internal wave breaking event. Traditional fixed mesh models would require a huge amount of computational resources to be able to accurately model this problem, and the benefit of having a multi-scale dynamically adaptive unstructured mesh model is apparent.

Fluidity–ICOM has been shown to be an effective tool in modelling the generation and breaking of internal waves in a two-layer fluid. The adaptive mesh capability of the model has captured the complex dynamics of the wave breaking process, which would have demanded a huge amount of computational resource when modelled with a traditional fixed-mesh model.

Chapter 8

Conclusions

Advances have been made in internal wave modelling with a next generation ocean model. The key feature of this model is the ability to adapt the mesh to capture evolving fluid dynamics. Internal waves are a globally significant feature of the world's oceans. In particular, internal wave breaking at a slope is responsible for a large vertical energy flux, and the range of lengthscales involved in the time-dependent process of wave breaking calls for an adaptive mesh model to evolve with time to simulate the dynamics in an efficient manner.

The results of the numerical model presented in this thesis were generated in order to test the efficacy of the Fluidity–ICOM model in the simulation of internal gravity waves. Internal waves have been simulated with other numerical models before, some with quad-tree based (structured mesh) refinement to capture the smaller scale dynamics, but never before have internal waves been simulated with an unstructured model utilising dynamic mesh adaptivity.

The generation, propagation and breaking of internal waves have been studied in both linearly stratified and two–layer fluids with Fluidity–ICOM. The fully unstructured adaptive mesh capability of Fluidity–ICOM is a unique feature in the computational oceanography community, which lends itself to efficiently modelling the complex dynamics that arise when internal waves break at a slope.

A series of test cases were investigated to examine the utility of Fluidity–ICOM in the study of internal waves. Fixed mesh simulations considered included the generation of

internal wave beams in a linearly stratified fluid due to an oscillating cylinder represented by a vertical momentum source and the propagation of internal waves in a linearly stratified fluid to demonstrate model convergence, which was found to be correct at second order as expected.

Simulations of the breaking of internal waves in a linearly stratified fluid at slopes showed that while adaptive mesh simulations are more computationally efficient, they are not always perfect and it can take time to optimally tune the parameters that guide the coarsening and refining of the mesh for a given problem.

The adaptive mesh capability of Fluidity–ICOM was incorporated with a view to producing a multi-scale ocean model with excellent computational efficiency. This has been demonstrated to be the case when modelling internal solitary wave breaking at a slope — an adaptive mesh simulation which captured the dynamics and energetics of the wave breaking process has been successfully performed on a single computer processor; I estimate that the equivalent simulation using the more traditional approach of a fixed mesh of uniform resolution (as would be required if the location of breaking was not known a priori) would require a mesh of approximately 27,000,000 nodes, which is certainly not feasible to be run on a single processor and would take excessive computational time.

Future work

Tidal flow of a stratified fluid over topography is the main mechanism by which internal waves are generated in the ocean. An attempt has been made to capture the internal lee wave generated by flow over a bump, and although the theoretical wavelength was captured by the numerical model, further work is needed to accurately model the amplitude of the lee wave. It is expected that this could be achieved through the use of higher resolution simulations run on a larger parallel computer.

The unstructured mesh multi-scale nature of the modelling approach considered here is well placed to conform to complex topography, and so having modelled the interaction of internal waves with an idealised slope, it would be valuable to investigate the interaction of internal waves with a realistic bathymetry, such as in Monterey Bay or the South China Sea for example.

The tilting tank test case considered in chapter 7 showed that Fluidity–ICOM can

accurately simulate the degeneration of interfacial waves into solitary waves, but a small offset was required in the evolution of the depth of the interface near to the centre of the tank with time. Incorporating a time dependent gravity vector direction to represent the transition of the tank from its initial position to a horizontal position, as occurs in the laboratory, may help to address this problem.

A quadratic drag term was used in the tilting tank test case to simulate the effects of sidewall friction in the laboratory model of interfacial waves. This could also be incorporated in the simulations of internal solitary wave breaking at a slope, and the effect of this on the energy reflected at the slope quantified.

All the results presented in this thesis were two–dimensional. Some three–dimensional simulations have been carried out, *e.g.* internal solitary wave breaking at a slope, but as the wave breaks the extra resolution required to resolve the three–dimensional dynamics has been prohibitively large. Three–dimensional adaptive mesh results could be performed in parallel, and the effect of including the extra dimension in the model on the energy budget examined.

Bibliography

A. Adcroft, C. Hill, and J. Marshall. Representation of topography by shaved cells in a height coordinate ocean model. *Mon. Wea. Rev.*, 125:2293–2315, 1997.

P. Aghsaee, L. Boegman, and Kevin G. Lamb. Breaking of shoaling internal solitary waves. *Journal of Fluid Mechanics*, 659:289–317, 2010.

M. H Alford. Internal swell generation: The spatial distribution of energy flux from the wind to mixed layer near-inertial motions. *Journal of Physical Oceanography*, 31(8), 2001.

P. G. Baines. The reflexion of internal/inertial waves from bumpy surfaces. *Journal of Fluid Mechanics*, 46:273–291, 1971a.

P. G. Baines. The reflexion of internal/inertial waves from bumpy surfaces. part 2: Split reflexion and diffraction. *Journal of Fluid Mechanics*, 49:113–131, 1971b.

M. F. Barad, P. Colella, and S. G. Schladow. An adaptive cut-cell method for environmental fluid mechanics. *International Journal for Numerical Methods in Fluids*, 60:473–514, 2009.

F. Bassi and S. Rebay. A high-order accurate discontinuous finite element method for the numerical solution of the compressible Navier-Stokes equations. *Journal Of Computational Physics*, 131(2):267–279, 1997.

G.K. Batchelor. *An Introduction to Fluid Dynamics*. Cambridge University Press, 1967.

S. Benhamadouche and D. Laurence. LES, Coarse LES, and Transient RANS comparison on the flow across a tube bundle. *Int. J. Heat Fluid Flow*, 24:470–479, 2003.

M. Berger and J. Oliger. Adaptive mesh refinement for hyperbolic partial differential equations. *J. Comp. Phys.*, 53:484–512, 1984.

J. Berntsen, J. Xing, and G. Alendal. Assessment of non-hydrostatic ocean models using laboratory scale problems. *Continental Shelf Research*, 26:1433–1447, 2006.

L. Boegman, G. N. Ivey, and J. Imberger. The degeneration of internal waves in lakes with sloping topography. *Limnology and Oceanography*, 50(5):1620–1637, September 2005.

D. Bourgault and D. E. Kelley. On the reflectance of uniform slopes for normally incident interfacial solitary waves. *Journal of Physical Oceanography*, 37:1156–1162, May 2007.

D. Bourgault, M. D. Blokhina, R. Mirshak, and D. E. Kelley. Evolution of a shoaling internal solitary wavetrain. *Geophysical Research Letters*, 34, 2007.

J. Boussinesq. *Théorie analytique de la chaleur*, volume 2. Paris: Gathier-Villars, 1903.

D. Cacchione and C. Wunsch. Experimental study of internal waves over a slope. *Journal of Fluid Mechanics*, 66:223–239, 1974.

S. Cai, S. Wang, and X. Long. A simple estimation of the force exerted by internal solitons on cylindrical piles. *Ocean Engineering*, 33(7):974 – 980, 2006.

V. Casulli and G.S. Stelling. Semi-implicit subgrid modelling of three-dimensional free-surface flows. *International Journal for Numerical Methods in Fluids*, 67(4):441–449, 2011. ISSN 1097-0363. doi: 10.1002/fld.2361. URL `http://dx.doi.org/10.1002/fld.2361`.

E. P. Chassignet, L. T. Smith, G. R. Halliwell, and R. Bleck. North Atlantic simulations with the hybrid coordinate ocean model (HYCOM): impact of the vertical coordinate choice, reference pressure, and thermobaricity. *J. Phys. Oceanogr.*, 33:2504–2526, 2003.

C. Chen, H. Liu, and R. C. Beardsley. An unstructured grid, finite-volume, three-dimensional, primitive equations ocean model: Application to coastal ocean and estuaries. *J. Atmos. Oceanic Tech.*, 20:159–186, 2003.

H. Cui, J.D. Pietrzak, and G.S. Stelling. A finite volume analogue of the p 1 nc - p 1 finite element: With accurate flooding and drying. *Ocean Modelling*, 35(1), 2010. doi: 10.1016/j.ocemod.2010.06.001.

B. Cushman-Roisin. *Introduction to Geophysical Fluid Dynamics*. Prentice Hall, 1994.

S. Danilov. Two finite-volume unstructured mesh models for large-scale ocean modeling. *Ocean Modelling*, 47(0):14 – 25, 2012. ISSN 1463-5003. doi: http://dx.doi.org/10.1016/j.ocemod.2012.01.004. URL `http://www.sciencedirect.com/science/article/pii/S1463500312000194`.

S. Danilov, G. Kivman, and J. Schröter. A finite element ocean model: principles and evaluation. *Ocean Modell.*, 6:125–150, 2004.

S. Danilov, Q. Wang, M. Losch, D. Sidorenko, and J. Schröter. Modeling ocean circulation on unstructured meshes: comparison of two horizontal discretizations. *Ocean Dynamics*, 58(5-6):365–374, 2008. ISSN 1616-7341. doi: 10.1007/s10236-008-0138-5. URL `http://dx.doi.org/10.1007/s10236-008-0138-5`.

T. Dauxois and W. R. Young. Near–critical reflection of internal waves. *Journal of Fluid Mechanics*, 390:271–295, 1999.

A. M. Davies. Application of the Galerkin method to the formulation of a three-dimensional nonlinear hydrodynamic numerical sea model. *Appl. Math. Model.*, 4:245–256, 1980.

S. F. Dotsenko. Generation of long internal waves in the ocean by a moving pressure zone. *Physical Oceanography*, 2(3):163–170, 1991.

E. Dumas, C. Le Provost, and A. Poncet. Feasability of finite element methods for oceanic general circulation modelling. In *Proc. Fourth Int. Conf. on Finite Elements in Water Resources*, pages 5,43–5,55. Hanover, Germany, 1982.

V. W. Ekman. On dead water. In F. Nansen, editor, *Norwegian North Polar Expedition, 1893–1896, Scientific Results*, volume 5. Longmans, London, 1904.

G. J. Fix. Finite element models for ocean circulation problems. *SIAM J. Appl. Math.*, 29:371–387, 1975.

L. A. Freitag and C. Ollivier-Gooch. Tetrahedral mesh improvement using swapping and smoothing. *Internat. J. Numer. Methods Eng.*, 40:3979–4002, 1997.

O. B. Fringer and R. L. Street. The dynamics of breaking progressive interfacial waves. *Journal of Fluid Mechanics*, 494:319–353, 2003.

O. B. Fringer, M. Gerritsen, and R. L. Street. An unstructured-grid, finite-volume, non-hydrostatic, parallel coastal-ocean simulator. *Ocean Modell.*, 14:139–278, 2006.

C. Garrett and E. Kunze. Internal tide generation in the deep ocean. *Annual Review of Fluid Mechanics*, 39:57–87, 2007.

C. Garrett and W. Munk. Internal waves in the ocean. *Annual Review of Fluid Mechanics*, 11:339–369, 1979.

P. L. George. *Delaunay Triangulation and Meshing: Application to Finite Elements*. Editions HERMES, Paris, 1998.

D. Gilbert and C. Garrett. Implications for ocean mixing of internal wave scattering off irregular topography. *Journal of Physical Oceanography*, 19:1716–1729, 1989.

A. E. Gill. *Atmosphere–Ocean Dynamics*. Academic Press, 1982.

L. Gostiaux and T. Dauxois. Laboratory experiments on the generation of internal tidal beams over steep slopes. *Physics of Fluids*, 19, 2007.

P. M. Gresho and R. L. Sani. *Incompressible Flow and the Finite Element Method*. John Wiley and Sons, 1998.

S. M. Griffies, C. Böning, F. O. Bryan, E. P. Chassignet, R. Gerdes, H. Hasumi, A. Hirst, A. M. Treguier, and D. Webb. Developments in ocean climate modelling. *Ocean Modell.*, 2:123–192, 2000.

D. B. Haidvogel, A. R. Robinson, and E. E. Schulman. The accuracy, efficiency, and stability of three numerical models with application to open ocean problems. *J. Comp. Phys.*, 34:1–53, 1980.

D. B. Haidvogel, J. L. Wilkin, and R. Young. A semi-spectral primitive equation ocean circulation model using vertical sigma coordinates and orthogonal curvilinear horizontal coordinates. *J. Phys. Oceanogr.*, 94:151–185, 1991.

K. R. Helfrich. Internal solitary wave breaking and run-up on a uniform slope. *Journal of Fluid Mechanics*, 243:133–154, 1992.

D. A. Horn, J. Imberger, and G. N. Ivey. The degeneration of large–scale interfacial gravity waves in lakes. *Journal of Fluid Mechanics*, 434:181–207, 2001.

A. Javam, J. Imberger, and S. W. Armfield. Numerical study of internal wave reflection from sloping boundaries. *Journal of Fluid Mechanics*, 396:183, 1999.

T. W. Kao, F.S. Pan, and D. Renouard. Internal solitons on the pycnocline: generation, propagation and breaking over a slope. *Journal of Fluid Mechanics*, 159:19–53, 1985.

S.C. Kramer and G.S. Stelling. A conservative unstructured scheme for rapidly varied flows. *International Journal for Numerical Methods in Fluids*, 58(2):183–212, 2008. ISSN 1097-0363. doi: 10.1002/fld.1722. URL `http://dx.doi.org/10.1002/fld.1722`.

C. Kranenburg and J. D. Pietrzak. Internal lee waves in turbulent two layer flow. *Journal of Hydraulic Engineering*, 115:1352–1370, 1989.

W. Krauss. *Methoden und Ergebnisse der theoretischen Ozeanographie*, volume 2 Internal Waves. Berlin: Gebrudüder Borntraeger, 1966.

P. K. Kundu. *Fluid Mechanics*. Academic Press, 1990.

R.J. Labeur and J.D Pietrzak. A fully three dimensional unstructured grid non-hydrostatic finite element coastal model. *Ocean Modelling*, 10, 2004.

K. G. Lamb. Nonlinear interaction among internal wave beams generated by tidal flow over supercritical topography. *Geophysical Research Letters*, 31, 2004.

K. G. Lamb and V. T. Nguyen. Calculating energy flux in internal solitary waves with an application to reflectance. *Journal of Physical Oceanography*, 39:559–580, March 2009.

M. Laugier, P. Agnot, and L. Mortier. Nested grid methods for an ocean model: a comparative study. *Int. J. Numer. Methods Fluids*, 23:1163–1195, 1996.

C. Le Provost and P. Vincent. Some tests of precision for a finite element model of ocean tides. *J. Comp. Phys.*, 110:273–291, 1986.

C. Le Provost, M. L. Genco, F. Lyard, P. Vincent, and P. Canceil. Spectroscopy of the world ocean tides from a finite element hydrodynamic model. *J. Geophys. Res.*, 99(C12): 24777–24797, 1994.

S. Legg and A. Adcroft. Internal wave breaking at concave and convex continental slopes. *Journal of Physical Oceanography*, 33:2224–2246, 2003.

K. Lim, G. N. Ivey, and R. I. Nokes. The generation of internal waves by tidal flow over continental shelf/slope topography. *Environmental Fluid Mechanics*, 8:511–526, 2008.

E. N. Lorenz. Available potential energy and the maintenance of the general circulation. *Tellus*, 7:157–167, 1955.

L. N. Ly and P. Luong. Numerical multi-block grids in ocean circulation modeling. *Applied Mathematical Modelling*, 23:865–879, 1999.

F. Lyard, F. Lefevre, T. Letellier, and O. Francis. Modelling the global ocean tides: modern insights from FES2004. *Ocean Dynamics*, 56:394–415, 2006.

D. R. Lynch and W. R. Gray. A wave equation model for finite element tidal computations. *Comput. Fluids*, 7:207–228, 1979.

D. R. Lynch, J. T. C. Ip, C. E. Naimie, and F. E. Werner. Comprehensive coastal circulation model with application to the Gulf of Maine. *Contin. Shelf Res.*, 16:875–906, 1996.

L. Maas. Worden mooi-weer verdrinkingen door dood-water veroorzaakt? URL `http://www.nioz.nl/files/upload/users/537050/maasvanharen06AA.pdf`.

J. Marshall and F. Schott. Open-ocean convection: observations, theory and models. *Review of Geophysics*, 37(1):1–64, 1999.

T. Matsuura and T. Hibiya. An experimental and numerical study of the internal wave generation by tide-topography interaction. *Journal of Physical Oceanography*, 20:506–521, 1990.

T. Maxworthy. A note on the internal solitary waves produced by tidal flow over a three-dimensional ridge. *Journal of Geophysical Research*, 84(C1):338–346, 1979.

G. L. Mellor, L.Y. Oey, and T. Ezer. Sigma coordinate pressure gradient errors and the seamount problem. *J. Atmos. Oceanic Tech.*, 15:1122–1131, 1998.

H. Michallet and G. N. Ivey. Experiments on mixing due to internal solitary waves breaking on uniform slopes. *Journal of Geophysical Research*, 104(C6):13467–13477, June 1999.

C. Moulinec, S. Benhamadouche, D. Laurence, and M. Peric. LES in a u-bend pipe meshed by polyhedral cells. pages 48–60. Elsevier, 2005.

D. E. Mowbray and B. S. H. Rarity. A theoretical and experimental investigation of the phase configuration of internal waves of small amplitude in a density stratified fluid. *Journal of Fluid Mechanics*, 28:1–16, 1967.

W. Munk and C. Wunsch. Abyssal recipes ıı: energetics of tidal and wind mixing. *Deep Sea Research Part I: Oceanographic Research Papers*, 45(12):1977 – 2010, 1998.

J. Nycander. Generation of internal waves in the deep ocean by tides. *Journal of Geophysical Research*, 110, 2005.

C. C. Pain, A. P. Umpleby, C. R. E. de Oliveira, and A. J. H. Goddard. Tetrahedral mesh optimisation and adaptivity for steady-state and transient finite element calculations. *Comput. Methods Appl. Mech. Engrg.*, 190:3771–3796, 2001.

B. Parker. Waves beneath the sea. *Mariners Weather Log*, 42(2):11–17, August 1999.

W. R. Peltier and C. P. Caulfield. Mixing efficiency in stratified shear flows. *Annual Review of Fluid Mechanics*, 35:135–167, 2003.

J. Peraire and K. Morgan. Unstructured mesh generation including directional refinement for aerodynamic flow simulation. *Finite Elements in Analysis and Design*, 25:343–356, 1997.

O. M. Phillips. *The Dynamics of the Upper Ocean.* Cambridge University Press, 2nd edition, 1977.

J. Pietrzak and R. J. Labeur. Trapped internal waves over undular topography in a partially mixed estuary. *Ocean Dynamics*, 54(3-4):315–323, 2004. ISSN 1616-7341. doi: 10.1007/s10236-003-0081-4. URL `http://dx.doi.org/10.1007/s10236-003-0081-4`.

P. R. Pinet. *Invitation to Oceanography*. Jones and Bartlett Publishers, 5th edition, 2008. URL `www.jbpub.com/oceanlink`.

Pliny. *Historia Naturalis*. 77.

S. Popinet and G. Rickard. A tree-based solver for adaptive ocean modelling. *Ocean Modelling*, 16(3–4):224–249, 2007. ISSN 1463-5003. URL `http://www.sciencedirect.com/science/article/pii/S1463500306000989`.

Lord Rayleigh. Investigation of the character of the equilibrium of an incompressible heavy fluid of variable density. *Proc. London Math. Soc.*, 14:170–177, 1883.

G. Rickard, J. O'Callaghan, and S. Popinet. Numerical simulations of internal solitary waves interacting with uniform slopes using an adaptive model. *Ocean Modelling*, 30: 16–28, 2009.

J. Roberts. *Internal Gravity Waves in the Ocean*, volume 2 of *Marine Science*. Marcel Dekker, Inc., 1975.

J. W. Sandström. Dynamische versuche mit meerwasser. *Annal. Hydrogr. Marit. Meteorol.*, 36:6–23, 1908.

H. Segur and J.L. Hammack. Soliton models of long internal waves. *Journal of Fluid Mechanics*, 118:285–304, 1982.

P.T. Shaw, D. S. Ko, and S.Y. Chao. Internal solitary waves induced by flow over a ridge: with applcations to the northern South China Sea. *Journal of Geophysical Research*, 114, 2009.

R. E. Shea and W. W. Broenkow. The role of internal tides in the nutrient enrichment of monterey bay, california. *Estuarine, Coastal and Shelf Science*, 15:57–66, 1982.

I. M. Smith and D. V. Griffiths. *Programming the Finite Element Method*. John Wiley & Sons, third edition, 1998.

G. G. Stokes. On the theory of oscillatory waves. *Trans. Cambridge Phil. Soc.*, 8:441, 1847.

P. K. Sweby. High-resolution schemes using flux limiters for hyperbolic conservation-laws. *Siam Journal on Numerical Analysis*, 21(5):995–1011, 1984.

O. Thiem and J. Berntsen. Numerical studies of large-amplitude internal waves shoaling and breaking at shelf slopes. *Ocean Dynamics*, 2009.

S. A. Thorpe. The excitation, dissipation, and interaction of internal waves in the deep ocean. *Journal of Geophysical Research*, 80(3):328–338, 1975.

S. A. Thorpe and A. P. Haines. A note on observations of wave reflection on a 20 ° slope. *Journal of Fluid Mechanics*, 178:299–302, 1987.

Y. H. Tseng and J. H. Ferziger. Mixing and available potential energy in stratified flows. *Physics of Fluids*, 13:1281–1293, May 2001.

C.M. Van der Boon. Numerical modelling of internal waves in the browse basin., 2011.

S. K. Venayagamoorthy and O. B. Fringer. Nonhydrostatic and nonlinear contributions to the energy flux budget. *Geophysical Research Letters*, 32, 2005.

S.K. Venayagamoorthy and O.B. Fringer. Numerical simulations of the interaction of internal waves with a shelf break. *Physics of Fluids*, 18, July 2006.

S.K. Venayagamoorthy and O.B. Fringer. On the formation and propagation of nonlinear internal boluses across a shelf break. *Journal of Fluid Mechanics*, 577:137–159, 2007.

V. Vlasenko and K. Hutter. Numerical experiments on the breaking of solitary internal waves over a slope–shelf topography. *Journal of Physical Oceanography*, 32:1779–1793, June 2002.

V. Vlasenko and N. Stashchuk. Three-dimensional shoaling of large-amplitude internal waves. *Journal of Geophysical Research*, 112, 2007.

Q. Wang, S. Danilov, and J. Schröter. Finite element ocean circulation model based on triangular prismatic elements, with application in studying the effect of topography representation. *Journal of Geophysical Research: Oceans*, 113(C5):n/a–n/a, 2008. ISSN 2156-2202. doi: 10.1029/2007JC004482. URL `http://dx.doi.org/10.1029/2007JC004482`.

N. P. Weatherill, O. Hassan, K. Morgan, J. W. Jones, B. G. Larwood, and K. Sorenson. Aerospace simulations on parallel computers using unstructured grids. *Int. J. Numer. Methods Fluids*, 40:171–187, 2002.

L. White, E. Dellersnijder, and V. Legat. A three-dimensional unstructured mesh nite element shallow-water model, with application to the ows around an island and in a wind-driven, elongated basin. *Ocean Modelling*, 22:26–47, 2008.

G. B. Whitham. *Linear and Nonlinear Waves*. Wiley, 1974.

C. R. Wilson. *Modelling multiple-material flows on adaptive unstructured meshes*. PhD thesis, Imperial College London, London, UK, 2009.

K. B. Winters, P. N. Lombard, J. R. Riley, and E. A. D'Asaro. Available potential energy and mixing in density-stratified fluids. *Journal of Fluid Mechanics*, 289:115–128, 1995.

C. Wunsch and R. Ferrari. Vertical mixing, energy, and the general circulation of the oceans. *Annual Review of Fluid Mechanics*, 36(1):281–314, 2004.

O. C. Zienkiewicz, R. L. Taylor, J. Z. Zhu, and P. Nithiarasu. *The Finite Element Method: Its basis and fundamentals; for solid and structural mechanics; for fluid mechnics*. Elsevier Butterworth-Heinemann, sixth edition, 2005.